Angle-Resolved Photoemission Spectroscopy Study of High Temperature Superconductor Cuprate, and Potential High Temperature Superconductors K-Doped *p*-Terphenyl and Trilayer Nickelate

by

Haoxiang Li

B.S., Lanzhou University, China, 2011

M.S., University of Colorado Boulder, 2014

A thesis submitted to the

Faculty of the Graduate School of the

University of Colorado in partial fulfillment

of the requirements for the degree of

Doctor of Philosophy

Department of Physics

2017

This thesis entitled:
Angle-Resolved Photoemission Spectroscopy Study of High Temperature Superconductor Cuprate, and Potential High Temperature Superconductors K-Doped p-Terphenyl and Trilayer Nickelate
written by Haoxiang Li
has been approved for the Department of Physics

Prof. Daniel S. Dessau

Prof. Dmitry Reznik

Date

The final copy of this thesis has been examined by the signatories, and we find that both the content and the form meet acceptable presentation standards of scholarly work in the above mentioned discipline.

Li, Haoxiang (Ph.D., Physics)

Angle-Resolved Photoemission Spectroscopy Study of High Temperature Superconductor Cuprate, and Potential High Temperature Superconductors K-Doped p-Terphenyl and Trilayer Nickelate

Thesis directed by Prof. Daniel S. Dessau

The macroscopic quantum phenomenology of superconductivity has attracted broad interest from both scientific research and applications. Many exotic physics found in the first high T_C superconductor family cuprate remain unsolved even after 30 years of intense study. Angle-Resolved Photoemission Spectroscopy (ARPES) provides the direct probe to the major information of the electronic interactions, which plays the key role in these exotic physics including high T_C superconductivity. ARPES is also the best tool to study the electronic structure in materials that potentially hold high T_C superconductivity, providing insight for materials research and design.

In this thesis, we present the ARPES study of the cuprate high T_C superconductor Pb doped $Bi_2Sr_2CaCu_2O_{8+\delta}$, and potential high T_C superconductors K doped p-terphenyl, and trilayer nickelate $La_4Ni_3O_{10}$. For Pb doped Bi2212, our study focuses on the key part of the electronic interactions—the self-energies. With the development of a novel 2-dimensional analysis technique, we present the first quantitative extraction of the fully causal complex self-energies. The extracted information reveals a conversion of the diffusive strange-metal correlations into a coherent highly renormalized state at low temperature followed by the enhancement of the number of states for pairing. We then further show how this can lead to a strong positive feedback effect that can stabilize and strengthen superconducting pairing. In K doped p-terphenyl, we discover low energy spectral gaps that persist up to 120 K, consistent with potential Meissner effect signal from previous studies. Among a few potential origins for these gaps, we argue that the electron pairing scenario is most likely. For $La_4Ni_3O_{10}$, we present the Fermiology and electron dynamics of this material, and they show certain similarities to the cuprate electronic structure, as well as a few unique features.

Dedication

To my lovely wife, my child and my parents

Acknowledgements

First, I would like to thank my parents for their constant love, and their supports for every important choice that I made.

I would like to thank my advisor Daniel S. Dessau. He is an excellent mentor, teacher, and co-worker. He encouraged me to explore every hidden physics in data, and provided amazing visions and guidance.

I would like to thank all my collaborators. Qiang Wang, Yue Cao, Ted Reber, Justin Griffith and Steve Parham have been generously sharing their insight of physics and their knowledge in ARPES, optics, ultra-high vacuum etc. Gerald Arnold has provided important theoretical advice for our projects. I also want to thank Justin Waugh, Tom Nummy, Xiaoqing Zhou for their supports in the experiments that I conducted at CU and other synchrotron facilities. In particular, I want to thank Xiaoqing Zhou, who has been my research partner for the majority of my PhD time. We went to numerous beam runs, and worked together on many fruitful projects. I really enjoyed this partnership and learned a lot from it.

I would like to thank the staffs at synchrotron facilities providing technical supports for our experiments: Makoto Hashimoto, Donghui Lu, Yi-De Chuang, Jonnathan Denlinger, Sung-kwan Mo, Eli Rotenberg, Aaron Bostwick, Alexei Fedorov and all the scientists and post-docs at the beamlines.

Finally, I want to thank my lovely wife, Manjun Deng, without her love and supports, I couldn't finish my PhD.

Contents

Chapter

Figures

Figure

Chapter 1

Introduction

In this thesis, we will present the Angle-Resolved Photoemission Spectroscopy (ARPES) study of the high temperature superconductor cuprate, potential high temperature superconductor K-doped *p*-terphenyl and trilayer nickelate. The first two chapters of the thesis will provide a necessary background for ARPES and superconductivity. Next, we will introduce a novel two dimensional analysis technique that we developed for ARPES spectra, and use it to extract the key information about the electronic interactions in high temperature superconductor cuprates. In chapter five, we will report the spectroscopic evidence of a gap that persist to 120K in a potential organic superconductor—surface K-doped *p*-terphenyl. Finally, we will present the electronic structure and dynamics of the trilayer nickelate $La_4Ni_3O_{10}$, and compare them to the ones from cuprates.

Chapter 2

Introduction to Angle-Resolved Photoemission Spectroscopy

Among the conventional experimental techniques for the study of condensed-matter systems such as neutron scattering, transport measurements, scanning tunneling microscopy, and optical conductivity measurements, angle-resolved photoemission spectroscopy (ARPES) is the most effective tool for studying electron band structures and electron dynamics. As ARPES directly probes the single particle spectral function, a plethora of useful properties can be extracted from an ARPES spectrum including band dispersions, spectral gaps, the complex self-energies etc. In this chapter, I will first introduce the general mechanisms of photoemission, then discuss the basic concepts of ARPES experiments as well as how to interpret the ARPES spectrum.

2.1 Introduction to Photoemission

The basic operating principle of ARPES is derived from the photo-electric effect, which was first observed by Heinrich Hertz in 1887. Subsequent researchers, building on the work of Hertz, found that when materials absorb electromagnetic radiation with a very short wavelength (ultraviolet, X-ray) the material will eject electrons. Later in 1905, a theoretical explanation was proposed by Albert Einstein, wherein the photo-electric effect was described as the absorption of a quantum of light leading to the ejection of an electron. These quanta are now known as photons. When the material absorbs a photon of energy that is larger than its work function, a photoelectron is emitted. This theory, among others, directly led to the development of quantum mechanics which

revolutionized modern physics. The photoelectric effect is described by the equation below,

$$E_f - E_i = h\nu - \Phi \tag{2.1}$$

where E_i is the initial energy of the electron, E_f is the final kinetic energy of the emitted photoelectrons, $h\nu$ is the incident photon energy, and Φ is the work function, which is the minimum energy needed to promote an electron from the surface into the vacuum. Photoemission spectroscopy (or PES) measures the kinetic energy E_f of the emitted photoelectrons. With this information, one can measure the occupied electron density of states (DOS) in the material (see Fig. 2.1). The work functions in most materials are in the region of 4 to 6 eV. Thus the photoemission experiments are typically performed at synchrotron facilities using ultra-violet, or X-ray photons.

2.2 Angle-Resolved Photoemission

The photoemission equation (eqn. 2.1) describes the energy conservation of the photoelectric process, which allows for the reconstruction of the initial kinetic energy of electrons in the material. The same conservation law approach can be applied to initial and final state momenta. Fig. 2.2 shows a typical experimental setup of ARPES. The emission angles of photoelectrons are resolved via an electron lens, and the kinetic energy is resolved by the electron analyser. In order to then apply momentum conservation laws we first recognize that the momentum of the photon is substantially smaller than the typical momenta of electrons in these experiments (10eV photon correspond to $5m\mathring{A}^{-1}$, where the typical Brillouin zone size is on the scale of $1\mathring{A}^{-1}$). Using this approximation where the photon momentum is taken to be zero, the in plane $k_{i\|}$ and out of plane $k_{i\perp}$ momentum of the initial state can be described by equations

$$k_{i\|} = \sqrt{\frac{2m}{\hbar^2}E_f}\sin\theta \tag{2.2}$$

$$k_{i\perp} = \sqrt{\frac{2m}{\hbar^2}(E_f\cos^2\theta - V_0)}. \tag{2.3}$$

where V_0 is the inner potential. When electrons leave the surface, the in-plane momentum is conserved, thus, $k_{i\|} = k_{f\|}$ is simply determined by the final kinetic energy and the emission angle of

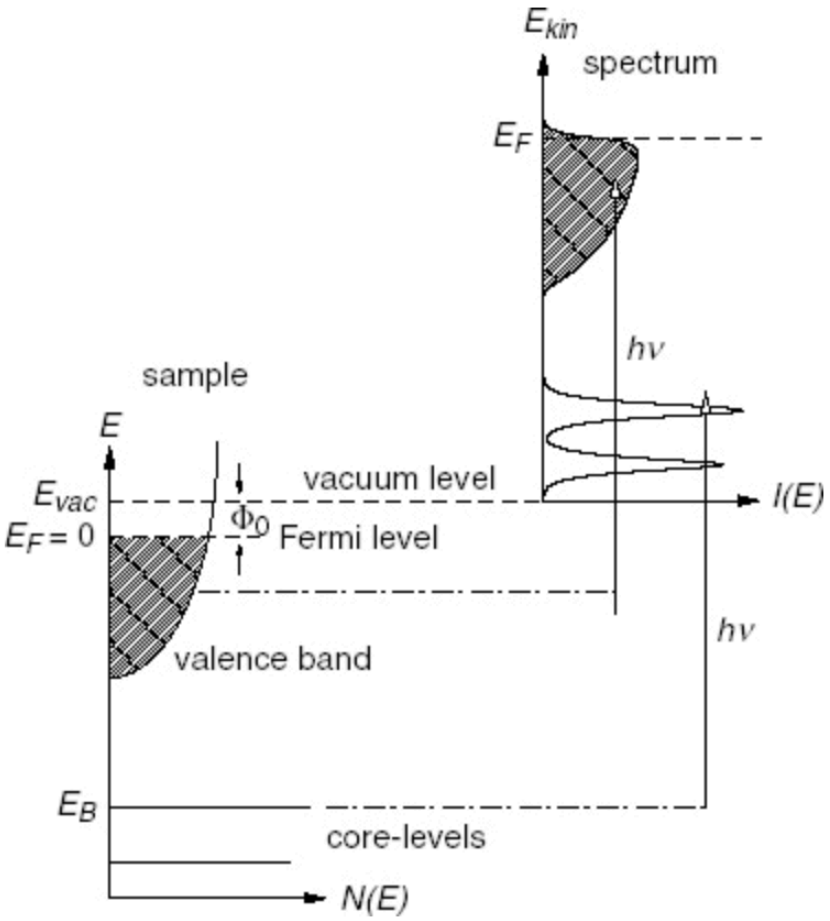

Figure 2.1: Schematic of the photoemission process. Electrons with binding energy E_B are excited above the vacuum level E_{vac} by photons with energy $h\nu$. The photoelectron distribution is a first order image of the occupied electron density of states in the material. Figure from [1]

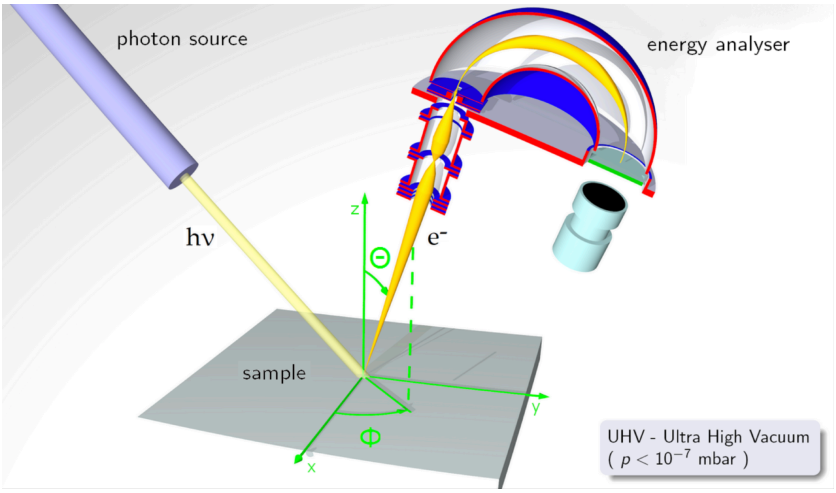

Figure 2.2: Schematic of the ARPES experimental setup. Figure from wiki pedia, *http* : *//en.wikipedia.org/wiki/Photoemission*$_s$*pectroscopy*

the photoelectron. However, the out-of-plane momentum is not conserved due to the discontinuity of the surface/vacuum potential. A photon energy scan is typically required to experimentally observe the periodicity of the dispersion in the out-of-plane direction, enabling the acquisition of the inner potential of the solid, and ultimately determining the out-of-plane momentum $k_{i\perp}$.

2.3 Photoemission process

The most intuitive way to explain the process is the three step model proposed by Spicer [2]. In this model, the photoemission process is separated into three parts: (1) optical excitation of the electron in the material, (2) transport of the excited electron to the surface, and (3) escape of the excited electron into the vacuum (see Fig. 2.3). The first step among the three provides the most important information, namely, the intrinsic physics of the electronic structure in the sample. The probability of the photo-excitation follows Fermi's golden rule:

$$\omega_{fi} = \frac{2\pi}{\hbar} |\left\langle \Psi_f^N \right| H^{int} \left| \Psi_i^N \right\rangle|^2 \delta(E_f^N - E_i^N - h\nu) \tag{2.4}$$

where $\left|\Psi_i^N\right\rangle$ and $\left\langle\Psi_f^N\right|$ are the initial and final state of the N particle system, and H^{int} is the electron photon interaction Hamiltonian $H^{int} = -\frac{e}{mc}\boldsymbol{A}\cdot\boldsymbol{p}$, with $\boldsymbol{A}$ denoting the electromagnetic vector potential, and $\boldsymbol{p}$ denoting the electron momentum.

Considering the "Sudden Approximation" that is commonly used in the photoemission process of a many-body system, the excited photoelectron is assumed to have no interaction with the rest of the electrons in the Fermi sea. Thus the final state in equation 2.4 is considered to be a product of the single electron wavefunction and the many body wavefunction with $N-1$ electrons, $\Psi_f^N = \mathcal{A}\phi_f^k\Psi_f^{N-1}$, with $\mathcal{A}$ denoting the antisymmetric operator, and ϕ_f^k is the photoelectron wavefunction. The first step is then reduced to the relaxation of the quasi-hole that is created by removing one electron from the system.

The second step is described by the probability of the excited electrons reaching the surface without scattering (either elastic or inelastic), which is related to the surface sensitivity of ARPES that determined by the photoelectron's mean free path. The scattering processes in this step

typically produces a continuous background in the ARPES spectra, and these background counts are usually subtracted or ignored. The third step is determined by the probability of transmission through the surface, which depends on the kinetic energy of the photoelectrons and the work function.

The one step model, on the other hand, takes a more quantum mechanical view of the whole photoemission process. A single coherent process considering the photo-excited electrons and their propagation into the vacuum is constructed with a more detailed consideration of different interference between electrons in all three steps. The one step model is generally more complicated and less intuitive as compared to the three step model.

2.4 Single-Particle Spectral Function

The intensity of the ARPES spectrum takes the general form of

$$I(k,\omega) = |\langle\phi_f|\boldsymbol{A}\cdot\boldsymbol{p}|\phi_i\rangle|^2 f(\omega)A(k,\omega)\otimes R(k,\omega). \tag{2.5}$$

The first part of this equation is the matrix element, where here we only show the leading term in the electron photon interaction—the diople term $\boldsymbol{A}\cdot\boldsymbol{p}$. The matrix element can suppress the intensity of the ARPES spectrum in certain areas of the k space and at certain energy. The second term is just the Fermi-Dirac distribution function. The last term $R(k,\omega)$ describes the broadening due to imperfections of experiment conditions, such as energy and momentum resolution, electromagnetic stray field, warpage of the sample surface etc. The most important part, which contains the intrinsic physics of the electron behavior are in $A(k,\omega)$, the single-particle spectral function. It directly connects to the single-particle Green's function as $A(k,\omega) = -\frac{1}{\pi}ImG(k,\omega)$, where $G(k,\omega)$ is the single particle Green's function and is also the propagator that describes the many-body system. In principal, the spectral function includes all information of the electron interactions in the system.

Before stepping into the interacting many-body system, let's first take a look at the non-

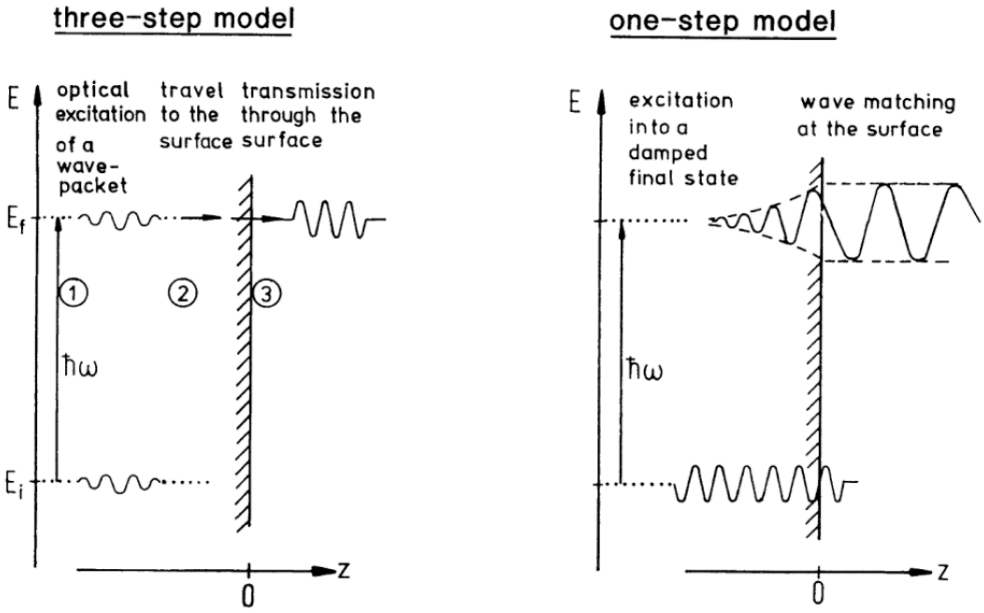

Figure 2.3: Illustration of the three step model and one step model. The three steps are (1) optical excitation of the electron in the material, (2)transport of the excited electron to the surface, and (3) escape of the excited electron into vacuum. The one step model describes the one-electron wave function that gets excited and propagates into the vacuum. Figure from [3]

interacting case, the bare Green's function, which is:

$$G(k,\omega) = \frac{1}{\omega - \epsilon_k + i\delta} \tag{2.6}$$

where ω is the electron energy, ϵ_k is the bare band energy at momentum k, δ is a infinitesimal term to make sure the integral of G converged. The spectral function corresponds to the bare Green's function is just a Dirac delta function that peaks at $\omega = \epsilon_k$, as shown in Fig. 2.4a

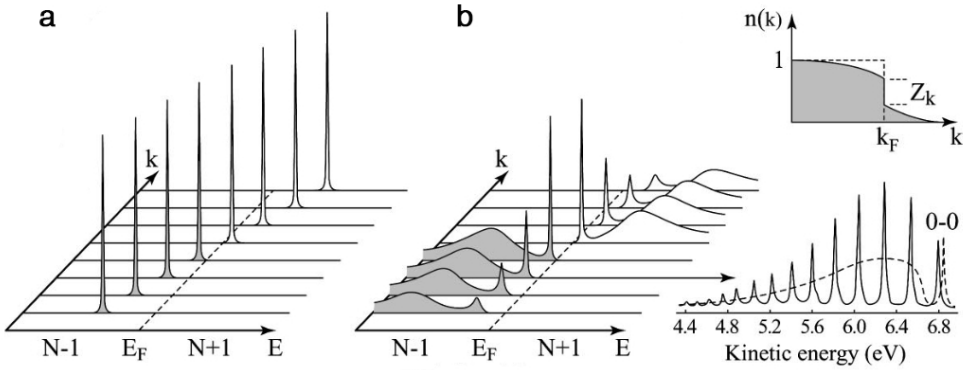

Figure 2.4: Panel a, momentum-resolved one-electron removal and addition spectral function for a noninteracting electron system with a single energy band dispersing across E_F. Panel b, the same spectra for an interacting Fermi-liquid system. For both noninteracting and interacting systems the corresponding ground state (T=0K) momentum distribution function n(k) is also shown. Lower right, photoelectron spectrum of gaseous hydrogen and the ARPES spectrum of solid hydrogen developed from the gaseous one. Figure adapted from [4]

Next, we include the quasiparticle self-energy term Σ that describes all the complexities of the electronic interactions, and the Green's function becomes:

$$G(k,\omega) = \frac{1}{\omega - \epsilon_k + \Sigma} \tag{2.7}$$

where the self-energy Σ is a complex function $\Sigma = \Sigma' + i\Sigma''$ that varies by energy, momentum and temperature etc. The physical meaning of the self-energy would be more clear as we look at the spectral function,

$$A(k,\omega) = -\frac{1}{\pi}\frac{\Sigma''}{(\omega - \Sigma' - \epsilon_k)^2 + \Sigma''^2}. \tag{2.8}$$

For simplification, we now consider that Σ' and Σ'' are constant with k and ω, then we can see that, for certain energy ω, $A(k,\omega)$ becomes a Lorentzian function, with the peak at $\omega = \epsilon + \Sigma'$, and the

full width half maximum (FWHM) as $2\Sigma''$. From this simplified case, we can learn that the Σ'' is the broadening term in the spectral function, which describes the quasiparticle life time. And Σ' is the extra energy that adds to the bare electron energy from the interactions. The effect of Σ' will deviate the quasiparticle dispersions from the bare dispersions, and typically enhance the effective mass of the quasiparticle. However, both Σ' and Σ'' are usually functions of the momentum and energy. An example of the spectral function with the self-energy described by the Fermi-liquid model [5] is shown in Fig. 2.4 panel b.

For many materials, the self-energies Σ are usually varying slowly with momentum. Thus, they can be considered as a constant in a small region of the k space at certain energy. In the analysis of ARPES spectra, if the electron band is close to a linear dispersion, and simplified as $\epsilon_k = v_b(k - k_F)$, the two dimensional spectral function can then be analyzed by a series of simple one dimensional cuts (Momentum Distribution Curves, or MDCs). The equation below shows how the quantitative informations of electron dispersions and self-energies can be extracted from the MDC method,

$$\begin{aligned} A(k,\omega) &= -\frac{1}{\pi}\frac{\Sigma''}{(\omega - v_b(k-k_F) - \Sigma')^2 + \Sigma''^2} \\ &= -\frac{1}{\pi v_b^2}\frac{\Sigma''}{(k - k_F - \frac{\omega-\Sigma'}{v_b})^2 + (\Sigma''/v_b)^2} \\ &= -\frac{1}{\pi v_b^2}\frac{\Sigma''}{(k-k_0)^2 + (\Sigma''/v_b)^2} \end{aligned}$$

where v_b is the bare band velocity, k_F is the Fermi momentum, $k_0 = k_F + \frac{\omega-\Sigma'}{v_b}$. The MDC at energy ω can then be considered as a lorenzian function peak at k_0 with the FWHM as $\frac{2\Sigma}{v_b}$. By fitting each MDC, and with an assumption of the bare electron velocity v_b, one can extract the electon dispersion from k_0 and ω together with the imaginary self-energy Σ''. This method has been used widely in the analysis of the ARPES spectrum. However, once the spectral feature deviates from a sharp and well linearly dispersive band due to a shallow band bottom, a spectral gap opening, or a strong mass enhancement etc., the one dimensional MDC method would fail to extract the quantitative information. Later in Chapter 4 we will discuss a more advanced 2-

dimensional analysis technique that will allow us to extract the comprehensive information from the spectrum.

Chapter 3

Introduction to Superconductivity and Cuprate High Temperature Superconductors

Since the discovery of zero resistance in elemental mercury at 4K by Heike Kammerlingh Onnes (see Fig. 3.1), superconductors have become one of the main research topics in the field of condensed matter physics. This macroscopic manifestation of quantum physics has now been found in a broad range of materials. In 1933, Walther Meissner and Robert Ochsenfeld observed that superconductors are perfectly diamagnetic: the so-called Meissner effect. Zero resistance and the Meisnner effect in tandem are considered to be the key signatures of superconductivity.

In 1987, a ceramic copper oxide (Cuprate) was discovered to host superconductivity. This discovery was quite surprising as all previous superconductors were good metals, whereas the non-superconducting phase (normal state) of cuprates was shown to be a bad metal by transport measurement. Later, many superconducting members from the cuprate family were discovered, many of which had significantly higher transition temperatures. These series of superconductors had transition temperatures greater than that of liquid nitrogen, up to $\sim$130K at ambient pressure. In 2008, the discovery of iron based superconductors extended the family of high temperature superconductors to ferromagnetic materials. Organic materials have also been proposed to be strong candidates to host high temperature superconductivity [7]. Aromatic organic materials have recently shown to potentiallly host superconductivity [8] up to 120K. The discovery of new high temperature superconductors in the past 30 years has triggered an intense search for possible room temperature superconductors, and for a new microscopic mechanism beyond the traditional BCS

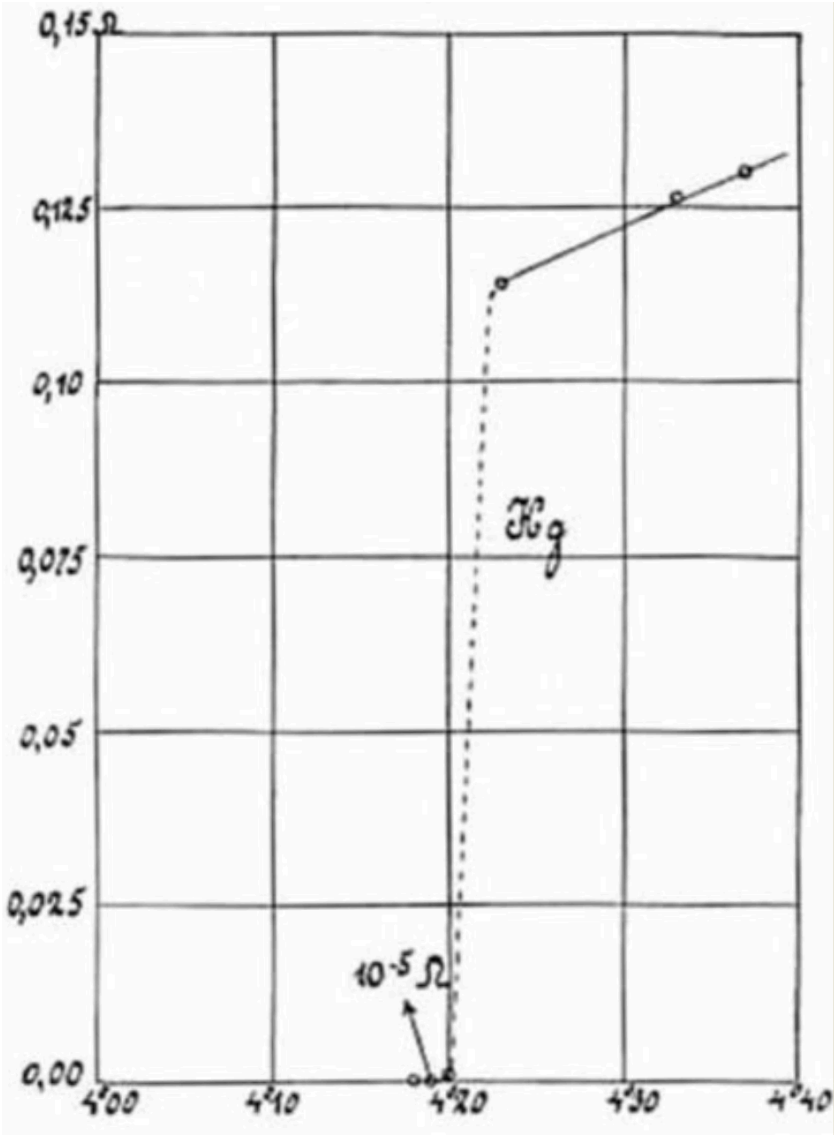

Figure 3.1: Resistance (ohms) vs temperature (kelvin) for mercury. This is the original plot from Onnes' paper in 1911 [6]

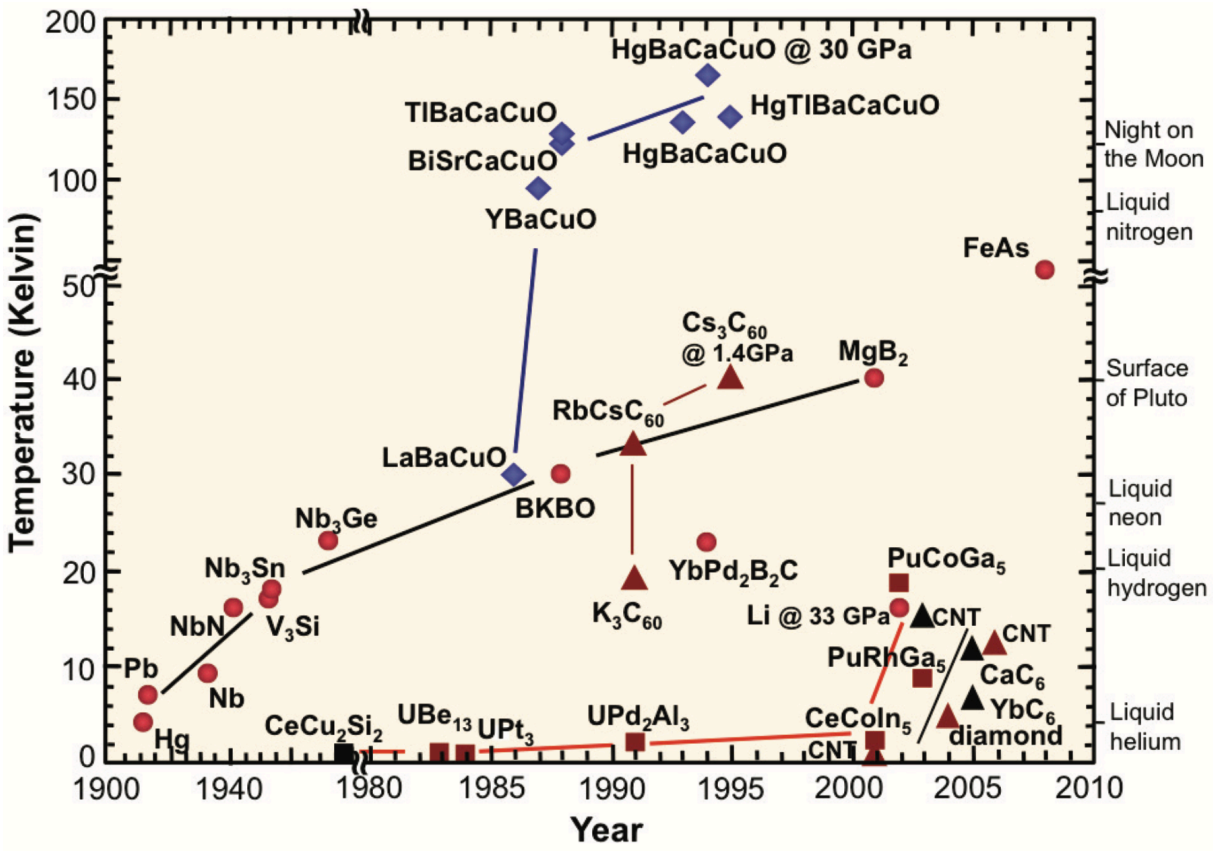

Figure 3.2: History of superconductivity. The transition temperature of superconductor vs the discovery year. Image courtesy of Department of Energy - Basic Energy Sciences

theory that would explain high temperature superconductivity.

In this chapter, I will briefly present a basic formulation of BCS theory followed by a brief introduction of high temperature cuprate superconductors and the superconducting Green's function (Nambu-Gorkov formalism) which will be further discussed in chapter 4.

3.1 BCS theory

Since the discovery by Onnes in 1911, a theoretical explanation for the phenomenon of superconductivity became one of the holy grails in physics research. However, not until 1957 was the first microscopic mechanism describing superconductivity proposed. This was the famous "BCS" Theory developed by Bardeen, Schrieffer, and Cooper [9].

The main idea of BCS theory is that a weak attraction between electrons can cause the instability in the Fermi-sea, especially for states near the Fermi level, leading to the formation of bound pairs of electrons. Such bound electron pairs then condense into a coherent ground state that is similar to the Bose-Einstein condensate, presenting macroscopic phase coherence and superfluid properties. However, the Coulomb interaction between electrons manifests as a repulsive force not an attractive one. In the conventional BCS theory, the attractive pairing "glue" between electrons is described to be as follows: an electron passing through the crystal lattice attracts positive ions in the lattice, causing a distortion of the lattice. Then, the region of lattice distortion now with excess positive charge attracts another electron. Thus the lattice mediates a weak, delayed attraction between the two electrons. Figure 3.3 shows a cartoon of the pairing via lattice distortions. The small lattice distortions are described as phonons (a quanta of atomic ion vibrations through the lattice). The electrons form pairs by exchanging virtual phonons. This phonon-mediated pairing has been proved to be correct in conventional superconductors [11] but not in high temperature cuprate superconductors. This distinction will be addressed in the later section.

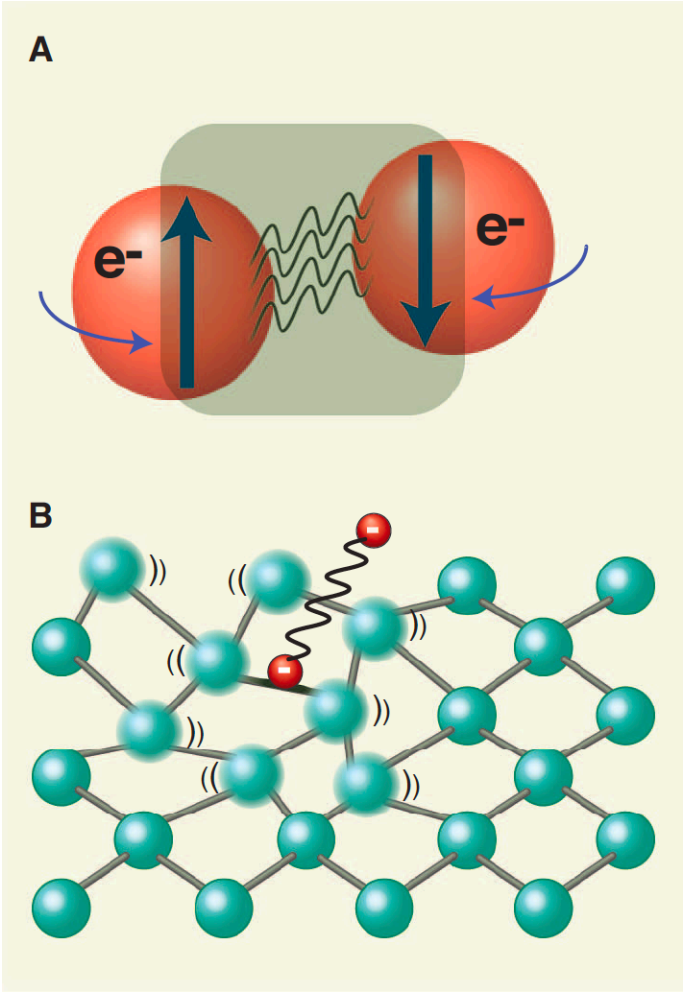

Figure 3.3: Phonon mediated pairing. Panel a, schematic of the electron pair. Panel b, cartoon of the phonon-mediated pairing. Figure from [10]

3.2 High Temperature Superconductivity

For phonon-mediated superconducting pairing, the limit of the transition temperature was theoretically predicted to be 40K [12]. Most of the superconductors that were discovered before 1986 obeyed this rule and had properties that were consistent with BCS theory. In 1986, Bednorz and Muller discovered a new superconductor, Lanthanum Barium Copper Oxide (LBCO), with a transition temperature of 35K. Soon after that, high transition temperature superconductors were found within the cuprate family, some with T_C as high as 135K at ambient pressure. Cuprate materials became the first family of high temperature superconductors. More importantly, the fact that these materials superconduct at temperatures accessible with liquid nitrogen (77K) provides enormous potential for applications. For the first time, superconducting devices could be produced and operated at low cost, without the need for expensive liquid helium for cooling. On the other hand, the cuprate superconductors also present many exotic properties that do not fit the existing theoretical framework. For instance, superconductivity arising from an antiferromagnetic parent compound with strong electronic correlations cannot be explained by traditional BCS theory, where the pairing glue is not likely produced by weak-coupling electron-phonon interactions, although the exact origin is still a mystery today (See Fig. 3.4 for the phase diagram of hole-doped cuprate). Furthermore, the strange metal normal state in cuprate superconductors also deviates from Landau's Fermi-liquid theory [5] [13], which ordinarily describes the many-body interactions in metallic materials well. Beyond these differences, there is also the issue of the pseudogap states [15], which have now become another great mystery in the field of strong correlated materials. Although these materials were discovered nearly 30 years ago, solutions to these puzzles have yet to be found.

Before continuing, some general information regarding cuprates is warranted. The Cu ion in cuprates has 9 valence electrons in the $3d$ orbital states. Superconductivity emerges by doping holes into the antiferromagnetic parent compounds (see phase diagram in Fig. 3.4). The highest transition temperature (optimal doping) typically emerges at around 16% hole doping. The doping levels above and below this optimal doping are typically called over-doped (OD) and under-doped

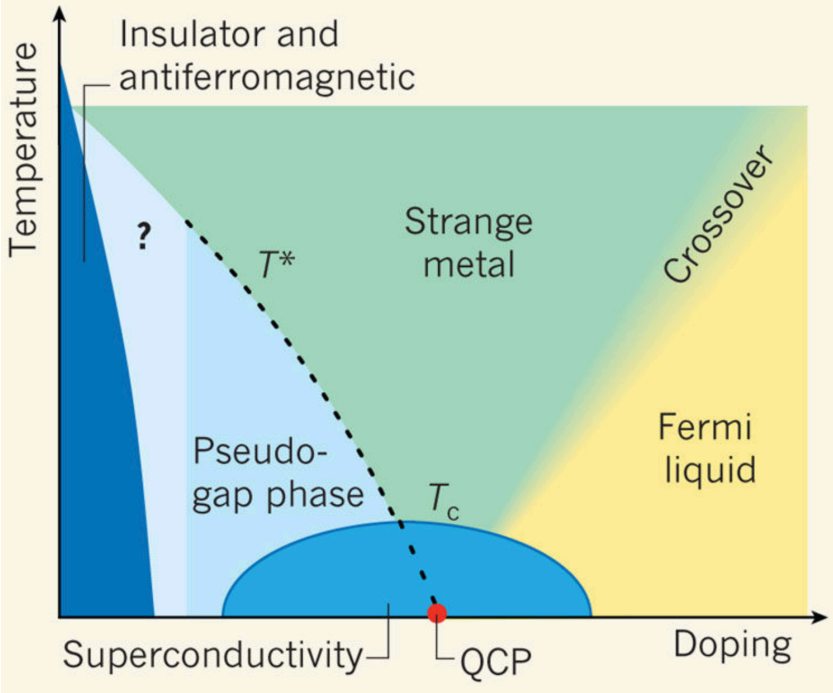

Figure 3.4: Phase diagram of hole-doped cuprate. Figure from [14]

(UD) respectively. The crystal structures of a few cuprate materials are shown in Fig. 3.5a. Most of the exotic physics, including superconductivity, originate from the copper-oxygen planes. These planes are considered to be quasi 2-dimensional, with only weak coupling between layers. (Fig. 3.5b). The superconducting gaps in cuprate materials are quite different from those in

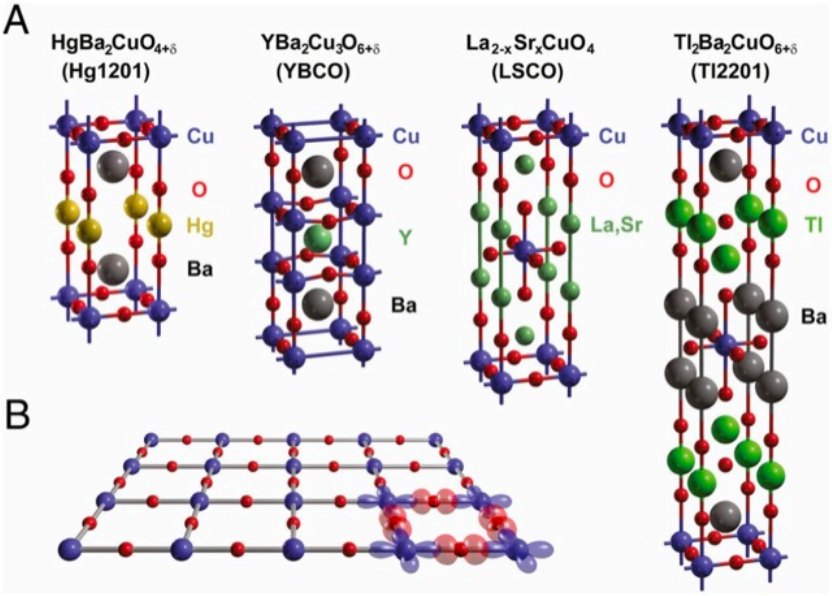

Figure 3.5: Panel a, crystal structures of a few cuprate materials. Panel b, the copper oxygen plane. Figure from [16]

conventional superconductors. They display a d-wave symmetry in k space, described by $\Delta = \Delta_0(\cos(k_x a) - \cos(k_y a))$, whereas a conventional superconductor displays an isotropic gap (s-wave) in k space. The magnitude of the d-wave gap varies from zero at the "node" in the Brillouin zone, to the maximum at the "antinode".

3.3 Nambu-Gorkov Formalism—the Superconducting Green's Function

Although BCS theory has been successful in describing many conventional superconductors, the strongly correlated nature of cuprates requires extra tools from many-body physics involving the concept of quasiparticles [5]. The superconducting Green's function (Nambu-Gorkov formalism) provides an excellent description of the quasiparticle behavior in the superconducting state

[17][18]. In the rest of this section, I will briefly present the main results of the Nambu-Gorkov formalism. The application of this superconducting Green's function to ARPES spectra and the detailed discussion of it are contained in Chapter 4.

We first introduce the original pairing Hamiltonian,

$$H_p = \sum_{k\sigma} \epsilon_{0k} c^\dagger_{k\sigma} c_{k\sigma} - \sum_{kk'} V_{kk'} c^\dagger_{k\uparrow} c^\dagger_{-k\downarrow} c_{k'\uparrow} c_{-k'\downarrow} \tag{3.1}$$

where σ denotes the spin, $c^\dagger_{-k\downarrow}$ and $c_{-k\downarrow}$ are the creation and annihilation operators for electrons, $\epsilon_{0k} = \xi_k - \mu$ is the electron energy relative to the chemical potential μ without the presence of pairing interactions, and $V_{kk'}$ is the pairing interaction. The 2-particles/2-holes term in this Hamiltonian is extremely difficult to work with. However, using the mean field approximation, the Hamiltonian can be simplified to contain only bilinear terms,

$$H_p = \sum_{k\sigma} \epsilon_k c^\dagger_{k\sigma} c_{k\sigma} - \sum_k (\Delta_k c^\dagger_{k\uparrow} c^\dagger_{-k\downarrow} + \Delta^*_k c_{k\uparrow} c_{-k\downarrow}) \tag{3.2}$$

with $\Delta_k = -\sum_{k'} V_{kk'} \langle c_{-k'\downarrow} c_{k'\uparrow} \rangle$ as the pairing order parameter in BCS theory, and absorbing a redefined chemical potential, $\epsilon_k = \epsilon_{0k} + V_0 n_{k\sigma}$, $n_\sigma = \langle c^\dagger_\sigma c_\sigma \rangle$ in the non-interacting term. Next we move on to the two-component Nambu-Gorkov field operators, which are

$$\Psi = \begin{pmatrix} c_{k\uparrow} \\ c^\dagger_{-k\downarrow} \end{pmatrix}; \Psi^\dagger = \begin{pmatrix} c^\dagger_{k\uparrow} & c_{-k\downarrow} \end{pmatrix} \tag{3.3}$$

together with the Pauli matrices:

$$\tau_0 = \begin{pmatrix} 1 & 0 \\ 0 & 1 \end{pmatrix}; \tau_1 = \begin{pmatrix} 0 & 1 \\ 1 & 0 \end{pmatrix}; \tau_2 = \begin{pmatrix} 0 & i \\ -i & 0 \end{pmatrix}; \tau_3 = \begin{pmatrix} 1 & 0 \\ 0 & -1 \end{pmatrix} \tag{3.4}$$

the pairing Hamiltonian can then be written as:

$$H_p = \sum_k \Psi^\dagger (\epsilon_k \tau_3 + \phi_1 \tau_1 + \phi_2 \tau_2) \Psi \tag{3.5}$$

where $\phi = \phi_1 + i\phi_2$ is the superconducting order parameter, same as Δ in the simple BCS case. In the case of strong coupling, Δ is defined as $\Delta = \phi/Z$ where Z is a renormalization factor that will be discussed in detail in Chapter 4. The single particle Green's function is defined as:

$$G(t) = -i \langle T \Psi(t) \Psi^\dagger(0) \rangle \tag{3.6}$$

with the time evolution field operator given by

$$\Psi(t) = e^{iH_p t}\Psi(0)e^{-iH_p t}. \tag{3.7}$$

Then applying the temporal Fourier transforms $G(\omega) = \int dt e^{i\omega t}G(t)$, we can obtain the bare Green's function:

$$G_0 = \frac{\omega\tau_0 + \epsilon_k\tau_3 + \phi_1\tau_1 + \phi_2\tau_2}{\omega^2 - \epsilon_k^2 - \phi_1^2 - \phi_2^2} \tag{3.8}$$

putting this into the inverse Dyson equation $G^{-1} = G_0^{-1} + \Sigma$ with proper parametrization of the self-energy term Σ, we obtain the Nambu-Gorkov Green's function:

$$G(k,\omega) = \frac{1}{(\omega-\Sigma)^2 - \epsilon_k^2 - \phi^2}\begin{pmatrix} \omega - \Sigma + \epsilon_k & -\phi \\ -\phi^* & \omega - \Sigma - \epsilon_k \end{pmatrix} \tag{3.9}$$

where $\phi = \phi_1 + i\phi_2$. The ARPES spectrum measures the spectral function on the particle (occupied) side, which is $A(k,\omega) = -\frac{1}{\pi}ImG_{11}(k,\omega)$. More details regarding the spectral function and its application will be discussed in Chapter 4

Chapter 4

Coherent Organization of Electronic Correlations as a Mechanism to Enhance and Stabilize High-T_C Cuprate Superconductivity

Strong diffusive or incoherent electronic correlations are the signature characteristic of the "strange metal" normal state of the cuprate superconductors, with these correlations considered to be somehow "undressed" or removed in the superconducting state. A critical question is if these correlations are responsible for the high temperature superconductivity itself. In this chapter, utilizing a new development in the analysis of angle-resolved photoemission data, we show that the strange metal correlations don't simply disappear in the superconducting state, but are instead converted into a strongly renormalized coherent state, with stronger normal state correlations leading to stronger superconducting state renormalization. Further, we show that this conversion begins well above T_C at the onset of superconducting fluctuations and that it greatly increases the number of states that can pair. Therefore, there is positive feedback—the superconductive pairing creates the conversion that in turn strengthens the pairing.

4.1 Introductions

Two main limits of electronic correlation effects exist in modern correlated electron metals: strongly coherent correlation effects and strongly diffusive incoherent correlations. Landau taught us the general principles for thinking of systems with coherent correlation effects, in which the quasiparticles (many body states that are characterized by excitations from the interaction) are the fundamental objects [5]. In these systems, strong interactions renormalize the quasiparticle

energy-momentum dispersion relation, endowing the quasiparticles with large effective masses that in certain heavy Fermion systems may be 10 or more times larger than the non-interacting electron dispersion [19]. The huge majority of concepts in modern condensed matter physics build upon this quasiparticle foundation, including the Bardeen Cooper Schrieffer (BCS) theory of superconductivity [9] and the extensions such as the Eliashberg [20] and Nambu-Gorkov theories [17][18].

The second limit of correlated electron systems with "diffusive" or incoherent interactions is generally considered to be much more exotic and rich than the first class, though because we do not have Landau's tools to visualize or understand the excitations, they are less understood. The non-superconducting "normal" or "strange-metal" state of the cuprate high temperature superconductors is typically believed to belong to this second regime of correlated electron materials, and is generally considered to be among the most exotic of any electronic material. Almost no electronic property (magnetism, thermodynamics, optics, transport, etc.) of this state behaves like that in any other material, and it is believed by some that the strong interactions make the concept of a particle useless[21]. Efforts to understand these non-quasiparticle excitations are diverse, but often bring in the concept of fractionalized excitations [21][22], utilize numerical methods to solve the Hubbard model [23][24], and/or borrow strongly from string theory and quantum gravity [25][26][27][28].

The superconducting state of the cuprates does not support these strange-metal excitations, instead, it has sharp quasiparticle-like excitations that somehow combine to form the Cooper pairs of the superconducting state. Since the superconducting state is borne from the "strange-metal" normal state, it is natural to imagine that the diffusive correlations of the strange-metal state are somehow converted or re-organized to the interactions that are responsible for the superconducting pairing. Relatively few discussions along this line exist however, with most of them centering around the idea of an "undressing" of the strange metal correlations [21][29][30][31] to reveal what has sometimes been described as a "hidden Fermi liquid" state [32].

With our development of the first 2-dimensional (2D) fitting technique for ARPES spectra, we present the first quantitative extraction of the fully causal complex electronic self-energies.

The extracted information of the electronic interactions directly confirms the general concept of the undressing of the strange-metal correlations and the unveiling of the hidden Fermi liquid, but it goes further by revealing a conversion or coherent reorganization of the diffusive strange-metal correlations into a coherent highly renormalized state at low temperature following by the enhancement of the number of states for pairing. We show how this can lead to a strong positive feedback effect that can stabilize and strengthen superconductive pairing, including favoring a strongly anisotropic (i.e. d-wave) superconducting gap. Such a new mechanism with positive feedback not only allows for much stronger pairing than would be possible from a standard strong-coupling picture within the conventional electron-boson coupling scenario, it also has the potential to enable a fully electronic (non electron-boson mediated) mechanism of superconductive pairing.

4.2 ARPES as a Self-Energy Spectroscopy

Over the past years, ARPES has made great progress at revealing certain aspects of the electronic interactions (characterized by the self-energies) of the cuprates. In particular, ARPES has discovered and provided key details of the unusual incoherent scattering or peak broadening [33][34][35] that is consistent with the "strange metal" transport [13] or "Marginal Fermi Liquid" state [36], or more precisely the "Power Law Liquid" state [33]. In contrast, using the standard language of peak tracking of quasiparticles, ARPES has described dispersion "kinks" or mass enhancements in the superconducting state in the nodal [37][38][39][40] and antinodal regime [34][41][42][43] which have been generally interpreted as indicating rather conventional electron-boson coupling, of the type for example that may act to pair electrons in a conventional non strongly-coupled electronic material. However, prior to the present work, ARPES analysis only focus on one-dimensional energy cuts (EDCs) or one-dimensional momentum cuts (MDCs) [31][33], but not both together—an issue that is not important when the peaks are sharp and the scattering rates are low like in a Fermi Liquid. In strongly correlated superconductors like cuprates, the complications of the peak broadening, the renormalization effect, and the spectral gap make a quantitative extraction of the band dispersions and self-energies from ARPES possible only in certain special cases. In particular,

along the nodal direction where there is a linearly dispersing band with relatively high velocity, the self-energies can be extracted through MDC analysis [33][38][39][40], but this method fails for mid-zone or antinodal cuts, in which more complicated structures come in with the spectral gap and a strong kink feature below T_{pair} . Whereas near the antinode, the sharp quasiparticle peak below Tc allows the relatively flat band dispersion to be extracted by EDC analysis, the EDC method fails when the gap starts to disappear near or above T_C [34][41][42][43]. Thus, the MDC and EDC methods can only provide qualitative result in certain cases, and in the general case they may give very different results from each other [44]. Moreover, slight warpage, doping heterogeneity, or any other surface conditions of the sample may lead to undesirable broadening in the spectra, which add in more complexity for extracting the intrinsic broadening effects through 1D methods. These problems can be overcome with the two-dimensional (2D) fitting of spectral function convolved with extrinsic energy and momentum broadening and forcing the real and imaginary parts of self-energy to have full causality. Therefore, previous studies have only been able to focus on certain parts of the Brillouin zone or certain temperature ranges (below or above TC) and these studies only extracted qualitative feature from part of the self-energy (either the real or imaginary part within a certain energy range) [37][38][39][40][34][41][42][43].

Our work provides a new analysis tool of a full 2D fitting technique, treating both EDCs and MDCs simultaneously and on an equal footing, while also drastically reducing the number of free fitting parameters. Another new and important advance of this technique is that the self-energy $\Sigma(k, \omega)$ has been constrained to be automatically Kramers-Kronig (KK) consistent, i.e. the obtained self-energies explicitly obey causality, whereas the 1D MDC and EDC methods have no restrictions on causality. The self-energies extracted from spectra covering a wide temperature range and the full Brillouin zone provide a more comprehensive picture of the electronic interactions that was not achievable in the previous studies with simple one-dimensional MDC or EDC methods.

4.3 2-Dimensional Fitting to ARPES Spectra

4.3.1 Experimental Results and Fits

Fig. 4.1 and Fig. 4.2 show raw data sets and matching 2D fits from a lightly underdoped T_C=85K $(Bi,Pb)_2Sr_2CaCu_2O_8$ superconductor. The Pb-doping removes the 5:1 superstructure that can add contamination to the antinodal portions of the spectra [45][46]. ARPES measurements were taken at beamline 5-4 Stanford Synchrotron Radiation Lightsource, and at beamline 9A at the Hiroshima Synchrotron Radiation Source. The samples were cleaved and measured in an ultra-high vacuum chamber with the pressure maintained below 3×10^{-11} Torr. We used 9 eV photons for the temperature dependent set of data in Fig. 4.1 and 24 eV photons to cover the full Brillouin zone (data in Fig. 4.2). These two photon energies are selected to minimize the matrix element of the bonding band and enhance the anti-bonding band [47][48]. The energy resolution was 5.5 meV with 9 eV photons and 10.5 meV with 24 eV photons. The count rate nonlinearity of the electron detector is corrected [49]. The data was taken over a rather large energy range so as to capture the large energy scale features as well as the low energy scale features such as the superconducting gaps. The data from Fig. 4.1 were taken near the middle of the zone (partway between the node and antinode, cut shown in Fig. 4.1 panel d) and show the evolution of the various features as a function of temperature from deep in the superconducting state into the normal state. Fig. 4.2 was taken in the superconducting state and shows how these features evolve as we move from near the node towards the antinode.

All the spectra in this chapter are symmetrized along $k = 0$. A weak energy-dependent background, presumably from elastically scattered electrons, is subtracted from each spectrum before fitting. This background is determined by measuring the counts at the edge of the spectrum as shown in Fig. 4.3.

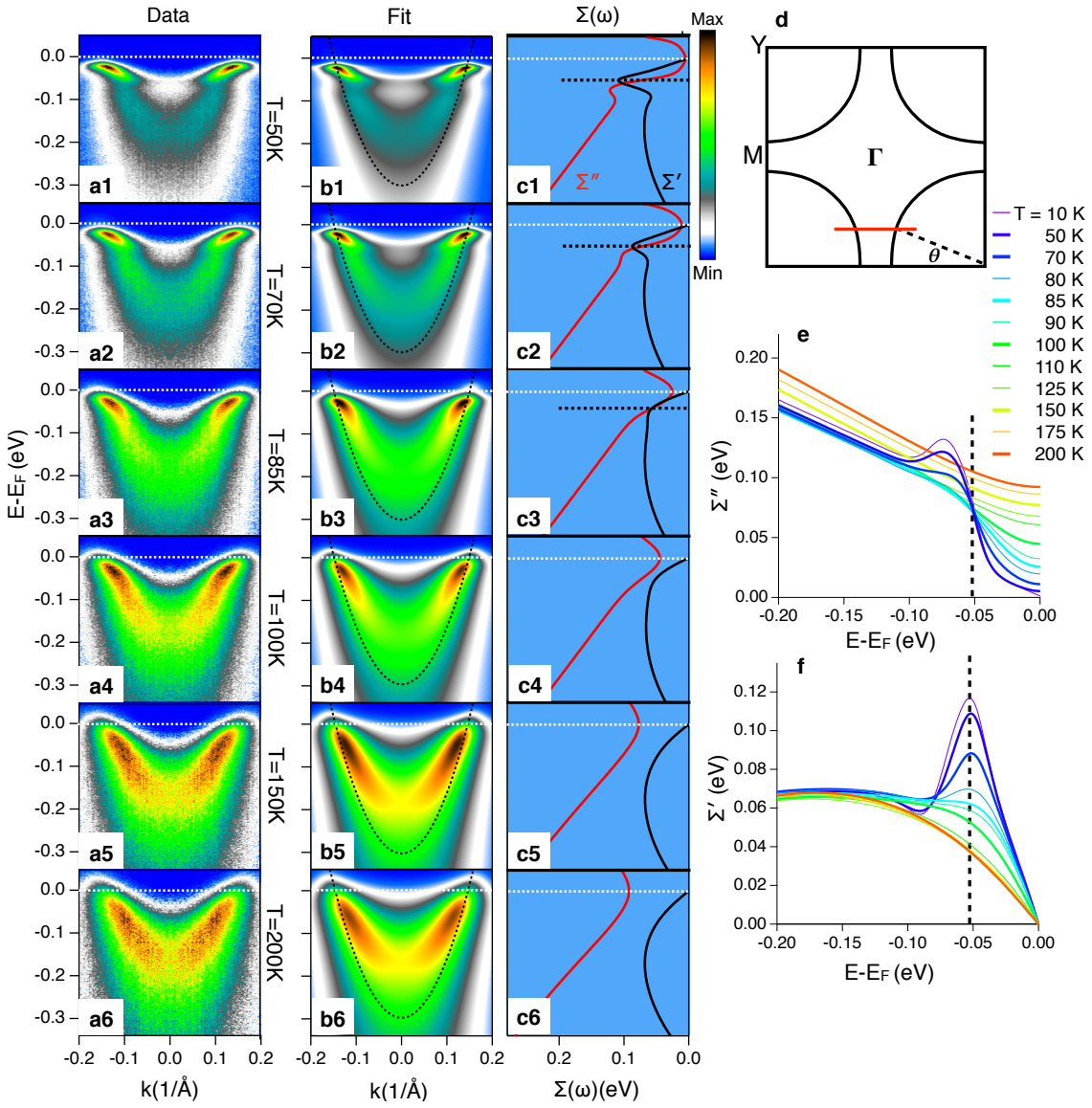

Figure 4.1: Mid-zone ARPES spectra, fits, and self-energies of a lightly underdoped T_C = 85K superstructure-free Pb-BSCCO sample. Panel a1-a6, measured spectra from a mid-zone cut (panel d) of the antibonding band at multiple temperatures. Panel b1-b6, 2D fits to the corresponding ARPES spectra, with the main unknown parameters the superconducting gaps, the electronic self-energies and the bare electron band, where the dotted curve is the bare band dispersion from the fitting. Panel c1-c6, correspondent self-energies extracted from the fit spectra on the left. Panel e, Imaginary part of the self-energy (or scattering rate) vs. frequency and temperature obtained from the 2D fits of the b panels. There is a strong reduction or gapping of the near-EF scattering rate as temperature is lowered into the paired state, along with a shift of this scattering to high energies beyond the dashed line. Along with this is a strong kink or mass enhancement in the real part of self-energy (panel f). These effects of and are responsible for the dramatic flattening and sharpening of the low energy states of panels a and b. All data were taken with 9 eV photons, and the Fermi surface angle was θ= 22.5 degree.

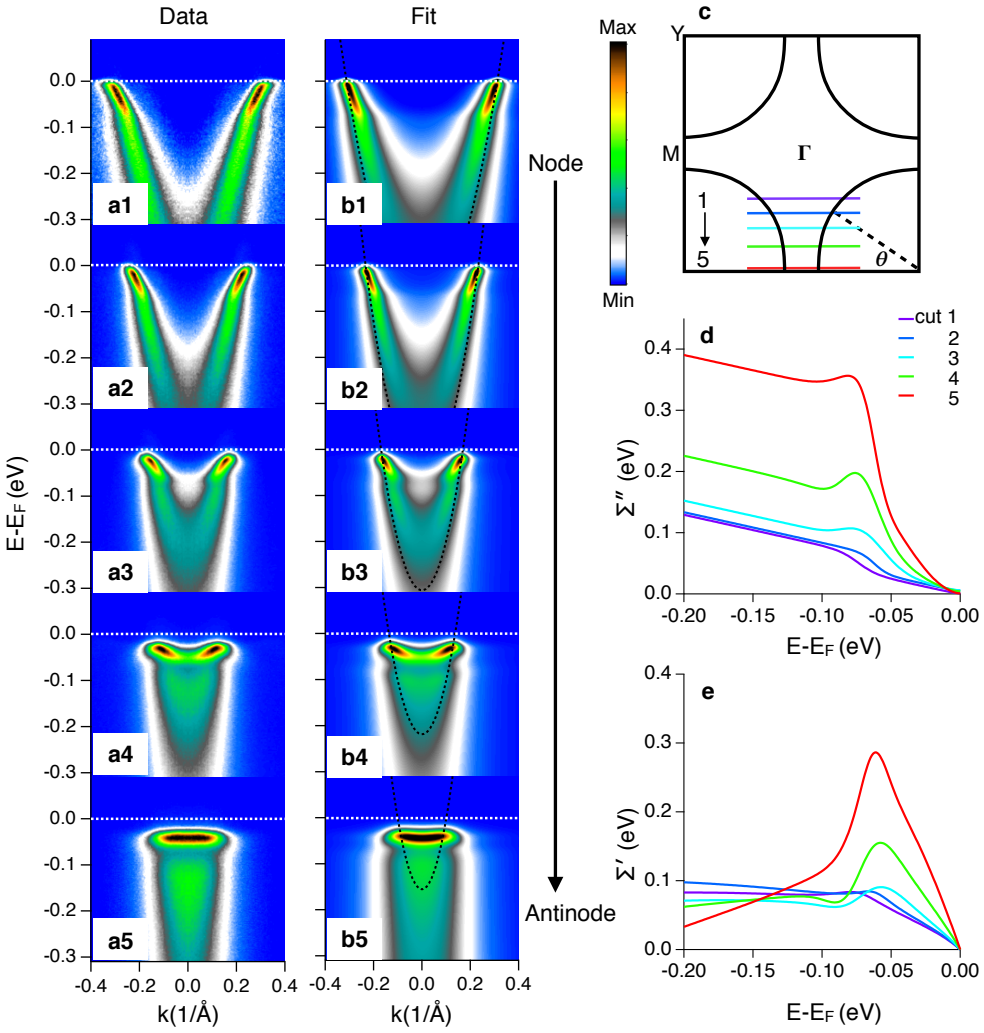

Figure 4.2: Dramatic growth of the electronic self-energies towards the antinodal regime. Panel a1-a5, measured T=15K superconducting state ARPES data along cuts 1-5, as shown in panel c. In panel a5 the states near E_F are almost dispersionless, i.e. extremely massive. Panel b1-b5, corresponding 2D fits of the spectra, where the dotted curve is the bare band dispersion from the fitting. Panel d, extracted imaginary part of the self-energy Σ'' at the 5 cuts in k-space. Panel e, extracted real self-energy Σ' at the 5 cuts in k-space. The huge mass enhancement of the low energy antinodal states of cut 5 is captured by the large magnitudes of Σ'' and Σ' for cut 5. All data were taken with 24 eV photons, and the sample was the same as used for Fig. 4.1.

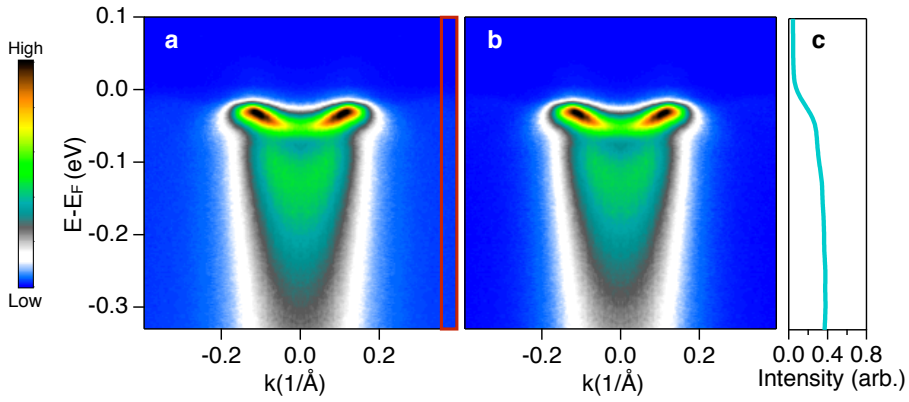

Figure 4.3: Example spectrum without (panel a) and with (panel b) background subtraction. Panel c, the energy-dependent background, which is the averaged and smoothed EDC within the red box in panel a.

4.3.2 2-Dimentional Fitting Method

The entire ARPES cut as shown in Fig. 4.1 and Fig. 4.2 is fitted to a spectral function multiplied by a Fermi function and broadened by experimental resolution, which can be written as:

$$I_{ARPES} = I_0[A(k,\omega) \times F(\omega,T)] \otimes R(\omega,k) \tag{4.1}$$

where I_0 is the prefactor of spectral intensity, $A(k,\omega) = -ImG_{11}(k,\omega)/\pi$ is the spectral function (imaginary part of the Greens function), $F(\omega,T)$ is the Fermi function and $R(\omega,k)$ is broadening function in both energy and momentum. We use the conventional Nambu-Gorkov formalism for superconductivity [17][18] for theoretically describing these spectra.The 2×2 Greens function matrix is:

$$G(k,\omega) = \frac{1}{(\omega-\Sigma)^2 - \epsilon_k^2 - \phi^2} \begin{pmatrix} \omega - \Sigma + \epsilon_k & -\phi \\ -\phi & \omega - \Sigma - \epsilon_k \end{pmatrix} \tag{4.2}$$

The G_{11}term describes the electron removal portion, which is:

$$G_{11}(k,\omega) = \frac{\omega - \Sigma + \epsilon_k}{(\omega-\Sigma)^2 - \epsilon_k^2 - \phi^2} \tag{4.3}$$

where Σ is the energy-dependent self-energy term that modifies the bare energies (real part of the self-energy Σ' and widths Σ'', imaginary part of the self-energy Σ), ϵ_k is the bare band dispersion, and ϕ is the pairing order parameter (with $\phi = Z(\omega) \times \Delta$, where $Z = 1 - \frac{\Sigma'(\omega)}{\omega}$ and Δ is the superconducting gap).

As all the two dimensional ARPES spectra in this chapter are taken along the $(\pi,0)$–(π,π) direction, a parabolic function with only two parameters (band bottom and k_F position) is used as the bare band instead of a more complicated tight binding model. We construct the phenomenological imaginary self-energy $\Sigma''(\omega)$ for each spectrum with minimal parameters and use the Kramers-Kronig relation, which is $\Sigma'(\omega) = \frac{1}{\pi}\int \frac{\Sigma''(\omega')}{\omega'-\omega} d\omega'$, to obtain the real part. We chose the integration range to be ±5 eV, such that a larger range does not change the integration result. While we allow for particle-hole asymmetry for the electronic structure (i.e. parabolic band dispersions), we have constrained the self-energies to be particle-hole symmetric. We found that

eight parameters in total are sufficient for constructing the self-energy for any one cut. We will discuss the details of constructing the self-energy later. Together with the extrinsic broadening terms (one for energy resolution and one for momentum broadening accounting for surface condition and sample heterogeneity), superconducting gap (real constant, but also checked for a complex energy-dependent option, discuss in later section), bare band dispersion (two parameters), and the prefactor for the spectral function, there are only 14 fitting parameters in total for the two dimensional ARPES spectra below T_C. Each two-dimensional ARPES spectrum in this chapter has over 10^5 data points. The ratio of fitting parameters to data points is therefore 1/6000. In a typical EDC or MDC analysis, a functional form of about 5 parameters is used to fit each EDC or MDC that contains about 300 to 400 data points (parameters to data points 1/60). Therefore, the ratio of parameters to data points in our 2D fitting method is two orders of magnitudes smaller than the 1D analysis technique. Some previous studies have simulated ARPES spectra with a theory based or phenomenological self-energy to achieve reasonably good simulation result that resemble the experimental data taken from cuprates well below the superconducting transition [50][51]. Our analysis technique is the first fitting method that applies to the ARPES spectra with temperature ranging from well below the superconducting transition to well above it and with spectra taken from the node to the antinode.

In essence, we are using a conventional quasiparticle-like approach for both the normal and superconducting states, with the exception that there is a complicated and large self-energy term Σ that captures the interactions (and the departure from true Landau quasiparticle physics). That both the superconducting state and normal state spectra can be so well described within this semi-conventional approach is in itself a surprising finding: the generally broad structures and large backgrounds observed in ARPES spectra of cuprates have often been described as being so far outside the realm of conventional physics that such semi-conventional quasiparticle-like approaches were considered untenable [21].

The key new information obtained from our study is that of the self-energies $\Sigma = \Sigma' + i\Sigma''$ (directly related to the electronic interactions), which we find vary dramatically as a function of

energy, temperature, and from node to antinode, as shown in Fig. 4.1e, f and Fig. 4.2d, e, which will be discussed in more detailed in section 4.4.

4.3.3 Impact of the Form of the Self-Energy

To show the construction of the self-energy, Fig. 4.4 panel a-f demonstrates how the gapped imaginary self-energy and the kink in the real part of the self-energy affect the ARPES spectra. All spectra in Fig. 4.4 are simulated with the same superconducting gap and bare dispersion with the parameters extracted from fitting to spectra in Fig. 4.2 panel a4. Fig. 4.4 panel a shows a simulated spectrum with self-energy of the Marginal Fermi liquid form [36] (more specifically the Power Law Liquid form [33] as shown in Fig. 4.4b, which can be written as:

$$\Sigma''(\omega) = \lambda\sqrt{\omega^2 + (\pi k_B T)^2} + \Gamma_0 \tag{4.4}$$

where λ is set to 0.5, Γ is 80 meV, and T is 15 K. The real part of the self-energy is obtained from the Kramers-Kronig relation. Compared with the ARPES data (Fig. 4.2a4), the example spectrum of Fig. 4.4a shows little feature from the superconducting gap (even though the gap has been input to the simulation) and it lacks the sharp feature near EF as well as a strong band renormalization. Then in Fig. 4.4c, we replaced with one equivalent to the one extracted from our 2D fitting method (4.4 panel d). Because we havent yet adjusted Σ'', Σ'' and Σ' no longer adhere to the Kramers-Kronig relation. Although the spectrum shows a strong band renormalization from the Σ', there is still no sharp spectral peak and little feature from the superconducting gap due to the large Σ'' that broadens the quasiparticle coherence peak and heavily fills in the superconducting gap. In the next step (4.4 panel e), we put in the full self-energy that is extracted from our 2D fitting method, which especially includes a strong drop in the scattering rate at low frequencies. The simulated spectral function in panel e now very closely resembles the experimental spectra, including the clear superconducting gap, the strong spectral weight near E_F, the kink and peak-dip-hump features, etc., all of which originate from the form of the self-energy.

In the final step (4.4 panel g), we convolve the spectrum with an energy and momentum

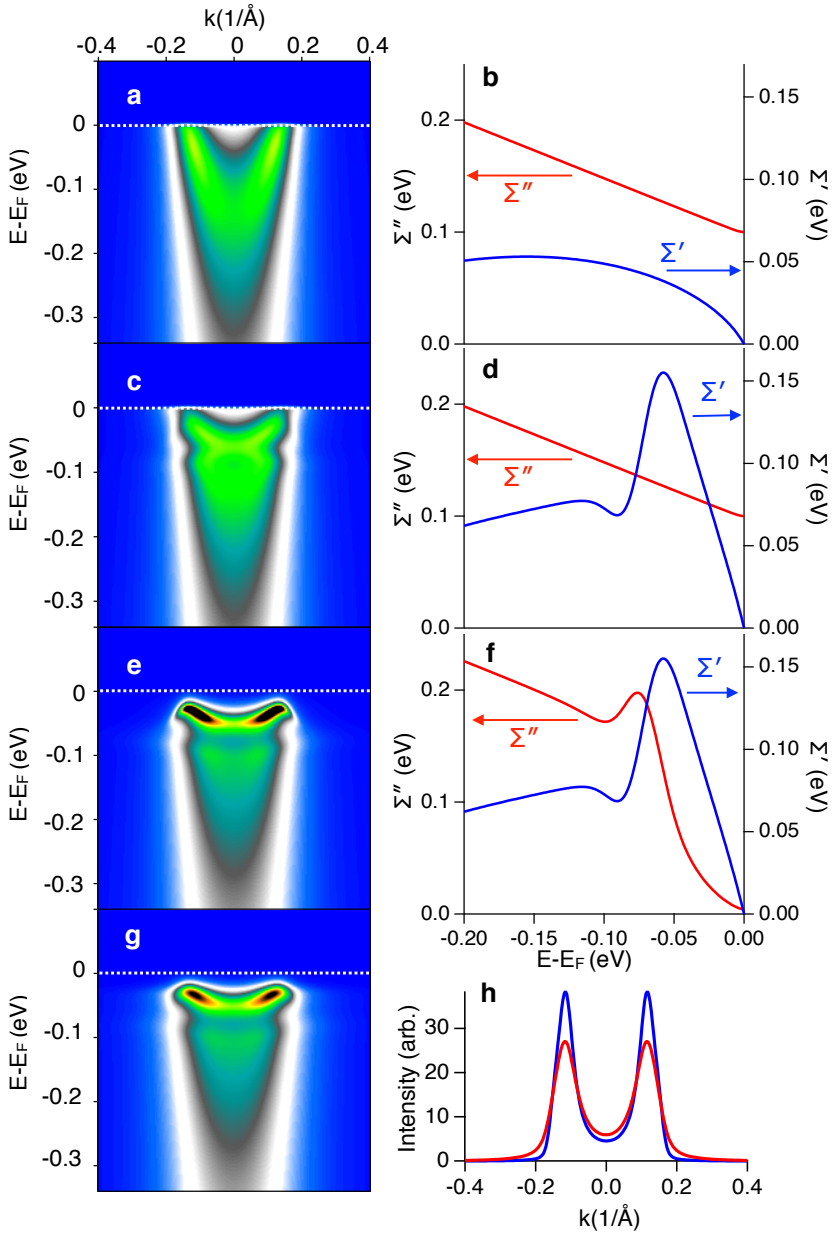

Figure 4.4: Phenomenological construction of the self-energy. Simulated spectra illustrating the effect of various forms of self-energy. The self-energies of panel d are not causally self-consistent, and are shown for illustrative purposes only. Color scales are the same for spectrum in panel a to g. h, The comparison of MDCs with (red) and without (blue) extrinsic broadening.

broadening function. The energy broadening is the measured energy resolution that is calibrated from the gold Fermi edge taken near the sample position with the same experimental conditions as the data from the superconductor. For this spectrum taken with 24 eV photons, the total energy resolution is 10.5 meV. The momentum broadening is added in to account for various intrinsic and extrinsic broadening factors, such as the angular-resolution of the electron analyzer, the imperfections of the cleaved surface (like surface warpage), and the doping heterogeneity of the single crystal sample that has been commonly observed in scanning tunneling spectroscopy [52]. This extrinsic momentum broadening can vary slightly with different samples, cleaved surfaces or even different photoemission spots on the same cleaved surface. Thus, we put in the momentum broadening as one of the fitting parameter for the low temperature spectrum and then hold this constant for all fits as a function of temperature. For the spectrum shown in 4.4g, the momentum broadening is 25 mÅ^{-1}. In 4.4 panel h, we compare the two different MDC cuts from the spectrum with (red) and without (blue) additional momentum broadening.

4.3.4 Terms in the Self-Energy

As discussed in section 4.3.2, 8 terms are utilized to parameterize the self-energy for each slice, and two terms (k_F and the band bottom) are used to parameterize the bare band structure. Along with the energy and momentum broadening terms, the superconducting gap, and the prefactor for the spectral function, the experimental spectra can be very well fit.

In our study we used the 8 terms to parameterize $\Sigma''(\omega)$ for each experimental cut, letting the energy dependence of $\Sigma'(\omega)$ to be fully determined by the Kramers-Kronig relations. We found that as long as the 8 terms give enough freedom to the fits, the exact functional form of $\Sigma''(\omega)$ is not so important, indicating the overall robustness of the fitting procedure (see Fig. 4.5).

Two forms of that we utilized are:

$$\Sigma''(\omega) = \lambda\sqrt{\omega^2 + (\pi k_B T)^2} + \frac{I_1}{e^{\frac{\omega - E_1}{W_1}} + 1} + I_2 e^{\frac{-(\omega - E_2)^2}{2W_2^2}} + \Gamma_0 \tag{4.5}$$

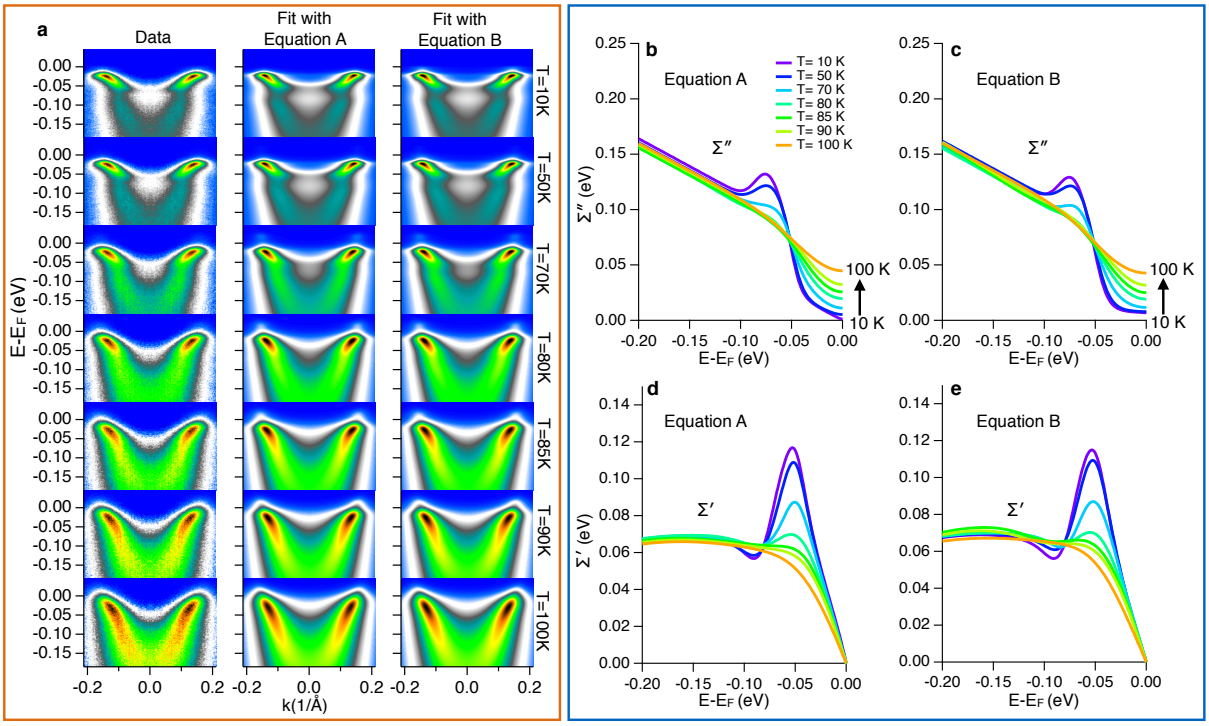

Figure 4.5: Self-energy constructed with different functional forms. Panel a, data and the fits with two different functional form to construct the imaginary self-energy, where equation A corresponds to equation 4.5, equation B corresponds to equation 4.6. Panel b and c, the imaginary part of the self-energy extracted from the fittings. Panel d and e, The real part of the self-energy that extracted from the fitting.

$$\Sigma''(\omega) = (\lambda\sqrt{\omega^2 + (\pi k_B T)^2} + \Gamma_0) \times (\frac{I_1}{e^{\frac{\omega - E_1}{W_1}} + 1} + 1 - I_1 + I_2 e^{\frac{-(\omega - E_2)^2}{2W_2^2}}) \quad (4.6)$$

Each of these is essentially a Marginal Fermi Liquid together with a step function at E_1 and a Gaussian function peak at E_2. All of the fits shown in Fig. 4.1 and Fig. 4.2 are obtained using the form of equation 4.5, while Fig. 4.5 shows a comparison of results obtained using the two functional forms.

Equations 4.5 and 4.6 contain the 8 parameters λ, Γ_0, I_1, E_1, W_1, I_2, E_2, and W_2. An extensive study of the temperature and energy dependence of the scattering rates in the normal state of the cuprates indicated that λ for nodal states of optimally doped samples should be near 0.5 [33]. We found that this value worked well for the temperature dependence set of data shown in 4.1, thus we set it to 0.5 for the momentum dependent set of data at 15 K shown in 4.2.

An additional term we utilized is a cutoff energy ω_c that brings $\Sigma''(\omega)$ to zero at high frequencies, which is necessary for the Kramers-Kronig transformation to work. Kordyuk et al [53]. have reported the cutoff energy scale to be around 500meV - our finding of the cutoff energy is consistent with that result.

4.3.5 Particle-Hole Symmetry

To justify our assumption of particle-hole symmetry on the self-energy ($\Sigma''(\omega)$ to be even and $\Sigma'(\omega)$ to be odd over E_F), in Fig. 4.6, we show a set of 2D fitting result with the self-energy that is enforced to be particle-hole asymmetric. The intensity on the hole side of the $\Sigma''(\omega)$ is forced to be larger or smaller than the particle side (Fig. 4.6a). The goodness of the fit the chi-square value shown in Fig. 4.6c indicates that the fit with particle-hole symmetry actually has the best fit quality (the smallest chi-square). On the other hand, Fig. 4.6a-b show that even under different condition of particle-hole asymmetry in the self-energy, both $\Sigma''(\omega)$ and $\Sigma'(\omega)$ (inset in Fig. 4.6b) reveals an energy-dependent behavior that is quantitatively robust on the particle (occupied) side, except for a constant shift in $\Sigma'(\omega)$. The extracted spectral gap sizes in Fig. 4.6d also shows a small variation (the standard deviation is only 0.7meV for the average 20meV gap size). In Fig. 4.6panel

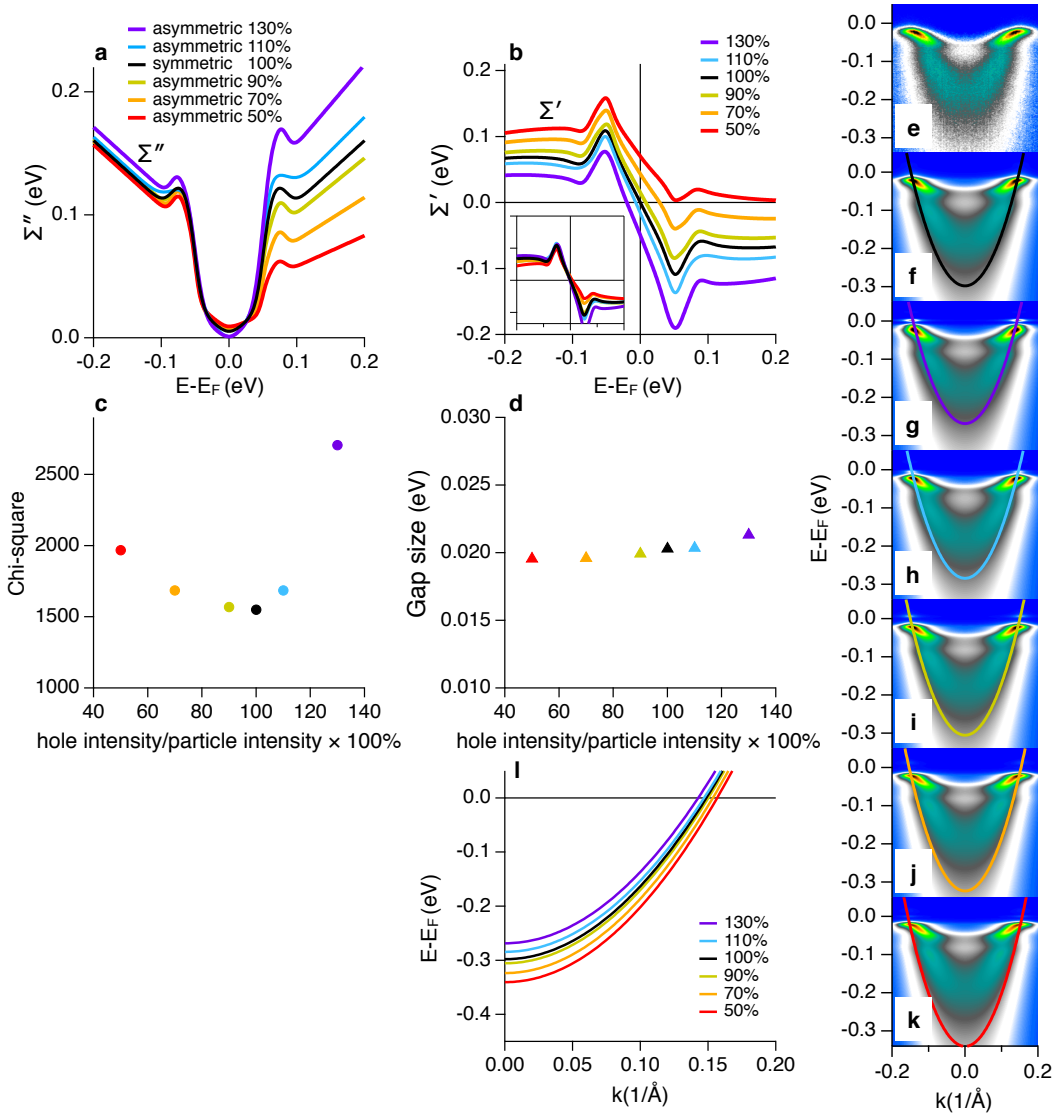

Figure 4.6: 2D fitting with enforcing particle-hole asymmetry. Panel a, the extracted imaginary part of the self-energy $\Sigma''(\omega)$ from 2D fitting, with the intensity of $\Sigma''(\omega)$ on the hole side enforced to be 130%, 110%, 100% (particle-hole symmetric), 90%, 70%, and 50% of the particle (occupied) side. Panel b, the correspondent real part of the self-energies $\Sigma'(\omega)$, where the inset shows the $\Sigma'(\omega)$ with the offset to be $\Sigma'(0) = 0$. Panel c, the statistical chi-square value of each fit, indicating the goodness of the fit (the smaller the chi-square, the better the fit). Panel d, the spectral gap size from each 2D fitting, which shows a small variation with standard deviation to be 0.7 meV comparing with the average gap size of 20 meV. Panel e, ARPES spectrum of the mid-zone cut taken at 50 K (same as in Fig. 4.1a1). Panel f to k, The fit spectra with different particle-hole symmetry and asymmetric condition, where panel f is the same fit as in Fig. 4.1a1 with the assumption of particle-hole symmetry, g to k are the spectra with particle hole asymmetry where the intensity of $\Sigma''(\omega)$ at the hole side is 130%, 110%, 90%, 70%, 50% of the particle side respectively. The colored curves are the correspondent bare band dispersions. Panel l, the extracted bare band dispersions.

e to k, we show the correspondent fit results of different particle-hole symmetry and asymmetry condition together with the bare band dispersion. The extracted bare band dispersion (Fig. 4.6 panel l) shows a shift in energy, which compensate the shift in the $\Sigma'(\omega)$. As ARPES only probe the particle (occupied) side of the spectral function, the particle-hole symmetry has long been an assumption in the analysis of ARPES spectra, especially in the common used symmetrized EDC method [31] that proved to be a useful technique to extract the spectral gap size and the scattering rate. In the symmetrized EDC method, both the density of state and self-energy is assumed to be symmetric, whereas our 2D fitting technique only assumed the symmetry on self-energy but not on the density of state. Based on the discussion above, we can conclude that the particle-hole asymmetry on self-energy only brings in minor affect to our results, where the behavior of both $\Sigma''(\omega)$ and $\Sigma'(\omega)$ is quantitatively robust. And the particle-hole symmetry assumption is justified as it returns the best fitting result judging by the statistical chi-square.

4.3.6 Energy-Dependent Complex Order Parameter and Superconducting Gap

In conventional strongly coupled superconductors, it is found that the pairing interaction can be strongly retarded, which brings in an energy dependence to the pairing order parameter (related to the superconducting gap). Because of causality (the Kramers-Kronig relations), any energy dependence of the order parameter necessitates that it be complex, having both real and imaginary parts.

To explore this physics, we performed fits with an energy-dependent complex superconducting order parameter. In this case we write $\phi(\omega) = \phi'(\omega) + i\phi''(\omega)$ which then corresponds to an energy-dependent complex superconducting gap $\Delta(\omega) = \phi(\omega)/(1 - \frac{\Sigma(\omega)}{\omega})$. We utilized 5 terms to allow for the energy dependence of $\phi''(\omega)$ as:

$$\phi'' = \frac{1}{e^{\frac{\omega - E_3}{W_3}} + 1} + \frac{1}{e^{\frac{-\omega + E_4}{W_4}} + 1} \tag{4.7}$$

and utilized the Kramers-Kronig transformation to obtain $\phi'(\omega)$. As is typical, we also enforced ϕ'' to be odd in ω and ϕ' to be even.

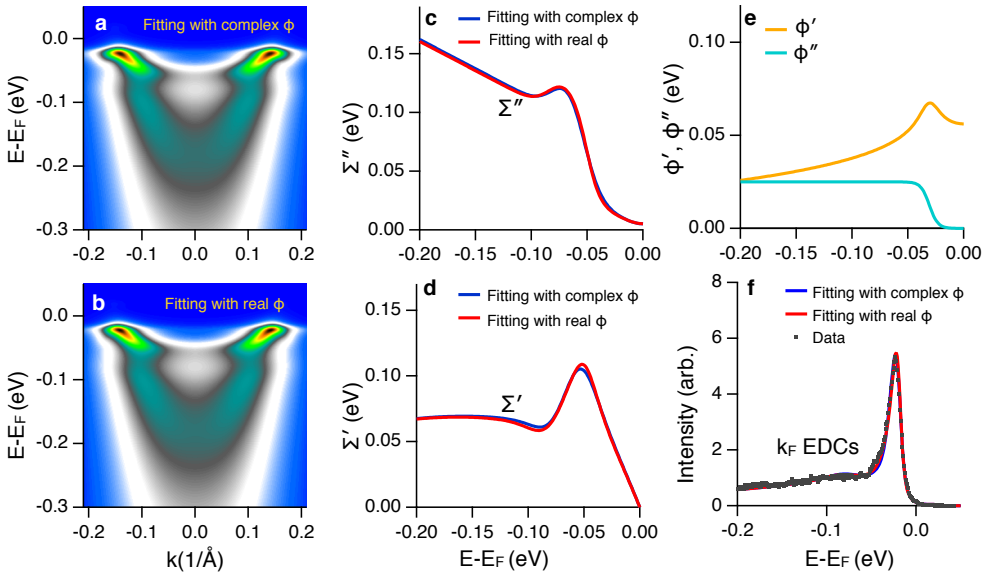

Figure 4.7: Fitting with a complex superconducting order parameter. Panel a, fitting the spectrum of Fig. 4.1 panel a1 with a complex superconducting order parameter ϕ. Panel b, the fit result with only a real ϕ (what we used for all other fitting in this chapter), the color scale is the same with panel a. Panel c and d, imaginary and real part of self-energy for these two different fitting. Panel e, the complex order parameter for the spectrum in panel a. Panel f, the kF EDC of spectra in panel a and b and the experiment data that they fit to.

Fig.4.7 shows a comparison between the fits obtained with the complex energy-dependent (complex energy-dependent) and the one with a real-only ϕ, where $\phi = \Delta \times Z$ and Δ is a real constant. The results for ϕ' and ϕ'' are shown in panel e. Even though there are many more parameters, the results and qualities of the fits with the real-only and the complex are almost identical. These results clearly show that the energy dependence of ϕ and Δ is much less important than the energy dependence of Σ, i.e. any energy dependence of the pairing interaction is a second-order effect.

A previous ARPES study [54] reported a significant energy dependence to the complex superconducting gap and a complex order parameter. This contrasts with our results (Fig. 4.7), which are equally well fit with a simpler real static gap. Here we discuss a few other differences between the two studies: First, the previous study was limited to the near-node and mid-zone regions, where the kink strengths are much weaker. Second, the previous study exclusively utilized the conventional 1D MDC fitting method, since the 2D method was not available to them at that time. This includes momentum cuts inside the gap region which do not have any true poles and where there are many fewer constraints. The self-energies extracted in this gap region showed a very strong or even dominant peak that they attribute to impurities [54][55]. However, unlike the 55 meV kink feature, this strong low-energy feature in the self-energy cannot be observed directly from the corresponding ARPES spectrum. Such an extra peak is not present in the self-energies that we extract with the 2D fitting method.

Our results show that the single particle self-energy and its energy dependence are much more important than any effects of the energy dependence of the superconducting gap or order parameter, and that these self-energy effects are in general critical to the physics of the cuprates.

4.3.7 Comparison of 1D and 2D Fit Results

Fig. 4.8 shows the comparison of the data and the fit in 1D cuts (EDCs and MDCs) from the temperature dependent set of data that is shown in Fig. 4.1. Three different temperatures of data and fit that lie in different regions of the phase diagram are shown as typical examples.

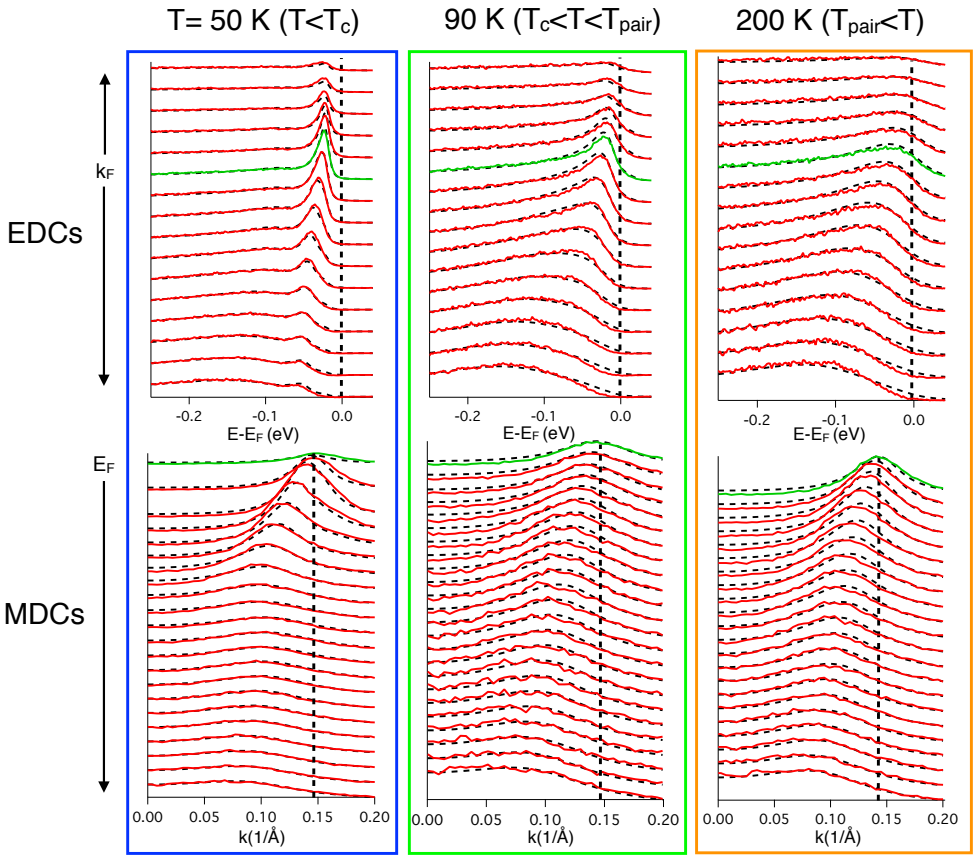

Figure 4.8: MDC and EDC line cuts from the experimental data (red solid) and fits (black dashed) from the mid-zone $\theta = 22.5$ color scale plot of Fig. 4.1. In contrast to the standard method in which all EDCs and MDCs are individually fit and individually scaled in amplitude, all spectra for one temperature were fit simultaneously, with no additional amplitude scaling or other modifications. This is a much more severe constraint than utilized in previous fitting studies of ARPES data.

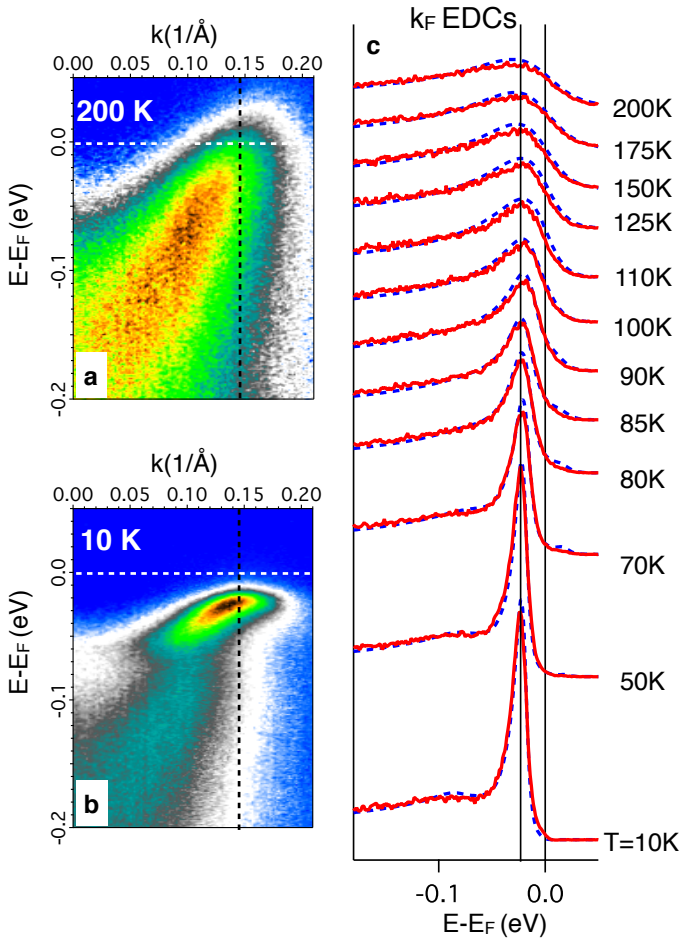

Figure 4.9: Temperature dependence of the quasiparticle peaks, from the mid-zone $\theta = 22.5$ cut. Panel a and b, 2D ARPES spectra at two extreme temperatures. Panel c, EDCs (red solid) from these and similar plots at $k = k_F$, i.e. along the vertical black dashed line in panel a and b. Line cut through the 2D fits to these data are shown as the blue dashed lines in panel c. The quasiparticle peak sharply emerges between T_{pair} and T_C.

The EDCs and MDCs of the data and fit indicate a very high fitting quality of our 2D fitting method that is comparable to those using phenomenological model fitting to only EDCs or MDCs [31][37][41][42][43][54][55][56] though the fitting using the 2D method effectively contains 100 times fewer fitting parameters.

Fig. 4.9 shows a quasiparticle peak view from k_F EDCs. As a complimentary tool to the false color scale spectra, the k_F EDCs from spectra of various temperatures in Fig. 4.1 show the evolution of quasiparticle coherence. The quasiparticle peaks sharply emerge between T_{pair} and T_C—behavior that has been qualitatively described in a previous study [56], and attributed to the onset of the superfluid density (a property of the 2-particle pairs) in the superconducting state. Here, we understand that this is due to the strong evolution of the single particle self-energies $\Sigma'(\omega)$ and $\Sigma''(\omega)$.

4.3.8 Pseudogap

In underdoped cuprates, a commonly known feature pseudogap that can be observed at much higher temperature scale well above the T_{pair} has attracted a lot of interest in high-T_C superconductivity research. Though the pseudogap is presented in the (underdoped) sample we studied, its presence is a relatively minor effect, which is why we dont discuss it prominently in the thesis. Fig.4.10 shows a comparison of spectra taken at the mid-zone and near the antinode with temperature below and above T_C. The symmetrized k_F EDC of the high temperature (150K) spectrum taken near the antinode displays a spectral weight depletion with weak coherence peak near the Fermi level (pseudogap) that is absent in the mid-zone. This k-dependence is consistent with previous reports [57]. This pseudogap feature is observable up to a temperature scale $T*$ that is much higher than the pairing temperature scale T_{pair} mentioned in the present chapter. This difference in these two temperature scales is consistent with other recent findings [58][59][60]. On the other hand, both the mid-zone and the near antinodal spectra exhibit a similar trend when moving into the superconducting state. At high temperature (150K), they both have broad and incoherent spectra, whereas at temperatures well below T_C (50K), the spectra display sharp and

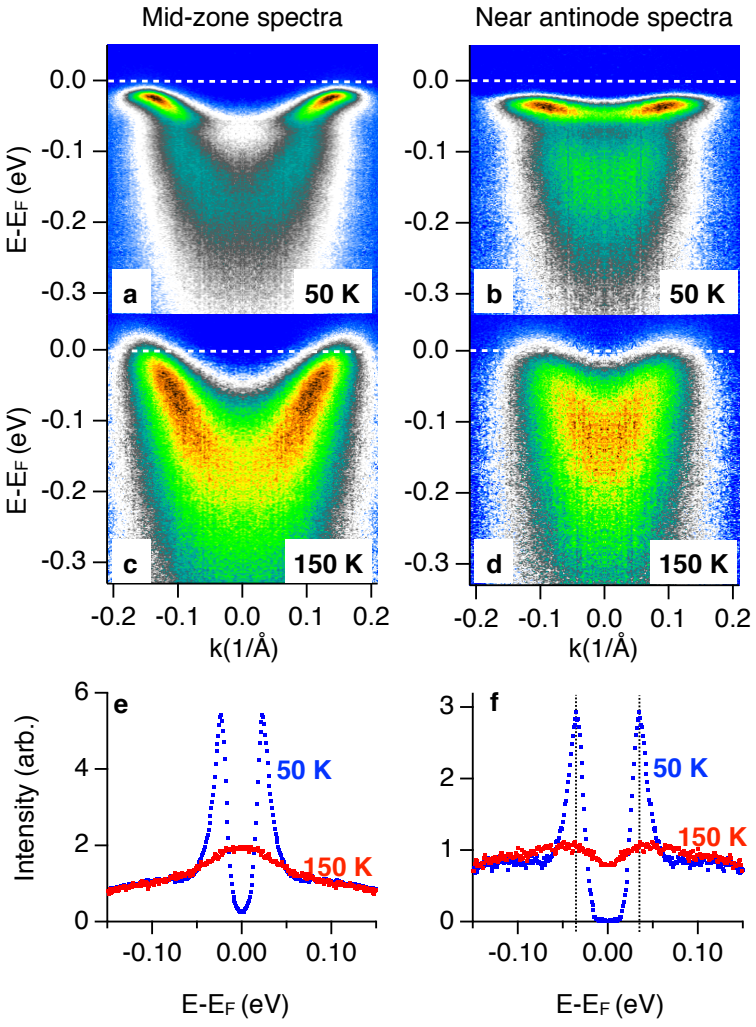

Figure 4.10: Comparing spectra at mid-zone and near antinodal region. Panel a and b, Low temperature spectra (T=50K) taken at the mid-zone (Fermi surface angle at 22.5 degree) and near the antinode (32 degree). Panel c and d, The same set of spectra taken at 150K. Panel e and f, symmetrized k_F EDCs of the mid-zone and near antinodal spectra at 50K and 150K. The correspondent symmetrized EDC of the near antinodal spectrum at 150K shows a strong depletion of the spectral weight near Fermi level (pseudogap), whereas the mid-zone one doesnt show any gap feature at 150K.

strongly renormalized quasiparticle peaks. This is also revealed by the strong quasiparticle peaks in the symmetrized k_F EDCs at low temperature compared to the broad curves at high temperature. The change in the general behavior is observed to begin at T_{pair} (Fig. 4.13 panel a), i.e. it is dominated by the pairing physics rather than the pseudogap physics.

4.4 Results: the Self-Energies Effect and Positive Feedback Loop

4.4.1 The Behavior of Self-Energies in Energy, Momentum and Temperature

We initially focus on the spectral widths or scattering rates (Σ) as shown in Fig. 4.11 panel a (the spectra and fits are shown in 4.1), beginning with the high temperature (T=125K) normal state data, which is smoothly varying as a function of energy, with a linear-like dependence on energy at high energies and a quadratic-like dependence at lower energies. The data also shows that the overall value of the scattering rate at all energies in this high temperature regime increases smoothly with temperature. Both of these are the expected behavior of the "strange metal" [13] or "Marginal Fermi Liquid" state [36], or more precisely the "Power Law Liquid" state [33]. Beyond just the functional form of Σ'' we also get information about the absolute value of the scattering rates, which are in general very high—ranging from 100 meV at EF to about 190 meV at 200 meV binding energy for the 200K spectrum, as shown in Fig. 4.11a. These large scattering rates are the reason for the overall broad spectra shown in Fig. 4.1 panels a5/b5 and a6/b6, with the broadening somewhat larger at deeper energies as described by the curves of Fig. 4.11a. These large normal state scattering rates are a critical aspect of the strongly correlated state of the cuprates, which we will come back to later.

As the sample is cooled below approximately 125K we begin to see subtle and then more dramatic changes in the spectrum of Σ'', with a slow and then rapid decrease of Σ'' in the low energy (<60 meV) portion of the spectra. With the decrease in Σ'' at low energies, the low energy peaks in the spectral function become noticeably sharper, as seen most clearly in Fig. 4.1 panels a1/b1, qualitatively consistent with previous ARPES results [37][34][41][42][43]. The sharp energy

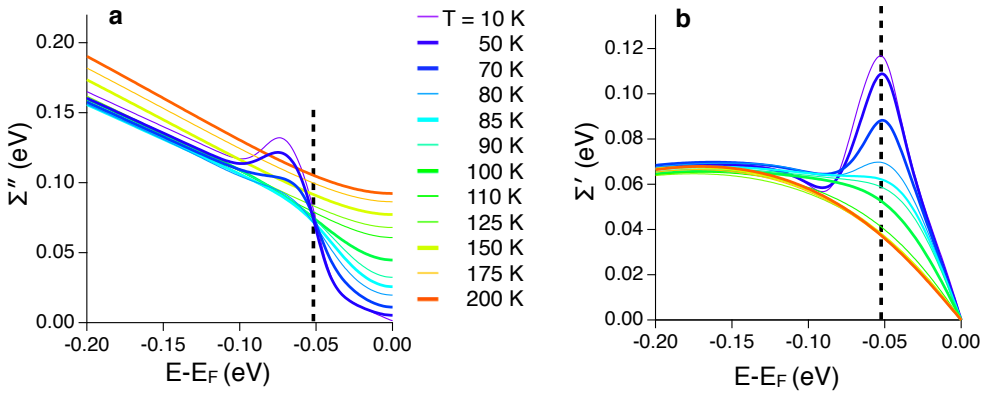

Figure 4.11: Temperature dependent self-energies. Panel a, the temperature dependent imaginary part of the self-energies extracted from 2D fitting of the mid-zone cut (also shown in 4.1 panel e). Panel d, the real part of the self-energies (also shown in 4.1 panel f)

step in the undressed Σ'' brings in dramatic changes in Σ'. In particular, the low temperature step increases in Σ'' centered at approximately 55 meV leads to a strong peak in Σ' at that same energy due to the Kramers-Kronig relations that derive from causality. This effect is absent at the highest temperature and strongest at the lowest temperatures. Σ' renormalizes the band energies, pushing the bare band energies ϵ_k towards EF by the amount of Σ', leading to two key consequences: a dispersion "kink" appears at the energy where Σ' is maximal (∼55 meV) and the dispersion of the low energy bands are flattened/made more massive, by an amount equal to the "renormalization factor" $Z = 1 - \frac{\partial \Sigma'}{\partial \omega}|_{\omega=E_F} \sim 3$ for the low temperature data of Fig. 4.11b. The same energy scale appears as the step in $\Sigma''(k,\omega)$, peak in $\Sigma'(k,\omega)$, and "kink" in $A(k,\omega)$ and is about 55 meV, consistent with previous results from the antinodal regime [34][41][42][43].

Fig. 4.12 shows how the low temperature self-energies vary across the Brillouin zone, moving from the near-nodal regime (top) to the antinodal regime (bottom) (the spectra and fits are in 4.2). In addition to the superconducting gap in the spectral function growing as we move to the

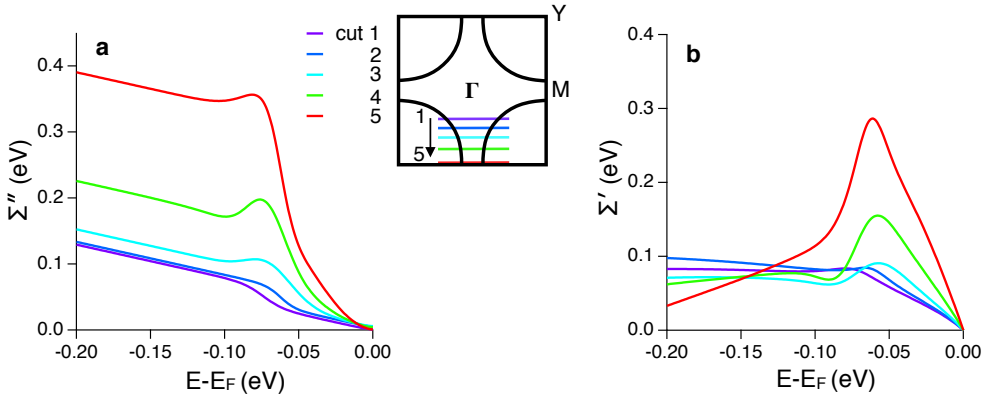

Figure 4.12: Momentum dependent self-energies. Panel a, the momentum-dependent imaginary part of the self-energies extracted from 2D fitting of the mid-zone cut (also shown in 4.2 panel d). Panel d, the real part of the self-energies (also shown in 4.2 panel e)

antinode we see that the quasiparticle dispersion becomes flatter and flatter from node to antinode, with a correspondingly stronger dispersion kink or renormalization effect. This evolution of the renormalization effect is seen in both Σ'' (Fig. 4.12 panel a) and Σ' (Fig. 4.12 panel b), as the

self-energies are in general larger and more dramatically varying at the antinode than at the node. In particular, Σ'' in the high energy portion of the antinodal spectrum is extremely large with a magnitude ∼350 meV, compared to the still-large magnitude of 120 meV for the near-nodal spectrum. Because the very low energy/low temperature portion of Σ'' has an extremely small value of ∼2 meV, this means that the antinodal states have a much stronger step decrease in the scattering rate Σ'' with energy and a correspondingly stronger peak in Σ', giving rise to a huge kink effect and almost dispersionless (extremely massive) states near EF (Fig. 4.2 panel a5/b5). Therefore, the larger the Σ'' is, the larger is the kink in Σ'.

4.4.2 Conversion of Self-Energies

In Fig. 4.13 panel a, we plot the temperature evolution of the renormalization effects at the mid-zone cut of 22.5 degrees (raw data in Fig. 4.1) as well as the temperature evolution of the superconducting energy gap from that same data set. $\Sigma''(E_F)$ (red squares of Fig. 4.13a) is seen to decrease gradually with decreasing temperature (as expected for a Marginal Fermi Liquid [36] or Power Law Liquid metal [33]), but then take a steep dive at the onset of the superconductive pairing T_{pair}, as also determined by the temperature at which the pairing gap reaches zero (orange circles of Fig. 4.13a). Concomitant with the drop in $\Sigma''(E_F)$ is a rapid rise in Σ' (blue diamonds of Fig. 4.13a), i.e. the large imaginary part of the self-energy is converted into a large real part of self-energy (and hence large renormalization factor Z) as the temperature is lowered and the pairing fluctuations begin.

Figure 4.13b shows the fit of the spectrum at the antinode at 15K (same as the left half of Fig. 4.2b5) together with the quasiparticle locus (renormalized dispersion - blue) and the gapped bare band (red). The renormalization at the antinode is so huge that the quasiparticle dispersion at the gap edge is almost completely flat. This effect is characterized by the renormalization factor Z (equivalent to the inverse of the quasiparticle residue), which is 6.5 for the present case at the antinode, with a value slightly less than 3 near the node (blue triangles, Fig. 4.13 panel c). In a non-gapped metal this renormalization parameter would also be the mass enhancement

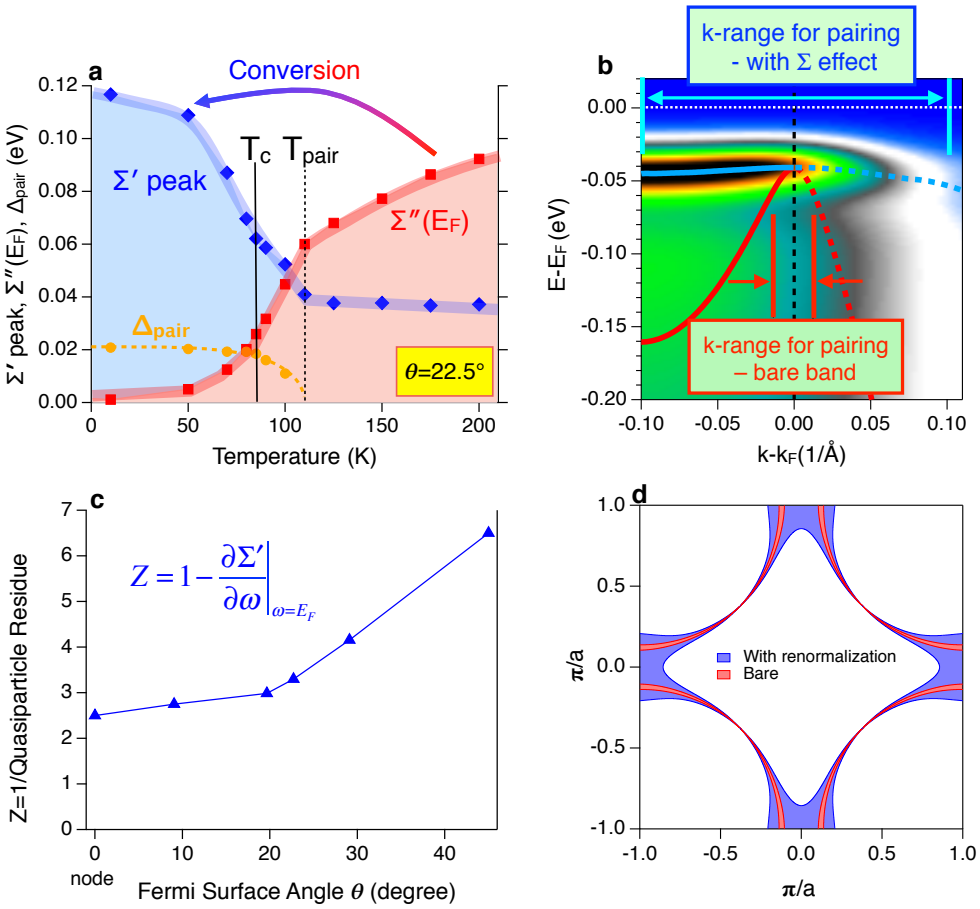

Figure 4.13: More details of the effects of the self-energies. Panel a, temperature dependence of gaps and self-energies of the $\theta = 22.5$ mid-zone cut of Fig. 4.1. Parameters shown are Real part of Σ' peak (blue diamonds Σ value along the dashed line in Fig. 4.11b), $\Sigma(E_F)$ (red squares zero frequency portion of Fig. 4.11a), and superconducting gaps (orange circles extracted from fits of Fig. 4.1). Upon cooling from high temperature, the main evolution of the parameters begins at T_{pair} and not at T_C. Panel b, reproduction of the right half of the spectrum of Fig. 4.2 panel b5 (antinodal states, cut 5, T=15K), with the renormalized quasiparticle dispersion (blue curve), and the extracted bare-band dispersion with no self-energies (red curve) overlaid on the spectrum. The superconducting gap is 40 meV. Also shown is the range of k-states contributing to pairing, which is significantly larger for the renormalized band (blue) than for the bare band (red). Panel c, quasiparticle renormalization factor Z (blue triangles) in the superconducting state as a function of Fermi surface angle, reaching the very large value of 6.5 at the antinode. Panel d, the effective k range for pairing in the Brillouin zone, where the effective k range with renormalization cover 11% Brillouin zone, the bare one only covers 2% Brillouin zone.

m*/m (ratio of second derivatives of the band dispersion). Such a huge renormalization factor and mass enhancement is beyond the regime of the conventional electron-phonon coupling described by Migdal-Eliashberg theory. The concept of self-energy conversion that we discuss here is such a mechanism, with a larger initial Σ'' leading to a stronger renormalization factor Z.

Previous ARPES studies of cuprates have discovered dispersion kinks or mass enhancements near the Fermi level in the near-nodal [38][37][39][40], and antinodal regime [41][42][43], which have been generally interpreted as indicating electron-boson coupling, with the debate centering on whether the boson is phononic or magnetic in origin, or both [4][61][62]. It is important to distinguish the near-nodal and antinodal regimes, as these behave quite differently—the near–nodal kinks are generally significantly weaker, are at slightly higher energy, and have only a weak temperature dependence. The case for electron–boson coupling, and electron–phonon coupling in particular, for these near-nodal states is relatively strong, including an isotope effect study on the near-nodal kinks [40]. In contrast, the mid-zone and antinodal kinks discussed in the present work are much stronger than these nodal kinks, with a renormalization factor (6.5 at the antinode, as shown in Fig. 4.13c) that is so strong we argue that it is beyond what is possible from the standard Eliashberg theory that are typically used for the description of electron-boson coupling in conventional strongly-coupled superconductors.

4.4.3 Enhancement of the Number of States for Pairing

A critical aspect of the huge band renormalization/mass enhancement is that it brings many states that were originally far from E_F up towards the Fermi level. If these new states are brought within an energy scale comparable to the pairing energy (within $\sqrt{2}\Delta$ of E_F, see discussion in the next paragraph), then these new states will strongly participate in the superconductive pairing. This effect is illustrated in Fig. 4.13 panel b, where there is an approximately 7-fold increase in the number of k-states contributing to the particle-hole mixing of superconducting pairing. As for the entire Brillouin zone (Fig. 4.13 panel d), we find that this effect brings a 5-fold increase in the number of paired k-states (blue) compared to the situation without the renormalization effect.

The effective momentum range of particle-hole mixing shown in Fig. 4.13 panel b and d is the full width at half maximum (FWHM) of the particle-hole mixing probability $u_k^2 v_k^2 = \frac{\Delta^2}{4(\xi_k^2+\Delta^2)}$, where $v_k^2 = \frac{1}{2}(1 - \frac{\xi_k^2}{\xi_k^2+\Delta^2})$, and $u_k^2 = \frac{1}{2}(1 + \frac{\xi_k^2}{\xi_k^2+\Delta^2})$ are the coherence factors for particles and holes respectively, in which ξ_k is the ungapped electron dispersion, and Δ is the superconducting gap. The value of $u_k^2 v_k^2$ indicates the probability of particle-hole mixing. As $u_k^2 v_k^2$ peaks at k_F, where $\xi_k = 0$, the FWHM of $u_k^2 v_k^2$ is where $\xi_k = \pm\Delta$, thus the electron energy at the half maximum is $E_k = \sqrt{\xi_k^2 + \Delta^2} = \sqrt{2}\Delta$. Considering the renormalization effect, ξ_k is then equal to ϵ_k/Z, where ϵ_k is the bare electron band dispersion and Z is the renormalization factor discussed previously. The particle-hole mixing range of the full Brillouin zone shown in Fig. 4.13d is calculated with the ξ_k, Z, and Δ extracted from the 2D fitting of the ARPES spectra shown in Fig. 4.2, after interpolating the parameters of those five cuts to the whole Brillouin zone.

Figure 4.14 summarizes the temperature evolution of the electron spectral function and the self-energy conversion, i.e. how the correlation effects are converted from giving a strongly diffusive (large Σ'') low mass state at high temperatures to a coherent (low Σ'') mass-enhanced state (Z or Σ' effect) in the superconducting state. In particular, at the first formation of a gap in the spectral function $A(k,\omega)$ at around T_{pair}, we start to get a gapping of the low energy portion of Σ'', as illustrated in panel b2. The newly-created steep step increases in Σ'' automatically (through the Kramers-Kronig relations) leads to a strong peak in Σ' (Fig. 4.14b3). The stronger is the step in Σ'', the stronger is the peak in Σ' and the larger the dispersion kink and mass renormalization, as quantified by the magnitude of Σ' and Z. Within this picture the huge (6.5-fold at the antinode) renormalization that we observe in the superconducting state is therefore directly attributable to the anomalously large diffusive scattering rate in the normal state. This large mass enhancement is beyond the simple concepts of "undressing" of the normal state correlations as discussed in the previous works [21][29], as in those ideas the normal state correlations were removed, not converted. The conversion effect described here also has similarities to the Kondo effect observed in heavy Fermion materials, in which high temperature incoherent correlations give rise to a highly massive coherent state at low temperature [19].

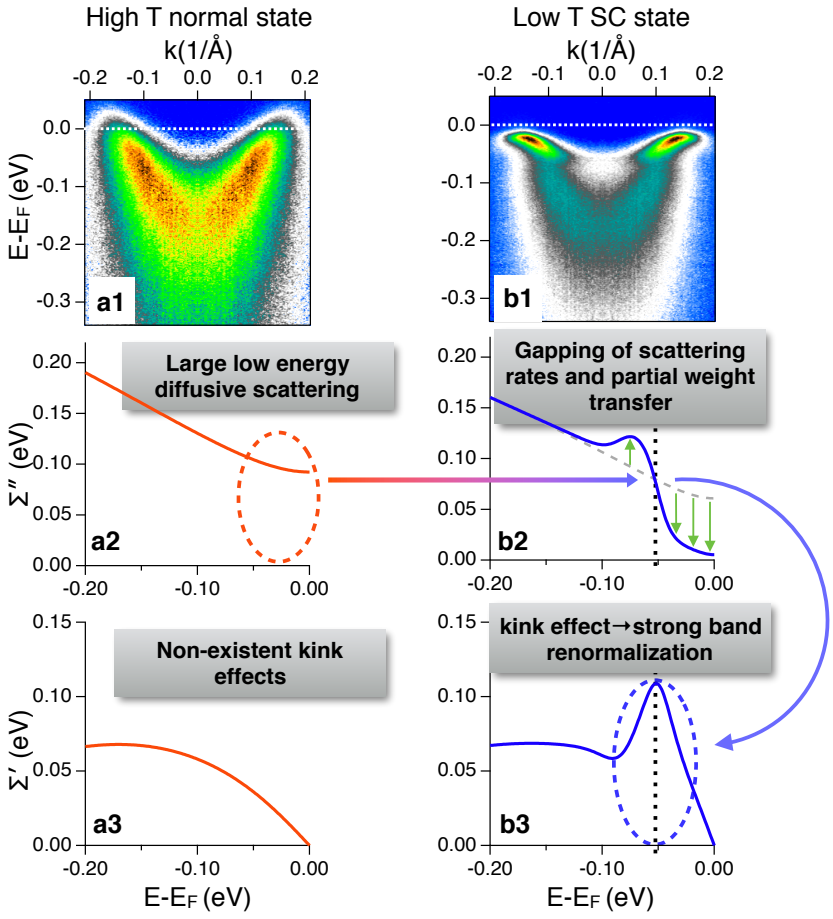

Figure 4.14: Conversion of electronic correlations. This figure summarizes the temperature evolution of the electron spectral weight $A(k,\omega)$ (top panels) and the electron interactions $\Sigma(k,\omega)$ (middle and lower panels). Panel a2 highlights the large low energy Σ'' (incoherent scattering) that is present in the normal state. Panel b2 shows that as the temperature is lowered into the superconducting state this low energy incoherent scattering is undressed, i.e. the low energy portion of Σ'' tends towards zero below the energy of the dashed line, along with a slight increase in at higher energy. Among other things this creates the well-defined quasiparticle states in $A(k,\omega)$ at low energy of panel b1. Causality requires that associated with this change in Σ'' is a change in Σ', as observed in b3, which shows the strong kink effect/mass renormalization. Hence the large diffusive scattering above T_C is converted to a strong kink effect and mass renormalization an effect that is much larger for the antinode than the node because the normal state diffusive scattering is much larger for the antinode than the for the node.

4.4.4 The Positive Feedback Loop

Our observations point towards the possibility for a positive feedback on the pairing process that can dramatically enhance and stabilize superconductive pairing. The idea is illustrated in Fig. 4.15, and is as follows: (1) Any onset of pairing fluctuations in the electronic spectrum $A(k,\omega)$ will start to open a gap in $A(k,\omega)$ which due to the removal of low energy electrons from which to scatter, will reduce the phase space for electron-electron scattering. This reduced phase space for low-energy electron-electron scattering implies the opening of a gap in the low energy portion of $\Sigma''(k,\omega)$. (2) Because of causality and the Kramers-Kronig relations, the gapping in $\Sigma''(k,\omega)$ leads to strong peaks in $\Sigma'(k,\omega)$, which give a strong coherent band renormalization effect in $A(k,\omega)$ (Fig. 4.1) that is strongest for the antinodal states (Fig. 4.2). (3) This low energy coherent band renormalization brings an increase in the number of low energy k-states available to participate in the pairing (Fig. 4.13 panel b and d), i.e. the effect of the pairing on $A(k,\omega)$ is enhanced by the changes in $\Sigma(k,\omega)$. (4) Since the gap in $A(k,\omega)$ enhances the changes in $\Sigma(k,\omega)$, and the changes in $\Sigma(k,\omega)$ enhance the changes in $A(k,\omega)$, we propose that a positive feedback loop is created that should strengthen and stabilize the superconductive pairing. This feedback effect should favor an anisotropic (e.g. d-wave) pairing channel since the self-energy effects are much greater at the antinode than near the node (Fig. 4.12a,b and Fig. 4.13c), and the effect can in general be very strong because of the very large overall strength of $\Sigma''(k,\omega)$ in these materials.

4.5 Conclusion

In summary, the extracted self-energies from data shown in Fig. 4.1, 4.2 and 4.13 not only quantitatively confirm the undressing behavior of Σ'' and the kink feature as the peak of Σ' from previous studies, but more importantly they provide the direct observation of the conversion of the self-energy as shown in Fig. 4.11a,b and Fig. 4.13a. Moreover, we present the evolution of the electron correlation effects from different parts of the Brillouin zone, with these strong renormalization effects providing a strong enhancement to the pairing state as shown in Fig. 4.13

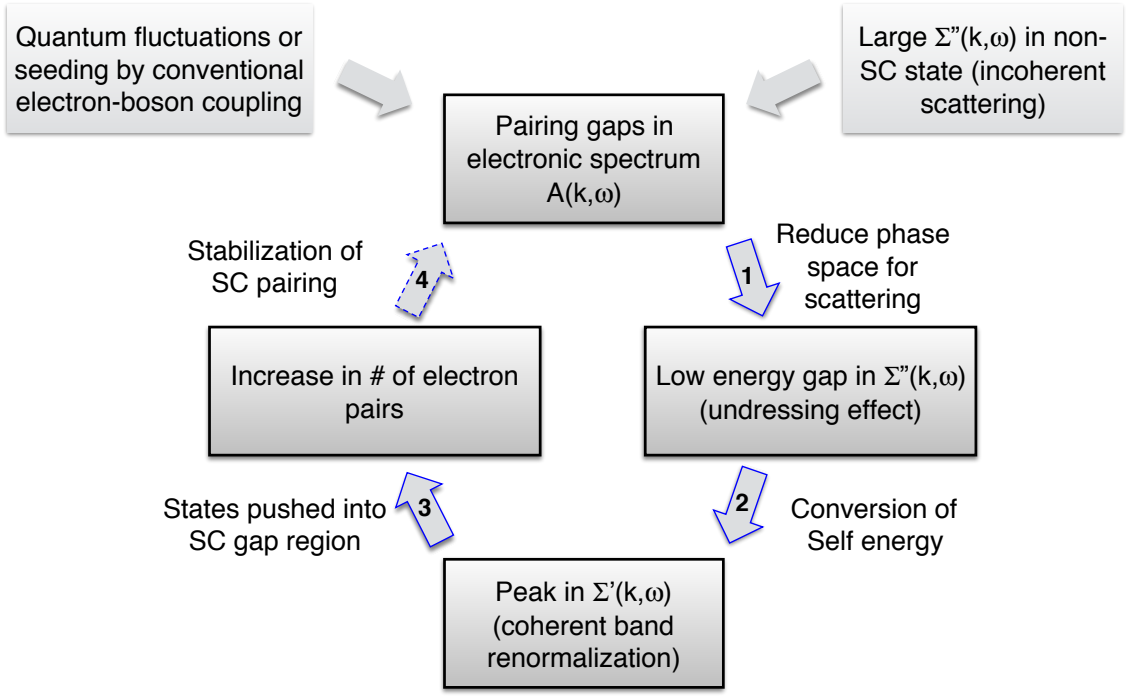

Figure 4.15: Proposed positive feedback effect between $A(k,\omega)$ and $\Sigma(k,\omega)$ enhancing and stabilizing the superconducting pairing. 1) The onset of pairing fluctuations (gapping) in the electronic spectrum $A(k,\omega)$ will start to open a gap in the scattering spectrum $\Sigma''(k,\omega)$ because of the removal of the low energy electronic states. 2) Then as shown in Fig. 4.14 the gapping and weight transfer in $\Sigma''(k,\omega)$ leads to strong peaks in $\Sigma'(k,\omega)$ which give a strong mass enhancement in $A(k,\omega)$. 3) This low energy band renormalization brings an increase in the number of low energy k-states available to participate in the pairing (Fig. 4.13 panel b and d), i.e. the effect of the pairing on $A(k,\omega)$ is enhanced by the changes in $\Sigma(k,\omega)$. 4) This enhancement in the pairing can feed back to the original pairing fluctuations of step 1), helping to strengthen and stabilize them. This mechanism is possible because of, or enhanced by, the huge incoherent scattering rate $\Sigma''(k,\omega)$ present in the strange metal incoherent normal state.

panel b and d, giving evidence of a positive feedback loop as described earlier and illustrated in Fig. 4.15.

In general, a positive feedback or "bootstrapping" mechanism such as we describe has the potential to strengthen and stabilize any type of superconductive pairing mechanism, regardless of the "initial" mechanism of pairing (electron-phonon, electron-spin resonance, spinon pairing/RVB physics, etc.). More interestingly, we note that this new mechanism also gives a potential route towards a purely electronic (boson-free) pairing mechanism, where the initial pairing gap in $A(k, \omega)$ could be seeded by quantum fluctuations alone. Regardless of the specific mechanism for the pairing, the strength of the positive feedback effect depends upon the strength of the incoherent normal state scattering, and presumably also the details of this incoherent scattering. Of course, understanding the details of this diffusive normal state self-energy at high temperatures also has remained elusive, capturing the attention of physicists from a great range of disciplines [23][25][26]. That the interactions (Σ' and Σ'') that drive this strange-metal state are essentially fully gapped when the low energy electrons in $A(k, \omega)$ are gapped, is in itself an important clue about the origin of the strange metal state, which should therefore be largely or fully electronic in origin. Even more, seeing how this strong diffusive scattering can be converted to strong coherent effects that can enhance and stabilize superconductivity opens a potential new path for engineering such effects into other materials, possibly with higher transition temperatures.

Chapter 5

Spectroscopic Evidence of Low Energy Gaps Persisting Towards 120 Kelvin in Surface-Doped *p*-Terphenyl Crystals

The possibility of high temperature superconductivity in organic compounds has been discussed since the pioneering work of Little in 1964 [7], with unsatisfactory progress until the recent report of a weak Meissner shielding effect at 120 Kelvin in potassium-doped para-terphenyl samples [8]. To date however, no other signals of the superconductivity have been shown, including the zero resistance state or evidence for the formation of the Cooper pairs that are inherent to the superconducting state. In this chapter, using high-resolution photoemission spectroscopy on potassium surface-doped para-terphenyl crystals, we uncover low energy gaps that persist to approximately 120 K. Among a few potential origins for these gaps, we argue that the onset of electron pairing within molecules is most likely. And while pairing gaps are a prerequisite for high temperature superconductivity they do not guarantee it. Rather, the development of long-range phase coherence between the paired states on the molecules is necessary, requiring good wavefunction overlap between molecular states something that is in general difficult for such weakly overlapping molecules.

5.1 Introductions

Para-terphenyl is a simple organic molecule composed of three benzene rings arranged end-to-end, as illustrated in Fig. 5.1a, and it is available commercially at a modest price. These molecules can be packed together in single crystalline form (Fig. 5.1c), in which case the molecules arrange

themselves in a unidirectional stacking as shown in Fig. 5.1b. The experiments that reported the weak (less than 0.1% shielding) Meissner shielding effect were prepared from non-crystalline *p*-terphenyl powders, annealed with potassium in an evacuated tube at temperatures between 443 and 533 K. Meissner signals from these experiments initially formed at 7 K [63], with subsequent experiments yielding signals beginning at 43 K [64] and finally 120 K [8]. The evolution with time in the onset temperature presumably has to do with the doping level of the K in the samples and/or the cleanliness/quality of the samples.

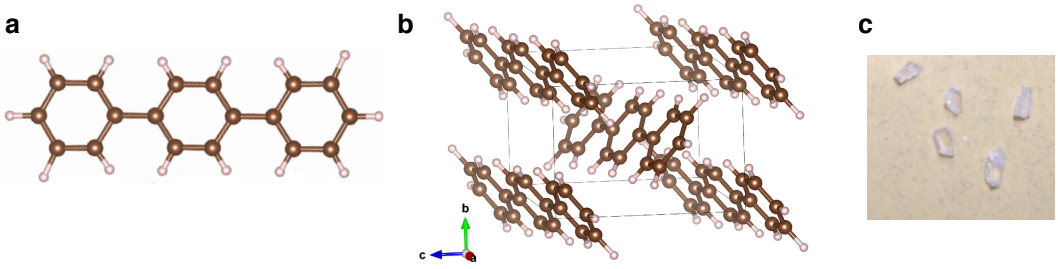

Figure 5.1: *para*-terphenyl crystal. Panel a, *p*-terphenyl molecule. Panel b, *p*-terphenyl molecules arranged in a single crystal. Panel c, pictures of our bulk crystals of *p*-terphenyl.

The Meissner effect is just one signature of superconductivity, so it is in need of confirmation from other techniques such as transport or spectroscopy, with the latter also able to give critical information needed to understand the origin of the possible superconductive pairing. The Meissner effect signal in these papers was also extremely weak, implying that only a tiny fraction of the end products became superconducting, or that any superconducting pairs were constrained to very short length scales. In this chapter, we present a photoemission study on pristine *p*-terphenyl single crystals (Fig. 5.1c) with controlled in-situ potassium metal (K) evaporation in ultra-high vacuum, aiming to directly detect the presence of the Cooper pairs that are at the heart of all known superconductors.

5.2 Experimental Results

5.2.1 Experimental Setup

Single crystal samples of *p*-terphenyl were grown by the zone-refining method [65]. Their crystal structure was identified using X-ray diffraction [65]. Three crystals of similar size (around 0.2×0.5×0.5 mm) were used.

Fig. 5.2 shows a schematic of the experiment. The crystal surfaces were prepared through sublimation at <373 K for one hour in 1×10^{-9} Torr vacuum, which due to the high vapor pressure of *p*-terphenyl will sublimate off any dirty exterior layers. Photoemission measurements were

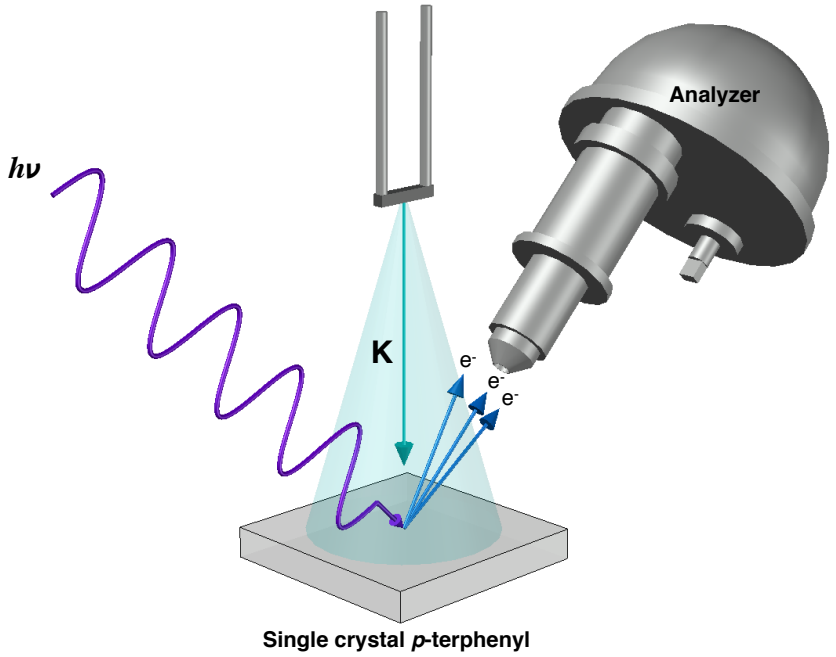

Figure 5.2: Schematics of experiment. The experimental schematic. K was repeatedly dosed onto the surfaces of the crystals, with photoemission spectra taken at these different doses.

carried out at the Stanford Synchrotron Radiation Lightsource (SSRL) beamline 5.4 with 32 eV linearly polarized light and 2×10^{-11} Torr ultra-high vacuum. The experimental energy resolution was 14 meV. Fermi energy references were repeatedly obtained from the in-situ Au Fermi edge installed on the same sample manipulator. In-situ potassium dosing was performed using a com-

mercial SAES getter source. It took the form of consecutive doses, with one dose corresponding to a heating current of 5.5 Amps that lasts 60 seconds. Sub monolayer coverages of K were then consecutively dosed onto the clean surface at T=300K, with the surfaces monitored by x-ray core level spectroscopy (XPS) as well as by high-resolution photoemission of the near-Fermi level features. To avoid sample charging, significant potassium dosing was performed at 300 K before cooling to low temperature.

5.2.2 Overview of Photoemission Intensity vs. Doping Level

Fig. 5.3 shows spectra for a variety of consecutive doses. There are at least 4 peaks in the spectra at binding energies (energy below E_F) near 5eV, 7eV, 9eV and 13.5eV respectively, corresponding to various peaks in the valence band/occupied molecular orbitals. For the pristine compound, there is vanishingly small spectral weight for the first 2eV below the chemical potential, consistent with the optical gaps that are of order 3-4eV [66]. With consecutive K surface dosings, a potassium $3p$ core level develops at the binding energy around 18eV, indicating that potassium is incorporated onto/into the surface. Even in the presence of K-dosing, the original valence peak features remain robust. This indicates that the potassium doping is perturbative in nature, only minimally modifying the large-scale electronic structure of p-terphenyl. On the other hand, the peak positions were monotonically shifted away from E_F, indicating a change in chemical potential and the spectral weight in the vicinity of the chemical potential grows (not visible in the wide scale scan of Fig. 5.3). This is consistent with the idea that potassium donates extra electrons to the lowest energy conduction bands.

To date, minimal angle-dependent changes have been observed, which is presumably due to A) the very weak dispersion expected in organic crystals in which the constituent components are far separated with weak orbital overlap, and/or B) possible disorder of the underlying crystal lattice or K overlayers, which were not annealed after the K deposition. For this reason, the present spectra are not labeled by momentum-space positions, and should be viewed as representing the average effect across the Brillouin zone.

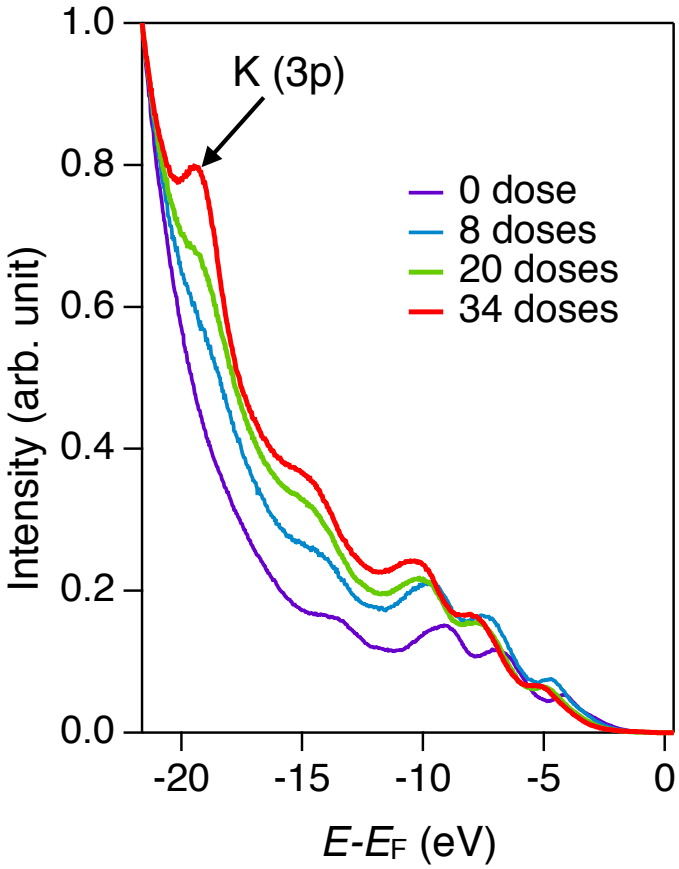

Figure 5.3: A wide overview of photoemission intensity vs. doping level. The growing intensity of the humps and peak around 18 eV (K 3p) in the photoemission spectra indicate the increasing doping level that follows the number of doses. The shift of the four spectral peaks of the valence band around 5, 7, 10, and 14eV shows the consistent change of chemical potential.

With sufficient K-dosing, very weak metallic spectral weight appeared near the chemical potential and the material became much more conductive, as also evidenced by the lack of sample charging at low temperatures (see Fig. 5.4). This weak spectral weight has similarities to some

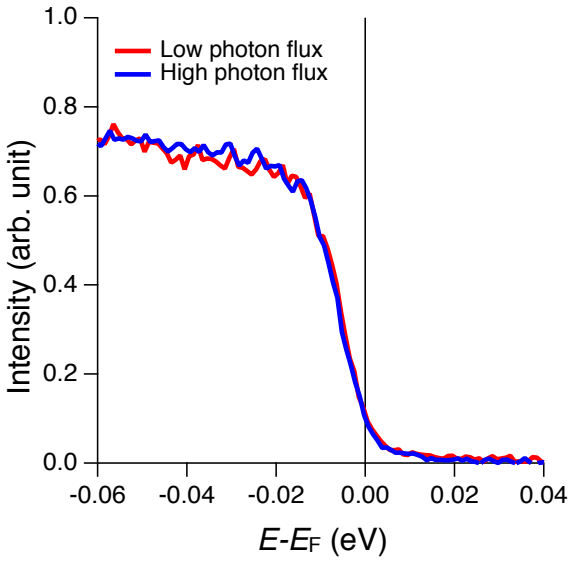

Figure 5.4: Photoemission spectra with different photon flux. The step edges of the two spectra with different photon flux are consistent. This indicates that there is no surface charging that could shift the spectral edge. The photon flux ratio is over 2

other doped aromatic organic compounds such as picene and coronene, in which minimal electronic weight was found at the Fermi level [67][68], and is different from doped C_{60} that does show strong spectral weight at E_F [69]. A more detailed discussion about the metallic but weak spectral weight at E_F is contained in Section 5.3.3.

5.2.3 Spectral Gaps with temperature dependence

Fig. 5.5a exemplified the spectral gap at T=10K for three different samples. The leading edge of all three 10K spectra are pulled away from the chemical potential, as also evidenced by an overlay of the spectrum from sample #3 with that from a metallic gold film measured under identical conditions right after the measurement of the doped *p*-terphenyl (see Fig. 5.6). An alternative view of the same spectra is presented in Fig. 5.5b, which shows the data of Fig. 5.5a

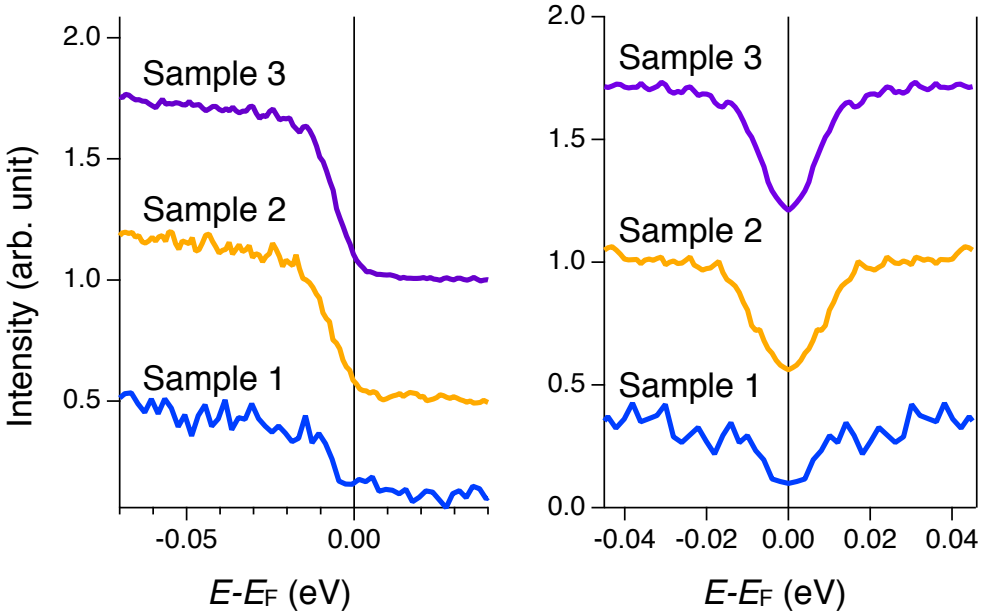

Figure 5.5: Spectral gap at 10K. Panel a, photoemission spectra of three different samples with effective surface doping of potassium. All spectra show a clear spectral edge below the Fermi level. Panel b, the corresponding symmetrized spectra that show the gap more clearly.

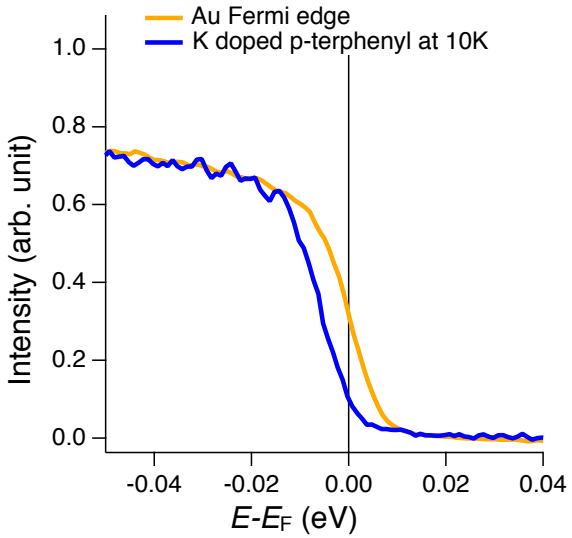

Figure 5.6: Comparing sample spectrum to Fermi level reference. The spectrum of the sample shows a leading edge well pushed away from that of the Au reference spectrum.

symmetrized about EF, which has been developed as a powerful way to remove the effect of the Fermi function and better visualize the presence of any low energy gaps [31]. While the statistics are different, the gap size of all three samples are similar to each other.

Fig. 5.7 panel a shows the very low energy regime for sample #3 as a function of temperature between 10K and 200K, whereas Fig. 5.7b shows the symmetrized spectra. Here we see that there is a strong suppression of low energy spectral weight (a gap or pseudogap) that gradually disappears as the temperature is raised. Fig. 5.7c shows the spectral weight lost at E_F (integrated over ± 3 meV) that is removed by the low energy gap, normalized to a maximum effect of 1 at our lowest temperature. It is seen that the low energy spectral weight is fully recovered at a temperature near 120K, above which there are minimal changes. This temperature is within error the same as the observed onset of the weak Meissner effect in ref [8], raising the possibility that the gaps we observe are related to the Meissner effect, that is, to the formation of Cooper pairs.

Other possible origins for the observed gaps or pseudogaps, such as due to a charge density wave (CDW), spin density wave (SDW), Coulomb gap, or polaronic effects are less plausible than that of a pairing gap, because a) no evidence for a CDW or SDW so far exists in these compounds, b) a Coulomb gap or polaronic gap would usually have a much softer or slowly varying character as a function of energy, c) none of the others would be expected to have the temperature dependence shown in Fig. 5.7c, while a pairing gap would, especially considering the onset temperature of the Meissner effect. Such a temperature evolution of the spectral weight lost was shown as a signature behavior in the pairing gap of cuprate high T_C superconductors (see Fig. 3 in ref. [58]). A more detailed discussion of the origin of the spectral gap is contained in Section 5.3.1.

Regardless of this, it is noted that the Meissner effect remains weak and that no clear evidence for zero electrical resistance has yet been reported. Possible reasons for this will be discussed near the end of the paper.

The gap data of Fig. 5.7b clearly shows the gap filling behavior with temperature, similar to the cuprate high temperature superconductors (see discussion in Section 5.3.2 and in ref. [70][59][71]. Such a filling-in behavior as well as weak or absent coherence peaks at the gap edge

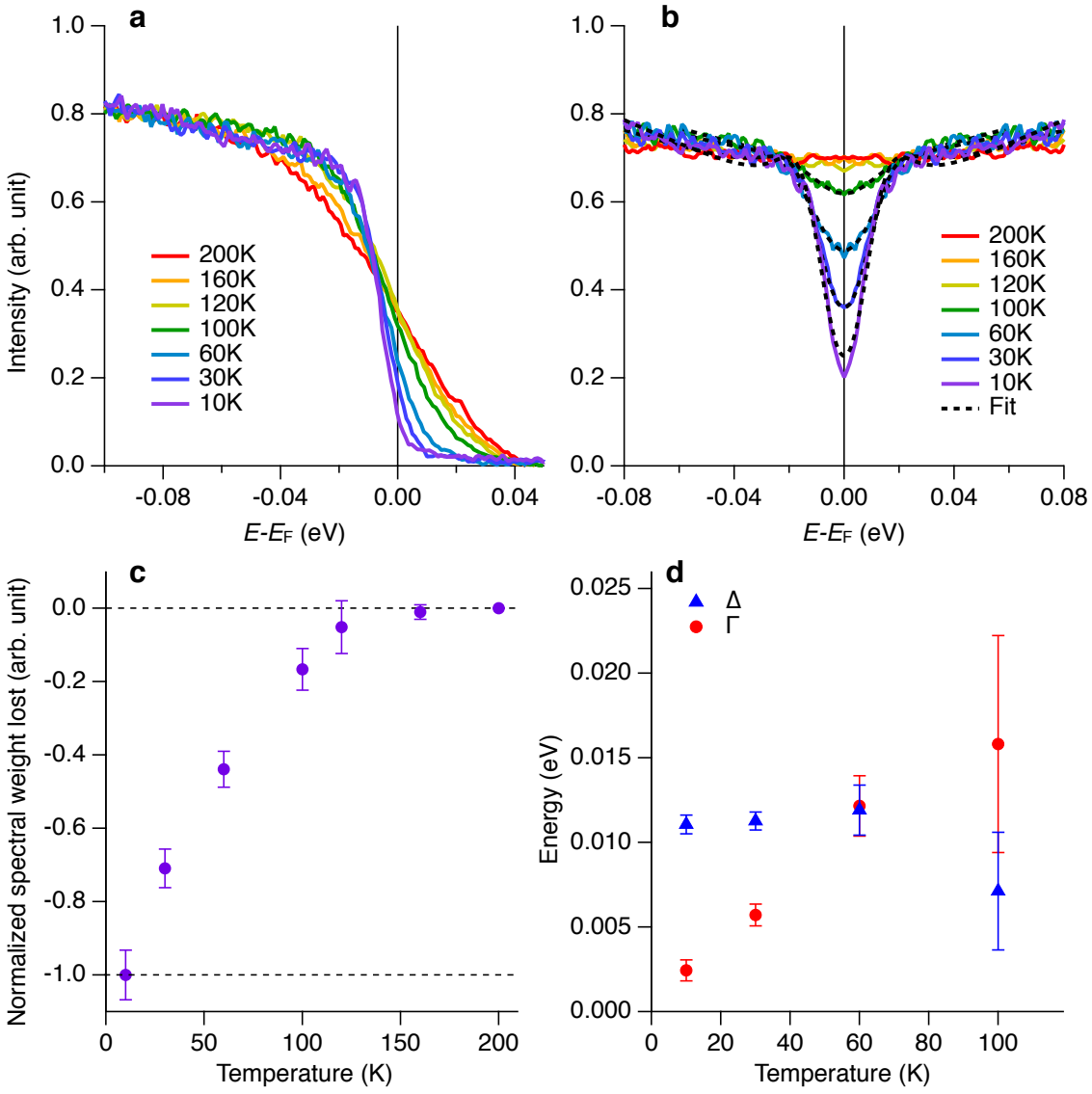

Figure 5.7: Temperature dependent spectral gaps. Panel a, temperature dependence of the very low energy photoemission spectra. Panel b, the spectra of panel a symmetrized about E_F so as to remove the effect of the Fermi function. This data clearly shows the presence of a gap at low temperatures, with the gap filling in as the temperature is increased. The dashed lines are fits to the data using equation 1, which has two key parameters a gap and a scattering rate Γ. Panel c, integrated spectral weight lost ($E_F \pm 3$meV) in the gap region vs. temperature, normalized to the lowest temperature measurement. The error bars denote thestandard deviations of the spectral weight lost extracted using different energy ranges for normalizing the spectra. d, The gap Δ and scattering rate Γ as a function of temperature from the fits of panel b. The error bar denotes the 3σ returned from the fitting.

is most commonly and simply modeled with the Dynes model for the superconducting density of states $N_{SC}(E,T)$ [72]:

$$N_{SC}(E,T = N_N(E)Re(\frac{E - i\Gamma(T)}{\sqrt{(E - i\Gamma(T))^2 - \Delta(T)^2}}) \tag{5.1}$$

where $N_N(E)$ is the normal state density of states and $\Gamma(T)$ represents a scattering rate or pair-breaking effect that competes with the superconducting gap $\Delta(T)$. The dotted lines in Fig. 5.7b show fits to the experimental data using this equation convolved with the measured experimental resolution function, and with $N_N(E) = a + bE$, i.e. a linearly varying density of states. The parameters extracted from these fits are shown in Fig. 5.7d. The gap has a low temperature magnitude of $\Delta(0) \sim 12$meV and is roughly constant as the temperature is increased to 60K or above. The fits also show that Γ which breaks the pairs, starts small and rises rapidly with temperature, which is unexpected for a conventional BCS superconductor but is a well-known characteristic for cuprate high temperature superconductors (see discussion in Section 5.3.2 and in refs. [59][70][71]). With considered as a pairing gap, our fits show that Γ becomes larger than Δ at approximately 60K. Above this temperature the rate at which pairs are broken will be faster than the rate at which they are created, so we expect that the formation of long range phase coherence above 60K would be especially difficult. Our results above 60K are therefore also strongly reminiscent of the pseudogap (pre-pairing) state in the cuprates, which are widely (but not universally) discussed as a state with preformed Cooper pairs that have not yet condensed into the phase-coherent SC state [59][58][70].

The possibility of sample aging was ruled out by a comparison of spectral weight through before and after the thermal cycles. Fig. 5.8 demonstrate the reproducibility before and after a temperature sweep from 10 K to 200 K, from sample 3. No sign of sample aging was found.

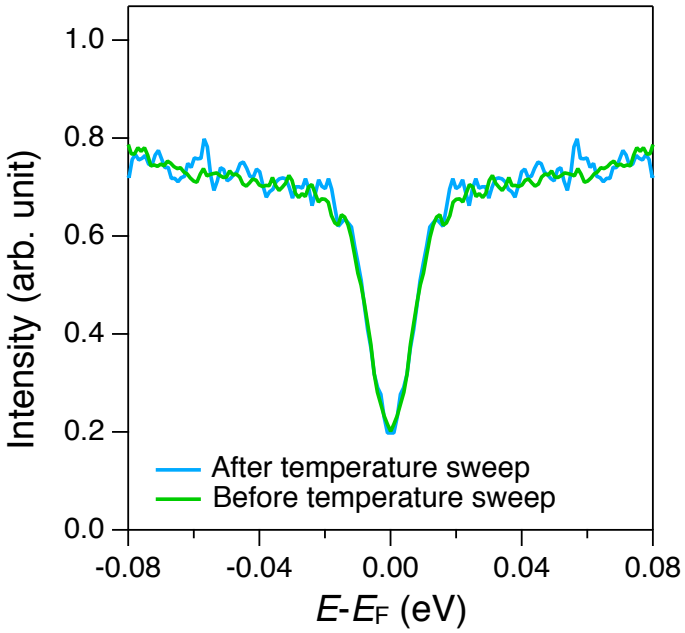

Figure 5.8: The two spectra of the sample show minimal changes before and after the temperature dependent measurement shown in Fig. 5.7

5.3 Discussion

5.3.1 The Origin of the Spectral Gap

As a spectroscopic probe, ARPES in general can map the characteristics of a gap well but cannot directly probe superconductivity itself. In this section, we give a more detailed discussion about why the pairing gap shows the best match to the phenomenology that we observed.

In general, if the gap we observe is due to a CDW (or SDW, Coulomb, polaronic effect), the existence of the weak Meissner effect would be an unusual coincidence, since a CDW (or SDW, Coulomb, polaronic effect) would have no direct connection to any Meissner effect. On the other hand, the presence of the weak Meissner effect with a similar temperature scale points towards the gap being related to pairing (but not necessarily long-range superconductivity). More importantly, the evolution of the in-gap spectral weight lost shown in Fig. 5.7c strongly resembles the one found in the pairing gap of cuprate high T_C superconductor, where it was demonstrated to be a signature of the paring-gap phase (see Fig. 3 in ref. [58]). In addition, in Fig. 5.7d and Fig. 5.9d, the fit parameters from the Dynes formula reveal a relatively small scattering rate (Γ) that is $\sim$2meV for the low temperature (10K) spectral weight. This value resembles the one from cuprates well below T_C using the same Dynes formula, which accounts for the strong depletion of spectral weight inside the gap (shown in Fig. 5.9, also discussed in previous studies from both ARPES [70] and STM [52]). In contrast, the pseudogap (possibly from CDW [[73]], though the origin is still controversial) that is observed well above T_C in the cuprates has a scattering rate that is typically a few tens of meV [70][52], strongly filling the spectral gap (there is only a weak depletion of in-gap spectral weight). This indicates a clear distinction from the pairing gap well below T_C. On the other hand, a recent STM [74] work on K surface doped single layer p-terphenyl reveals a similar spectral gap that is symmetric above and below E_F (a key feature of pairing gaps), and it showed no sign of a phase transition by charge ordering under varying temperature. In addition, spin density wave gaps found in iron-based superconductors also show a weak depletion in the spectrum that can be well distinguished from the low-energy pairing gap [75].

Moreover, our low-energy spectral gap is unlikely to be a Coulomb gap, which is a soft gap that usually develops over a large energy scale like 100meV or more [76][77]. A bipolaron at ∼180meV has been proposed in the K doped terphenyl [8] from Raman spectroscopy. Again, this energy scale is way larger than our low-energy spectral gap. Based on the discussion above, we can conclude that the spectral gap that we found in the K doped terphenyl can to a high probability be accounted as a pairing gap instead of other origins.

5.3.2 Comparison to High T_C Cuprate Superconductor

Fig. 5.9 demonstrate the phenomenological similarities between the cuprate superconductors and the *p*-terphenyl system. In particular, we stress that a lack of an apparent coherence peak is an intrinsic feature of the integrated spectral weight over momentum. As shown by the example of Fig. 5.9b, the integrated spectral weight often resembles a shifted Fermi edge even though the EDC at k_F (Energy Distribution Curve) shows a clear coherence peak. This can be understood as the EDC technique when measured at $k = k_F$ picks the sharpest feature of a whole spectrum. On the other hand, due to the lower statistics and the lack of a clear dispersion we cannot yet perform the same analysis on *p*-terphenyl. It is possible that with improved understanding of sample fabrication / doping / annealing it might be achieved in the future.

5.3.3 The Weak Spectral Weight at E_F in the Doped Compounds over a Larger Energy Scale

With sufficient K-dosing, weak metallic spectral weight appeared near the chemical potential and the material became much more conductive. Compared to the spectral weight of the HOMO (Highest Occupied Molecular Orbital), the weight of these new doped features is 100 times smaller (Fig. 5.10), i.e. we should not think of them as having rigidly doped the system into the LUMO (Lowest Unoccupied Molecular Orbital). This result has similarities to some other doped organic compounds such as picene and coronene, in which minimal electronic weight was found at the Fermi level [67][68], and is different from doped C_{60} that does show strong spectral weight at E_F [69].

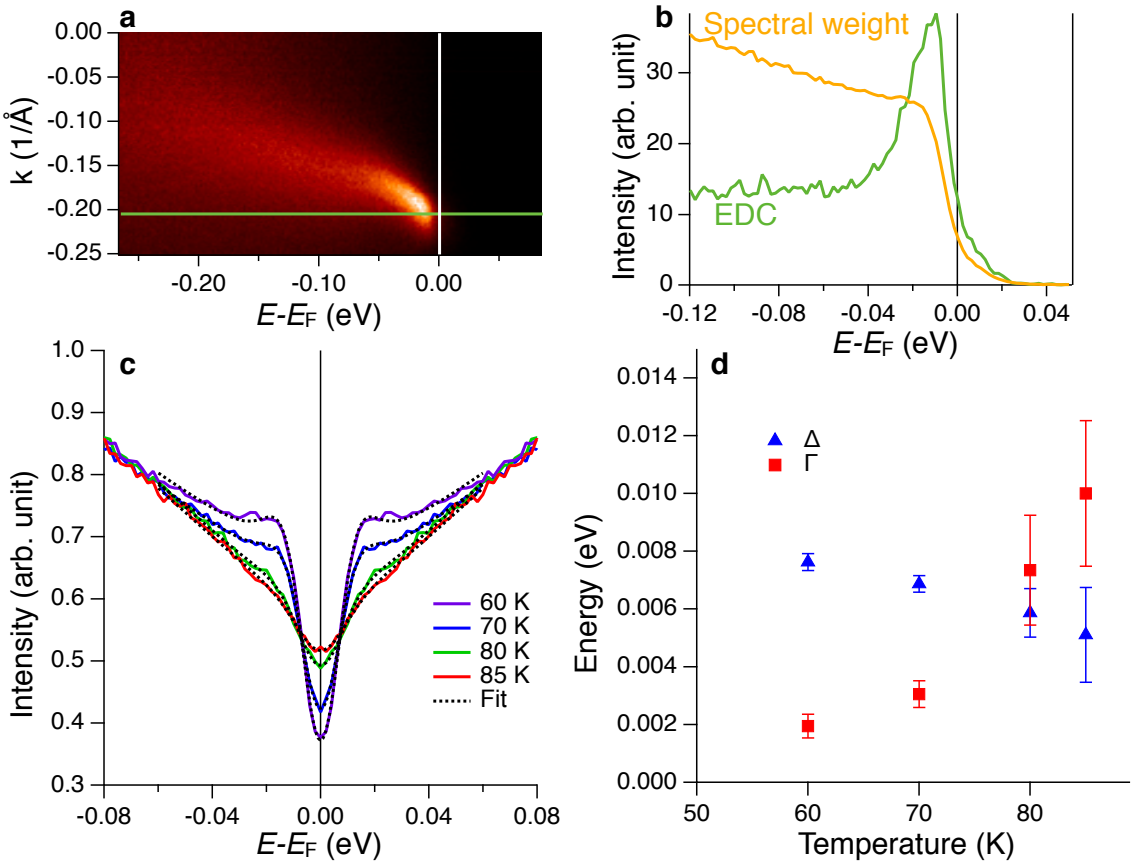

Figure 5.9: Comparing to high Tc cuprate superconductor. Panel a, a typical ARPES spectrum of BSCCO superconductor taken at 60K (T_C=85K, lightly underdoped) in the near nodal region. Panel b, the spectral weight (integrated over the momentum range of this cut) and an Energy Distribution Curve (EDC) at $k = k_F$ (green line in panel a). The EDC shows a strong coherence peak, but not in the spectral weight. c, The symmetrized spectral weight at different temperatures and the corresponding fits to equation 5.1 of the main text. Panel d, the extracted superconducting gaps (Δ) and scattering rates (Γ), which have a temperature dependence similar to that of Fig. 5.7c.

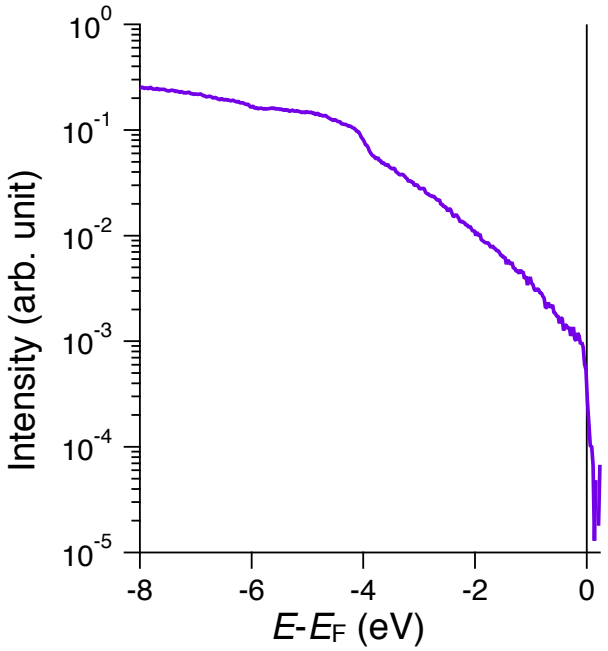

Figure 5.10: Log scale plot of the spectrum over large energy range after effective surface doping with potassium. The spectral peak around 5eV (also shown in Fig. 5.3) is approximately 100 times larger than the spectral weight near E_F

In contrast to the depression of spectral weight over the first 12 meV or so that is discussed in detail in the main paper, this depletion of spectral weight covers a few hundred meV scale or more. A large energy scale reduction in spectral weight at EF is often termed a pseudogap, and may have relation to the large energy pseudogaps observed in cuprates [78][79][80], manganites [81], iridates [82], as well as the other organics (we note that some relatively low energy reductions of spectral weight, such as in underdoped cuprates, are also termed a pseudogap). Mechanisms to discuss such physics include strong electronic correlations (Mott physics) [83], polaronic effects [84], Coulomb gap effects [77], and doping heterogeneity [85], though it is too early to determine which, if any, of these is responsible for the very low near-EF spectral weight we observe in terphenyl. Note that these large energy pseudogaps may or may not be related to lower energy scale (10-50 meV) pseudogaps observed in some cuprates [86] and iridates [87], which have recently been discussed in terms of charge density waves [88] as well as of preformed Cooper pairs in the absence of long range phase coherence [58][70].

On the other hand, we note that the extremely weak spectral weight near EF might be related to the extremely weak Meissner effect signal of the bulk material. It has been estimated from the Meissner signal strength that the superconducting fraction of the bulk material is less than 0.1% in volume, the ratio of which seems to strongly depends on the growth/annealing condition. If this is the case, then a typical K-doped system might be regarded as a mixture of a dominant non-superconducting background which is not drastically different from the parent compound, and K-dosing-induced tiny superconducting grains embedded inside, which could correspond to strong ARPES spectra in the valence bands but very weak density of states near E_F respectively. Such a scenario would also imply that a global zero resistivity state would be extremely difficult to achieve without significant improvement on the less than 0.1% level of volume ratio even with the presence of local pairing.

Beside the extremely inhomogeneous scenario as discussed above, there are other alternative scenarios that might address the unusually weak Meissner effect signal. The molecules in an organic solid are relatively far apart and not necessarily arrange for optimal wavefunction overlap, so

coherent transport between molecules is in general difficult. Upon doping, a possible scenario is that the pairing emerges, but pairs are localized inside individual molecules, and have very little overlap with each other. As the pair size can be smaller than the separation between pairs, the system may be best described as in the BEC limit where the system remains a Bosonic insulator, and cannot efficiently shield the magnetic field nor provide strong near EF spectral weight. It is only with enhanced overlapping between wavefunctions that a crossover to the BCS limit might become possible. An example of such a scenario is proposed in reference [89], in which K-dosing drives a structural transition and enhances the overlap of -orbitals, although it remains unclear how strong the overlap can be.

It is unclear whether the weak Meissner effect / weak spectral weight is dictated by the intrinsic physics of the system, or simply due to imperfection in the chemistry processes (to draw a parallel, early cuprate compounds only had 10% volume ratio [90]). The answer to this question is likely beyond the scope of a single experimental probe, and will require the combined efforts of the community.

5.3.4 Comparison to the STM Study

Ren *et al.* [74] have presented a STM study on surface doping a single layer p-terphenyl deposited on a Au (111) surface. Compared with our study, the STM work gave a very similar gap size of 10-14 meV. As STM naturally probes both the occupied side and the un-occupied side, the data shows that the spectral gap is symmetric above and below E_F. Such symmetry is a key feature of the pairing gap. Their tomographic data also found no sign of a CDW transition under varying temperature.

On the other hand, the STM study found no signature of vortices in the presence of a magnetic field, and they found the gap to be insensitive to a magnetic field up to 11 Tesla. Both of these are at odds with the conventional wisdom of a superconductor. Nevertheless, such a behavior does not rule out a local pairing gap that precedes the superconducting state before the phase stiffness enables superconductivity. For instance, in the example of the Nernst effect in cuprate

superconductors [91], it was believed that the pre-pairing gap does enable vortex-antivortex pairs. However, the vortices fluctuate at so fast a time scale that they cannot be detected by a static probe such as STM. In such a scenario, one might even argue that 11 T is in fact a very small field compared to this scale of pairing temperature (the typical conversion is that 1T$\sim$1K), and that the cuprates with similar temperature scales have critical fields over 100T. In fact, the author of ref [74] did discuss the local pairing gap as the most likely candidate for the origin.

We also note that there are certain differences between our own experiment that was carried out on a three dimanesional single crystal, and the STM study which was performed on a single layer *p*-terphenyl. To enable global superfluidity, generally the wavefunctions of preformed pairs need to overlap with each other, the process of which might well depend on the details of the structure and dimensionality. For instance, it was proposed that K-doping drives a 3D structural transition in the terphenyl crystal [89], which enhances the overlap between molecular orbitals and enables superconductivity. Such a transition is likely forbidden in a 2D case. It is also unclear whether the interface physics between the *p*-terphenyl and the Au substrate plays a role here.

5.4 Conclusion

The success of the simple Dynes model fitting, as well as the general resemblance of our observed phenomenology to that of cuprate superconductors, enhances the likelihood of high temperature superconductivity in this class of materials, and indicates that the host of the superconductivity should be the K-doped or K-intercalated *p*-terphenyl itself. In contrast to the original report [8][92] in which the end product is arguably a mixture of different components, in our experiment it is highly unlikely that chemical reactions substantially modified the material phase.

The mechanism of the likely pairing in these materials is also potentially quite different from other known superconductors, not just because of the high T_Cs but also because of the unusual structure and chemistry of organic molecular solids. Littles original proposal suggested that a fully electronic (non-phononic) mechanism may be possible [7] and other proposals for organic superconductors including Resonating Valence Bond (RVB) physics [93] as well as bipolaronic

pairing mechanisms [94] have been discussed in the context of organic superconductivity. However, since the proposed bipolaron energy scale from Raman spectroscopy is of the order of 180 meV in these materials [8], it is not obvious if we can connect bipolaron physics to the much lower energy scale gaps that are observes here. The present findings therefore potentially open new and exciting venues into the most fundamental aspects of superconductivity as well.

Chapter 6

Fermiology and Electron Dynamics of Trilayer Nickelate $La_4Ni_3O_{10}$

Layered nickelates have the potential for exotic physics similar to high T_C superconducting cuprates as they have similar crystal structures and these transition metals are neighbors in the periodic table. In this chapter, we present an ARPES study of the trilayer nickelate $La_4Ni_3O_{10}$ revealing its electronic structure and correlations, finding strong resemblances to the cuprates as well as a few key differences. We find a large hole Fermi surface that closely resembles the Fermi surface of optimally hole-doped cuprates, including its $d_{x^2-y^2}$ orbital character, hole filling level, and strength of electronic correlations. However, in contrast to cuprates, $La_4Ni_3O_{10}$ has no pseudogap in the $d_{x^2-y^2}$ band, while it has an extra band of principally $d_{3z^2-r^2}$ orbital character, which presents a low temperature energy gap. These aspects drive the nickelate physics, with the differences from the cuprate electronic structure potentially shedding light on the origin of superconductivity in the cuprates.

6.1 Introduction

Transition metal oxides hold a variety of intriguing electronic phases arising from the strongly correlated d electrons. Among these materials, the cuprates have attracted most of the attention, exhibiting compelling physics including the high T_C superconducting phase, the strange metal scattering rates, pseudogap state, etc [15]. To understand these exotic properties, close analogues of the cuprates have been studied extensively to gain insight into which aspects of cuprate physics are most critical for the superconductivity and other anomalous properties. Layered perovskite nick-

elates are perhaps the most natural place to look for this physics, as nickel lies directly adjacent to copper in the periodic table, meaning they should also be charge-transfer/Mott insulators [95] and nickelates can be formed in the same or similar crystal structures as the cuprates [96]. Indeed, some of these materials have been shown to harbor pseudogaps [97] as well as stripe and checkerboard type charge ordering [98][99], and recent theoretical works have argued that high temperature superconductivity should likely also present itself [100]. This has motivated recent investigations of $LaNiO_3$ based heterostructures and planar-trilayer nickelates that have been designed to imitate the electronic configuration of cuprates in pursuit of potential high T_C superconductivity and other intriguing cuprate-related phenomena [96][101][102][103][104]. Unlike the single layer nickelate compounds, where a metallic state is difficult to obtain, or non-layered structures (such as $LaNiO_3$) which are not superconducting even in the cuprates, trilayer Ruddlesden-Popper nickelates $R_4Ni_3O_10$ (R=La, Pr), with formal oxidation state 2.67+ (d^7.33), are good metallic materials of correlated electrons that are natural for detailed study. However, such studies have not been possible until now because of the difficulty of preparing high quality single crystal samples. This has recently been overcome for trilayer nickelates through the use of special high-pressure floating-zone image furnaces, which now enable single crystals of these nickelates to be prepared [103]. In the planar trilayer nickelate $La_4Ni_3O_8$, recent studies [103][105] have revealed stripe charge ordering with a phase transition at 105 K. As for $La_4Ni_3O_{10}$, a charge density wave instability has been predicted below the metal-to-metal transition around 140 K [106][107]. In this chapter, we present the electronic structure and dynamics of trilayer $La_4Ni_3O_{10}$ using angle-resolved photoemission spectroscopy (ARPES) and compare our observations on $La_4Ni_3O_{10}$ to cuprates and to Density Functional Theory (DFT) band structure calculations. Our ARPES measurements reveal a gapless hole pocket that resembles the hole Fermi surface of cuprates. Comparing our data to the DFT calculation, most parts of the $La_4Ni_3O_{10}$ Fermi surface present a mass enhancement of 2 to 2.5, which is very similar to what is observed in cuprates in the normal state. On the other hand, an extra hole pocket with strong $d_{3z^2-r^2}$ orbital character exhibits a flat band dispersion near the Fermi level, revealing a 20 meV energy gap that shows a connection to the transition found in the

resistivity curve. Our study on $La_4Ni_3O_{10}$ will help resolve the anomalous physics of the nickelates (such as the resistivity curve and any potential ordering tendencies associated with it), while also revealing the connection to the cuprate physics. This therefore provides insight into the potential testing ground for cuprate-like properties, as well as articulating the electronic structure of this novel nickel-based oxide.

6.2 ARPES Results of $La_4Ni_3O_{10}$

The ARPES experiments were carried out at the Advanced Light Source using beamlines 4.0.3, 10.0.1 and 7.0.2. The energy resolution was 13 meV at beamline 7.0.2 and 20 meV at beamline 4.0.3. All data shown in this chapter were measured with the photon energy of 75 eV unless otherwise noted. All Fermi surface maps shown in this chapter are integrated intensity over EF $\pm$5meV. The polarization dependent study (section 6.2.2) was carried out at beamline 10.0.1 with glancing incident photons.

6.2.1 Electronic Structure of $La_4Ni_3O_{10}$

The crystal structure of the Ni-O plane in $La_4Ni_3O_{10}$ is depicted in Fig. 6.1 panel e. Due to the out-of-plane tilted Ni-O octahedra, the original Ni-O plaquette (blue box) is reconstructed into a two Ni unit cell (black box) with double the volume, which is similar to the reconstruction of the antiferromagnetic unit cell in the cuprates. Panels a and b of Fig. 6.1 show the Fermi surface of $La_4Ni_3O_{10}$ taken at 30 K and the corresponding schematic drawing. The original Brillouin zone that corresponds to the Ni-O plaquette is marked as the blue box, while the black box corresponds to the folded Brillouin zone of $La_4Ni_3O_{10}$. Different parts of the Fermi surface are highlighted with different colors and marked as α, α', β and γ in Fig. 6.1b. In resemblance to the cuprate ($(Bi,Pb)_2Sr_2CaCu_2O_{8+\delta}$) Fermi surface antibonding band shown in Fig. 6.1 panel c and d, $La_4Ni_3O_{10}$ also displays a large hole pocket centered at the corner of the original Brillouin zone (α band). Due to the doubling of the unit cell, this cuprate-like hole pocket (α band) is (π,π) back-folded, with the back-folded bands drawn as dashed curves (α' band) in Fig. 6.1b. This back-folded

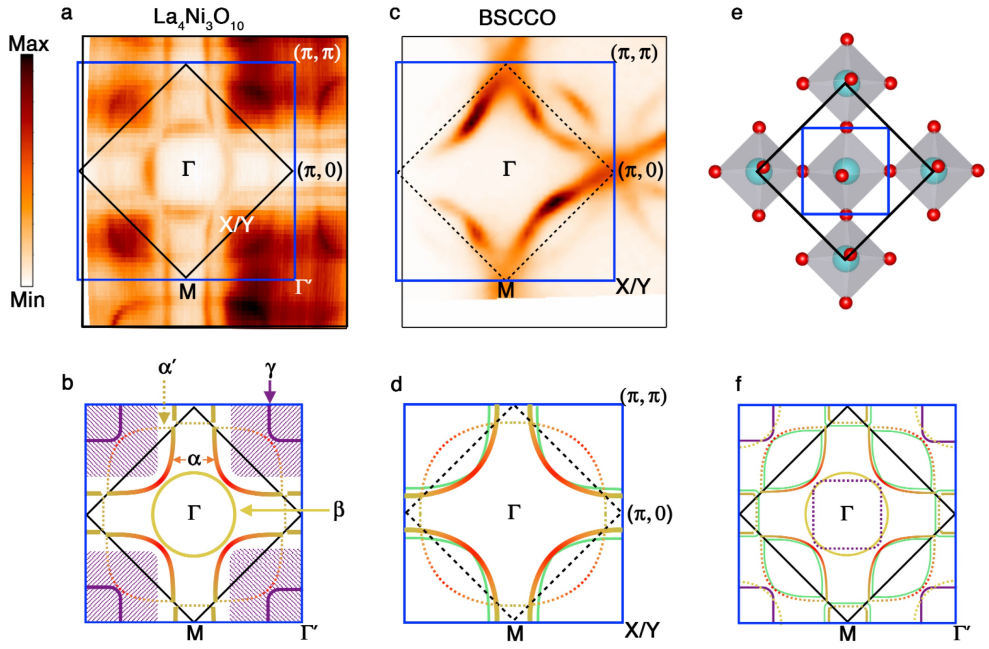

Figure 6.1: Fermi surface map of $La_4Ni_3O_{10}$. Panel a and b, the unsymmetrized Fermi surface of $La_4Ni_3O_{10}$ from ARPES measurement and schematic of the Fermi surface. Panel c and d, Fermi surface of optimally doped cuprate $(Bi,Pb)_2Sr_2CaCu_2O_{8+\delta}$ (BSCCO) and a schematic of its Fermi surface. The Fermi surface of $La_4Ni_3O_{10}$ can be divided into three parts. The hole pocket centered at Γ' is similar to the hole doped cuprate Fermi surface (solid red-yellow curve) with the (π,π) back-folded band. This cuprate-like hole pocket corresponds to 17% of hole filling level. The other two parts are the extra electron (yellow circle in b) and hole (purple curve and hatched area) pocket around Γ and Γ', respectively. Panel e, the real space unit cells of $La_4Ni_3O_{10}$. The black box corresponds to the two Ni unit cells where the blue box corresponds to the origin Ni-O plaquette. Panel f, drawing of the Fermi surface in the repeated zone representation where pockets are back folded into the small Brillouin zone. The light green curves in panels d and f represent the extra band expected from multilayer band splitting.

feature resembles the shadow band observed in the cuprate Fermi surface [108][109][110][111]. In Fig. 6.1f, we sketch the reconstructed Fermi surface with all the back-folded bands shown as thin dotted curves. However, the measurement only reveals the β pocket (yellow circle) at the original Brillouin zone center while the γ pocket (purple) is only present at the original Brillouin zone corner. This absence of a strong back-folded band feature from the broken translation symmetry of the crystal has been observed in many other materials and investigated in previous studies [112][113][114]. When the folding potential from the broken translation symmetry is weak, the spectral intensity of the back-folded bands is also expected to be extremely weak, and sometimes further reduced for symmetry reasons [114]—therefore, it is not surprising that these back-folded bands are not observed. In this chapter, we will show from both polarization-selective ARPES experiments and DFT calculations that the orbital character of the cuprate-like hole pockets possess a strong $d_{x^2-y^2}$ weighting (similar to cuprates) while the other parts of the Fermi surface (not present in cuprates) display a $d_{3z^2-r^2}$ dominant orbital character. Details of the polarization dependent ARPES experiment and orbital characters are discussed later in section 6.2.2 and Fig. 6.4. Counting the size of the cuprate-like hole pocket in Fig. 6.1a, it occupies ~58.5% of the original Brillouin zone. With the scheme of $1 + p$ holes per nickel per degenerate spin direction, this indicates the hole doping level corresponding to this part of the Fermi surface is ~17%, similar to the optimally hole-doped cuprates. The γ pocket with a $d_{3z^2-r^2}$ orbital character centered around the zone corner shows a blurry outline with the spectral weight covering a large volume of the Brillouin zone, which is depicted as the hatched area in the schematic drawing (Fig. 6.1b). This blurry spectral weight exhibits a stark contrast to other parts of the Fermi surface. As we will show later, this blurry spectral weight is due to a flat band lying extremely close to the Fermi energy over a large region of k-space.

In Fig. 6.2, we present additional aspects of the electronic structure utilizing two different experimental geometries, taking advantage of the photon polarization/matrix element effects to highlight various features of the data, particularly the $d_{x^2-y^2}$ and $d_{3z^2-r^2}$ bands (see section 6.2.2). In cuts 1 and 2 (Fig. 6.2 c-d), which are the high symmetry cuts through the Fermi surface shown

in Fig. 6.2 a, we observe a sharp band dispersion near the M point corresponding to the cuprate-like hole pocket near the boundary of the unfolded Brillouin zone. This region in momentum space resembles the antinodal region in the hole doped cuprates, where the band structure comes to a saddle point at (π, 0) roughly around -100 meV, and hosts the largest energy gap in both the superconducting and pseudogap phases. Just as in the cuprates, the band shown here for $La_4Ni_3O_{10}$ comes to a saddle point at (π, 0) near -100 meV, shown for both cuts 1 and 2 of Fig. 6.2. To quantify the dispersion, we have extracted peak positions from both Energy Distribution Curves (EDCs) and Momentum Distribution Curves (MDCs), with the extracted peak positions plotted as red and blue dots respectively, in each ARPES spectrum.

Other aspects of the electronic structure can be observed by a 45-degree azimuthal rotation of the sample relative to the incident direction of the photons (Fig. 6.2b), giving selection rules that highlight different symmetry states from those of Fig. 6.1b. In cut 3, a slice through the electron pocket (β band) displays a clear dispersion near the Fermi level. However, the ratio of coherent spectral weight to the background weight is not so strong for this band. In cut 4, around the Γ' point, a cut through the γ pocket with $d_{3z^2-r^2}$ orbital character displays a spectral weight that is broadened near the Fermi level. The dispersion of the γ band is flattened near the Fermi level indicating exotic low-energy electron dynamics. This band behaves quite differently from the α and β bands that are highly dispersive across the Fermi level.

We calculated the band structure using the all-electron, full-potential code WIEN2k [115] based on the augmented plane wave plus local orbital (APW+LO) basis set [116]. As exchange-correlation potential we have used the generalized gradient approximation (GGA) in the Perdew-Burke-Ernzerhof scheme [117]. The results of these calculations are plotted in Fig. 6.2g. The α, β, and γ bands are labeled in the plot, which correspond to the three different parts of the Fermi surface observed experimentally.

The color scale that indicates the orbital weighting shows a dominant $d_{x^2-y^2}$ orbital character for the cuprate-like hole pocket (α band), while the γ hole pocket reveals a dominant $d_{3z^2-r^2}$ orbital character. As for the β band, the DFT calculation exhibits a mixture of $d_{x^2-y^2}$ and $d_{3z^2-r^2}$ orbital

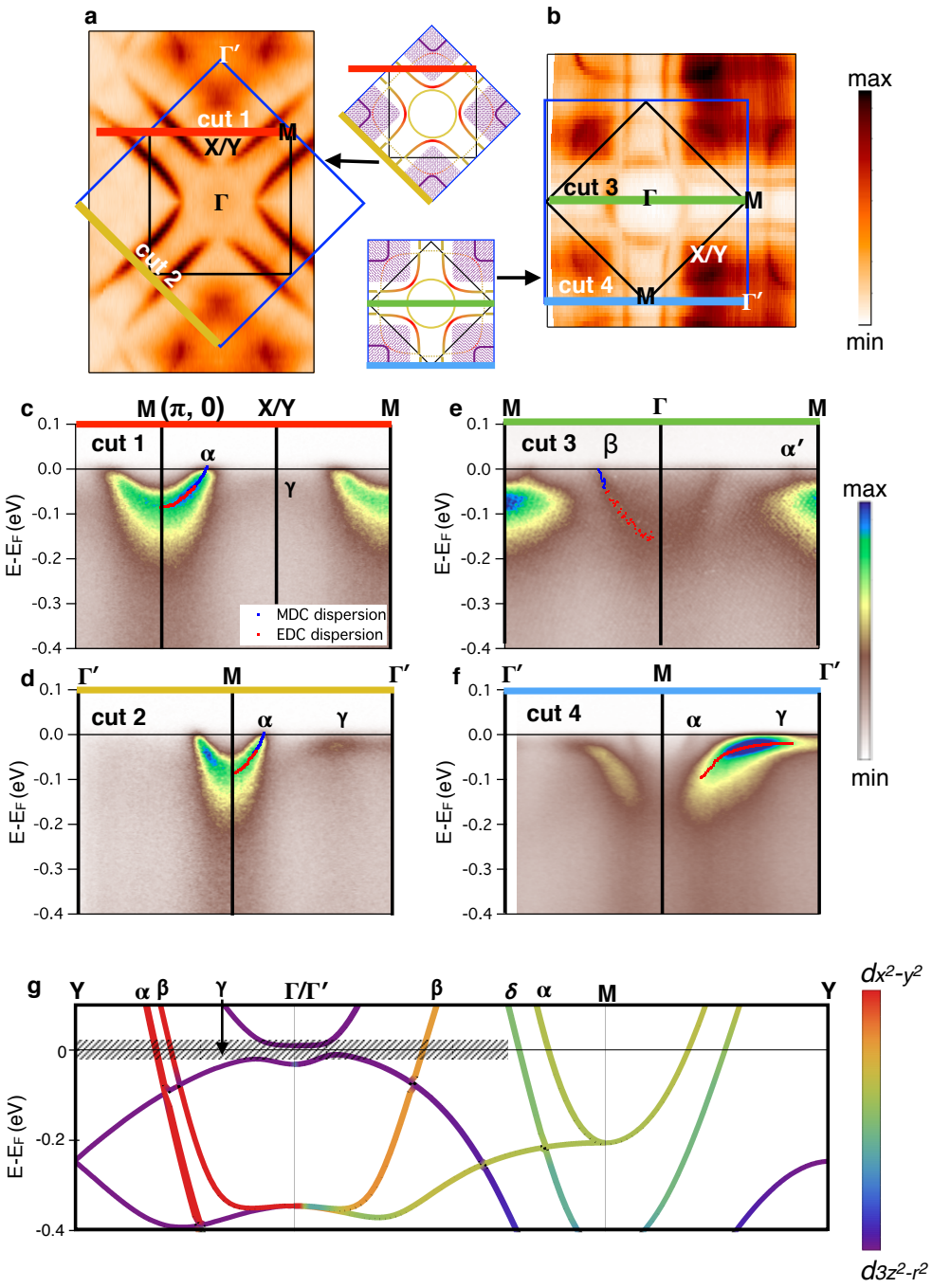

Figure 6.2: Fermi surface maps and high symmetry cuts of $La_4Ni_3O_{10}$ measured at low temperature (T=30K). Panel a and b, Fermi surface maps of $La_4Ni_3O_{10}$ taken with different experimental geometries, where map a emphasizes the cuprate-like hole pocket (α band), while map b shows the comprehensive structure. The blue and black boxes are the unfolded and folded Brillouin zones, respectively. Panel c-f ARPES spectra of the high symmetry cuts. Each high symmetry cut position is indicated as the colored line in panel a and b. Cut 4 is taken along Γ-M in the 2nd Brillouin zone to avoid the weak matrix element in the 1st Brillouin zone. The dots in panel c-f depict the MDCs (blue) and EDCs (red) peak position which indicate the band dispersion. Panel g, band structure from DFT calculation under the folded Brillouin zone. The weightings of $d_{3z^2-r^2}$ and $d_{x^2-y^2}$ orbital character are shown with different color scales. The hatched area indicates the blurry area from the γ band spectral weight in the Fermi surface.

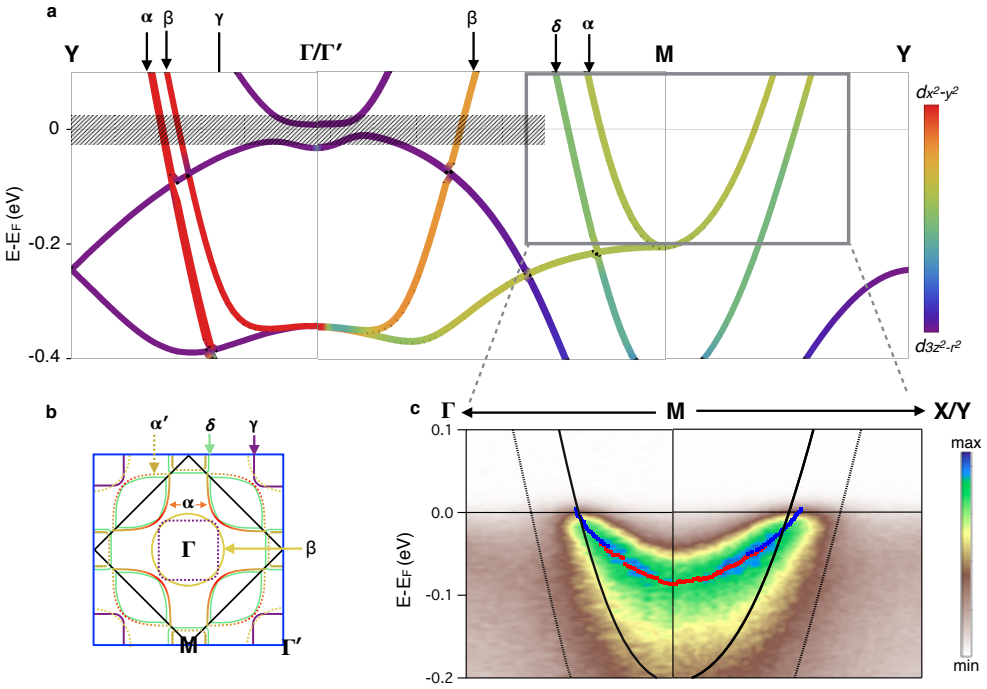

Figure 6.3: All bands from multilayer band splitting and hybridization. Panel a, band structure from DFT calculation under the folded Brillouin zone. The weightings of $d_{3z^2-r^2}$ and $d_{x^2-y^2}$ orbital character are shown by the color scale plot. The hatched area indicates the blurry area from the γ band spectral weight in the Fermi surface. Panel b, the schematic drawing of the measured Fermi surface. Different parts of the Fermi surface are marked as α, β, γ, and δ. Panel c, comparison of ARPES spectrum and the DFT band structure around the M point, where the dotted curves correspond to the outer nickel bands, the solid and dashed curves correspond to the inner nickel bands.

character. This theoretical result is consistent with our polarization-dependent ARPES result, which will be discussed later in section 6.2.2.

Along the Γ/Γ'-M direction, there is an extra green band (δ) that crosses the Fermi level that has not been experimentally resolved in our data. In the calculation, the δ band (green) and the α band (yellow) originate from the outer and inner Ni-O planes respectively. In the experimental data (Fig. 6.2d) only one band in this direction is resolved, whose Fermi momentum (k_F) coincides closely with the one from the inner Ni-O planes, i.e. the α band. In 6.3, the ARPES spectrum is overlaid with the theoretical band dispersion around the M point. The calculated outer nickel bands do not coincide with any band dispersion in the spectrum at k_F, whereas the inner nickel bands show a good match.

6.2.2 Polarization-Dependent ARPES Experiment and Orbital Characters

Polarization-dependent ARPES has been proved to be a powerful experimental tool to identify the orbital symmetry in electronic structure [118][119][120][121]. To understand the orbital characters in different parts of the Fermi surface in $La_4Ni_3O_{10}$, we performed polarization-dependent ARPES measurement on this material. A schematic drawing of the experimental geometry is sketched in Fig. 6.4a. In the first row of the figure (panels b, c) taken along the green cut of the schematic, one can observe a stark contrast between the s and p polarization. In the s polarization, the nodal-cut of the cuprate-like hole pocket (α band) shows a band with good contrast, while the same band disappears in the p polarization. The other hole pocket (γ band) shows an opposite behavior, where it disappears in the s polarization but exhibits high intensity in the p polarization. The electron pocket around Γ (yellow circle in Fig. 6.4a) is difficult to resolve in Fig. 6.4b,c as the spectral intensity is contaminated by the other two bands. In order to resolve the band dispersion of this electron pocket, we take a slightly different cut along the blue line in Fig. 6.4a, with the band dispersion sketched as the yellow curve in the spectra (β band, Fig. 6.4d, e), The contrast of this band with the two polarizations is not as sharp as the other band in Fig. 6.4, as it shows a roughly equal intensity in both polarizations.

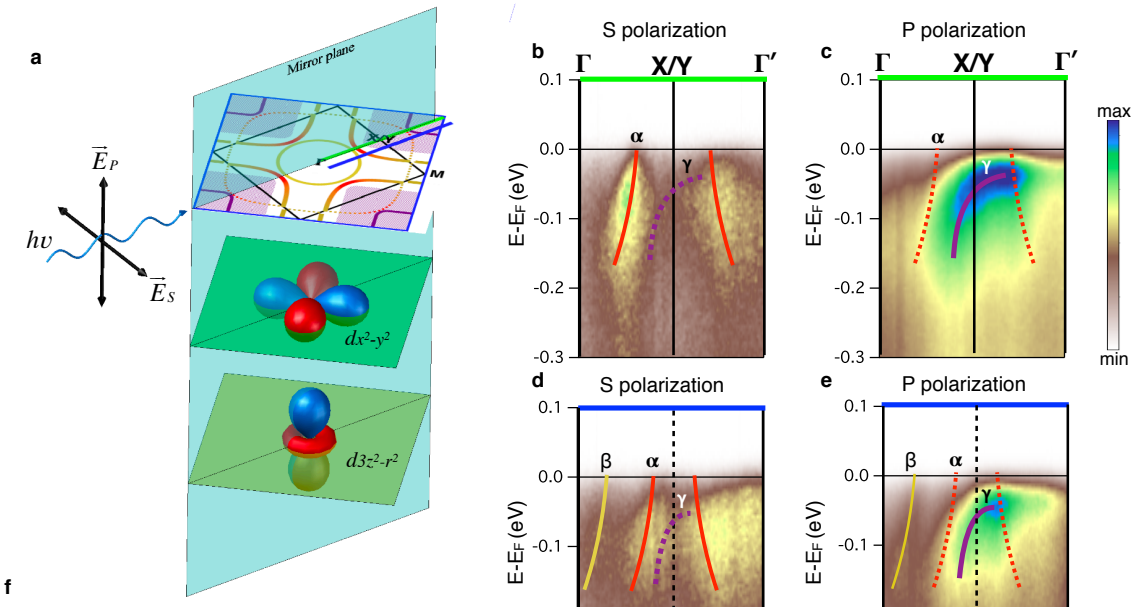

f

	s pol. (odd)	p pol. (even)
dx^2-y^2 (odd)	strong	weak
$d3z^2$-r^2 (even)	weak	strong

Figure 6.4: Polarization dependent ARPES measurement. Panel a, schematic drawing of the experimental geometry and the Fermi surface map for spectra in panel b and c. The green line indicates the cut positions of spectra in panel b and c. The blue line indicates the cut position of spectra in panel d and e. Panel b and c, spectra taken with s polarization light. Panel d and e, spectra taken with p polarized light. The color scale is the same for each row of spectra. The band dispersions in each spectrum are sketched with the colored curves corresponding to the different parts in the Fermiology. The dashed curve means disfavored matrix element, and solid curve means favored matrix element. Panel f, the table describes the parity of polarization vector and orbitals with respect to the mirror plane shown in panel a and the correspondent matrix element intensity.

The table in Fig. 6.4 panel f describes the parity of the polarization vectors and the orbitals with respect to the mirror plane. The matrix element for the in-plane $d_{x^2-y^2}$ orbital is strong in the s polarization but weak in the p polarization while the $d_{3z^2-r^2}$ orbital has an opposite trend. Thus, we can conclude that the cuprate-like hole pocket (α band, orange) exhibits a $d_{x^2-y^2}$ orbital character whereas the γ hole pocket around Γ' (purple) reveals a $d_{3z^2-r^2}$ orbital character and the β electron pocket around Γ point (yellow) shows a mixture of these two orbitals.

6.2.3 Search for Multilayer Band Splitting

To further investigate the possibility of multilayer band splitting, we explored the matrix element effect with different photon energies and polarizations near the M point (Fig. 6.5). Fig. 6.5b shows the stack of Momentum Distribution Curves (MDCs) at E_F at many different photon energies every eV from 50 eV to 90 eV. In this set of data, the M point and the k_F position of the α band are represented by the blue solid line and the dashed yellow line respectively, whereas the green dotted line shows the expected k_F position of the δ band from the outer Ni-O planes, as predicted by our DFT calculation. Though there are quite strong modulations of the ARPES intensity with photon energy, the two main peaks of the experimental MDCs match the expected k_F positions for the α band for every energy where a peak is resolvable. Further, there is never a clear peak along the green dotted lines where we expect the band to reside. This is consistent with all of the other data in the paper, though we also note that it is difficult to completely exhaust the potential matrix element effect in the experiment because of the huge potential parameter space.

We also consider the possibility that the outer Ni-O plane, which is expected to give rise to the δ band, might be affected by the surface potential in such a way as to move its k-position towards the α band or to greatly reduce its intensity. That the δ band should be more sensitive to the surface than the other bands is plausible since the outer Ni-O plane is closer to the cleaved surface, which is expected to be between the La-O planes (Fig. 6.5c).

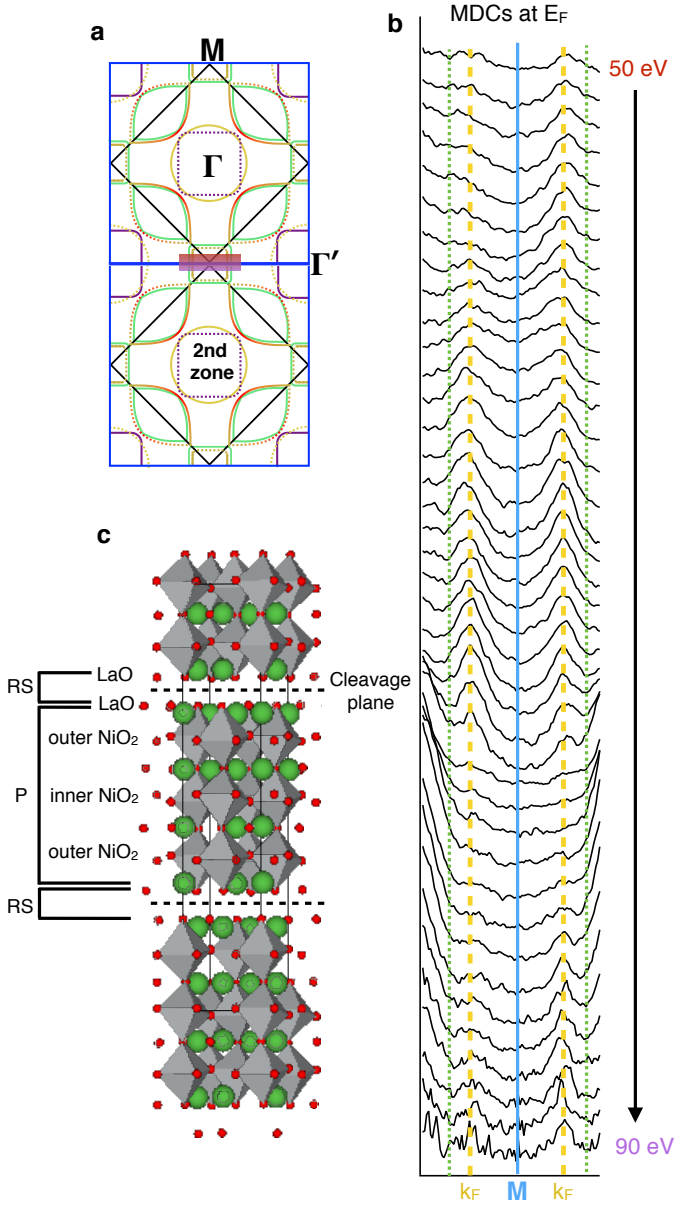

Figure 6.5: Photon energy dependent spectra for searching for the delta band. Panel a, schematic of the Brillouin zone including multilayer splitting. The red-purple shaded area indicates the area of the k_F MDC positions in panel b. Panel b, k_F MDCs of the cuts near the M point (similar to the antinodal region in cuprates.). The M point and the k_F position of the band are represented by the blue solid line and the dashed yellow line respectively, whereas the green dotted line shows the expected k_F position of the band from the outer Ni-O planes, as predicted by our DFT calculation. The δ band is not clearly resolved at any photon energy. Panel c, the crystal structure of La-trilayer nickelate: P, perovskite; RS, rock salt.

6.2.4 Band Renormalization and Mass Enhancement

The measured band dispersions from EDC and MDC analyses of the data of Fig. 6.2 are shown in Fig. 6.6a-c (open colored circles) and are compared to the results from our DFT calculation (black lines). It is seen that the measured dispersions are flatter than the calculated ones, implying a mass-renormalization (self-energy) effect. We extracted the mass enhancements from the ratio of the second derivatives of the measured to calculated dispersions, which further quantifies the band renormalization effect. The values of mass enhancements in panel d of Fig. 6.2 are around 2.2 for each of the bands, which are similar to results of cuprates in the normal state, which are also around 2 [39][41][38]. The dotted curves in Fig. 6.6a-c are the DFT bands scaled by the mass enhancement value, and show good agreement with the measured band dispersions. We do not show the γ band here due to an energy gap opening in this band - details will be discussed later.

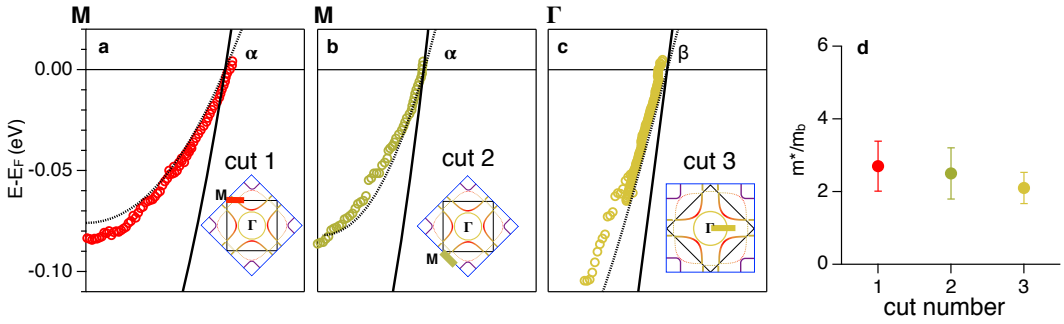

Figure 6.6: Low energy electron dynamics. Panel a-c, experimental band dispersions (colored dots), where the cut positions are indicated in the insets. The solid black curves are the calculated dispersions from DFT theory for the relevant bands. The dotted black curves are the DFT bands scaled by the corresponding mass enhancement values. Panel d, the measured mass enhancements of each band, which are all roughly 2 to 2.5. The error bars denotes the s.d. of the mass enhancement determined by using various ranges of the band dispersion.

6.2.5 Gapped and Non-Gapped Portions of the Fermi Surface

To further understand the low energy electron dynamics, we investigate the energy gap of two different bands. For the cuprate-like hole pocket, symmetrized energy distribution curves (EDCs) at multiple k_F points measured at 30K are plotted in Fig. 6.7a, with k-locations labeled in Fig.

6.7b. Using the standard method typically applied to cuprates [31], the single peaks at the Fermi level for each of the points indicate a state that is ungapped. Unlike the single layer nickelate, where a pseudogap is observed near the antinodal region [97], the cuprate-like band in this trilayer nickelate shows no energy gap opening. However, for the γ band with $d_{3z^2-r^2}$ orbital character, symmetrized spectra taken at 24K (Fig. 6.7 panel c) show a dip of spectral weight at the Fermi level and the band dispersion turns flat and extends to a wide range in momentum when approaching the Fermi level. These features reveal a significant energy gap of about 20 meV in this band. This is consistent with our observation in the low temperature Fermi surface, in which the hole pocket covers a blurry area where no well-defined Fermi momentum can be observed. However, in the 180 K spectrum (Fig. 6.7 panel d), the coherent spectral weight displays a linear band dispersion across the Fermi level. The symmetrized EDCs in Fig. 6.7 panel e describe more temperature dependent behavior of this electronic dynamics. When moving towards higher temperature, the spectral weight within the energy gap gradually increases and the coherence peaks of the spectra are broadened. The disappearance of the energy gap between 120K and 150K is consistent with the resistivity curve in Fig. 6.7f, which display the anomaly at 140 K. This indicates the likely connection of the energy gap opening to the phase transition found in the resistivity curve.

6.3 Discussion of the Electronic Structure and Dynamics

6.3.1 Resemblances to Cuprates

In general, the electronic structure and dynamics of $La_4Ni_3O_{10}$ present multiple commonalities to the high T_C superconductor cuprates. First, the Fermi surface of $La_4Ni_3O_{10}$ reveals a hole pocket with $d_{x^2-y^2}$ orbital character that is in many ways similar to the hole surface in cuprates. The volume of this hole part of the Fermi surface indicates a doping level of 17%, close to the optimal hole doping for superconductivity in cuprates. Second, the mass enhancement of $La_4Ni_3O_{10}$ shows a similar value to that of the normal state of the cuprates [38][39][41]. The similarity of this renormalization effect in $La_4Ni_3O_{10}$ and cuprates indicates a similarity of the electronic correlations

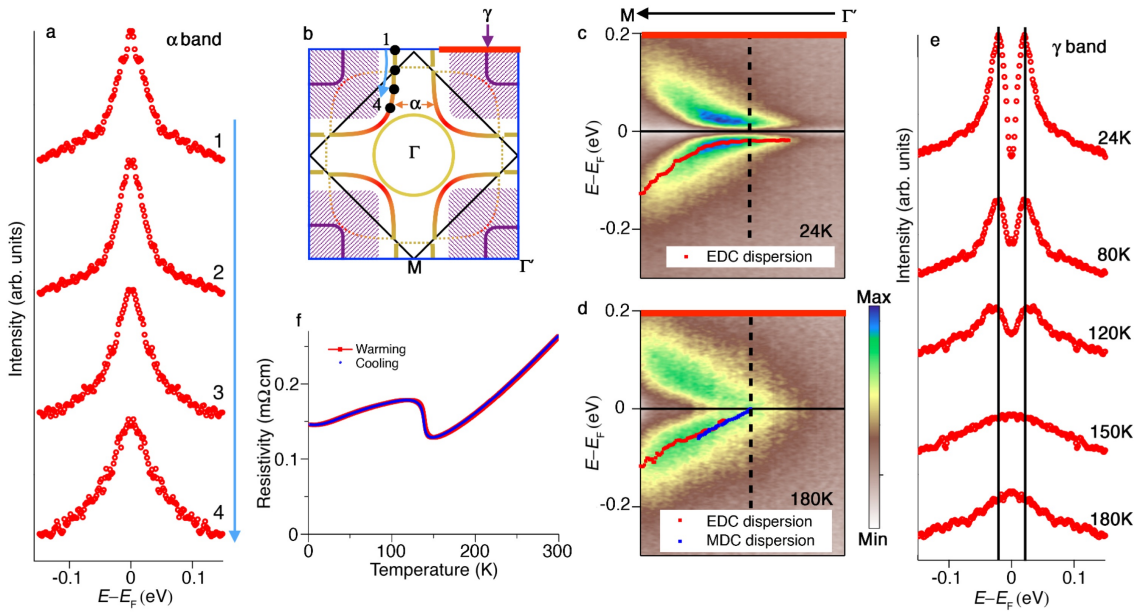

Figure 6.7: Temperature evolution of energy gaps. Panel a, symmetrized EDCs at multiple k_F positions of the α band at 30K. Panel b, schematic of Fermi surface. The black dots indicate the k_F positions of the symmetrized EDCs in panel a. Panel c and d, spectra at 24K and 180K. k_F is indicated by the dashed line. The thick red line in b shows the position of the cuts in both c and d. The dots in the spectra are the EDC and MDC peak positions that sketch out the band dispersion. The band dispersions near E_F flatten at 24K but linearly disperse up to E_F at 180K. Panel e, symmetrized EDCs at multiple temperatures. Panel f, resistivity curve of $La_4Ni_3O_{10}$. The resistivity anomaly at ˜140K is consistent with the energy gap filling in between 120K and 150K.

in these two materials. Third, the back-folded band of the cuprate-like hole pocket in $La_4Ni_3O_{10}$ resembles the shadow band feature observed in the Fermi surface of cuprates. The origin of this shadow band phenomenon in cuprate is controversial [108][109][110][111]. It is believed to originate from the antiferromagnetic correlation or a structural distortion of the crystal. However, in $La_4Ni_3O_{10}$, this feature most likely arises from the broken translation symmetry due to the tilted Ni-O octahedra.

6.3.2 Unique Properties of $La_4Ni_3O_{10}$

In addition to these commonalities with the cuprates mentioned above, there are some unique properties observed in this material. First, the cuprate-like hole pocket in $La_4Ni_3O_{10}$ reveals no energy gap opening, unlike the underdoped multilayer cuprates [122] or the single layer nickelate ($Eu_{0.9}Sr_{1.1}NiO_4$) that both host pseudogap states [97]. The general trend of a pseudogap in the single-layer compound and smaller or absent pseudogap in higher dimensionality compounds (bilayer, trilayer, and infinite-layer perovskites, respectively) is fully consistent with the trends observed in other doped Mott insulators, including the cuprates [122][86], iridates [82][123], and ruthenates [124], even though the origin of the pseudogap in all of these compounds remains controversial.

Second, the band splitting expected from the multilayer coupling of this trilayer material is unresolved in our ARPES data (Fig. 6.2 and Fig. 6.5). This is in contrast to trilayer cuprate ($Bi_2Sr_2Ca_2Cu_3O_{10+\delta}$) that has revealed band splitting [125]. Some other layered transition-metal oxides have also revealed clear band splitting from bilayer coupling [126][127]. We consider two explanations why our experimental data does not show this band splitting. A) The band splitting may exist as calculated, but one of the two split bands is greatly reduced in intensity, possibly due to the matrix element effect, which is a combination of different photon energies, polarizations and experimental geometries (see section 6.2.3). In this scenario, we argue that the band observed in our ARPES data is due to the inner-plane nickel band from DFT (Fig. 6.6a-b and Fig. 6.3), since the k_F position of these two bands is extremely similar, leaving the outer nickel band (δ band in

Fig. 6.2g) unresolved. For Luttinger counting of the Fermi surface, this unresolved band should exist in order to give a correct electron filling in the system. B) The actual band splitting might be much weaker than expected from the DFT result, and if the splitting is comparable with the energy or momentum widths of the constituent states, the splitting will become unresolvable. Such a situation has previously been discussed in both bilayer [128] and trilayer [129] cuprates. In this case we would nominally expect that the centroid of the unresolved states would be at the calculated centroid of the split bands rather than at one of them, which is inconsistent with our experimental observation. On the other hand, the centroid of the non-split bands could be at a slightly different k-value if other states took up the required number of electrons missing from these bands, with the γ band being the most natural candidate; because it skims right along the Fermi surface, it can accommodate a large number of electrons with a minimal change in chemical potential. Further investigation is required to resolve this delicate band-splitting issue.

Third, the extra $d_{3z^2-r^2}$ character band in this material raises intriguing issues. The flat band dispersion of the γ hole pocket at low temperature shows a strong spectral weight right below the Fermi level (Fig. 6.7) and its residual spectral weight at the Fermi level covers a large area in k-space. The energy gap observed in this band exhibits a sharp coherence peak. For the pseudogaps in cuprates and some other transition metal oxides, the depletion of spectral weight instead of a coherent gap characterizes the opening of the pseudogap [58][97][82][130]. In this regard, the origin of this energy gap in $La_4Ni_3O_{10}$ may differ from the commonly known pseudogap state. On the other hand, the coincidence of the gap evolution with the resistivity anomaly implies the connection to the potential charge-density waves in this material [106][107]. However, the spread of the γ band in k space especially at low energy near the Fermi level implies it to be agnostic to certain nesting q vectors and the corresponding charge modulations. To fully determine the charge density wave origin, further studies of the electronic structure combined with other experimental techniques like scanning tunneling spectroscopy and X-ray diffraction are required and are beyond the scope of this work.

Fourth, the band top of the γ hole pocket is relatively close to the Fermi level and the band

dispersion is extremely flat near EF, which makes it susceptible to undergoing a Lifshitz transition that can lead to topology changes as well as a drastic change of carrier density on the Fermi surface. The Lifshitz transition has been a topic of intense discussion in various materials [131][132][133] and has been recently argued to have a close connection to superconductivity in layered iron-based superconductors [133][53][134][114][135]. The susceptibility to a Lifshitz transition in the γ hole pocket with minor changes of the chemical potential or band curvature gives the potential for fine tuning the electronic structure and topology in these compounds.

6.4 Conclusion

In summary, we present a comprehensive study of the electronic structure and dynamics of the trilayer nickelate ($La_4Ni_3O_{10}$). Our work reveals a hole pocket that resembles the cuprate hole Fermi surface and displays similar renormalization effects. These similarities in both electronic structure and dynamics imply a possibility that more cuprate properties may be achievable in this material including high T_C superconductivity. On the other hand, we found an extra $d_{3z^2-r^2}$ orbital band that displays an energy gap opening coinciding with the phase transition observed in the transport measurement. To separate the $d_{3z^2-r^2}$ orbital band from the cuprate-like hole pocket, future developments such as changing the carrier density by doping, or changing the uniaxial pressure with different layer-spacing elements may help to move the $d_{3z^2-r^2}$ orbital band away from the Fermi level, bringing the electronic structure of these materials even closer to that of the cuprates.

Bibliography

[1] Friedrich Reinert and Stefan Hüfner. Photoemission spectroscopy—from early days to recent applications. New Journal of Physics, 7(1):97, 2005.

[2] C. N. Berglund and W. E. Spicer. Photoemission studies of copper and silver: Theory. Phys. Rev., 136:A1030–A1044, Nov 1964.

[3] Stephan Hfner. Photoelectron Spectroscopy: Principles and Applications. Springer, 2003.

[4] Andrea Damascelli, Zahid Hussain, and Zhi-Xun Shen. Angle-resolved photoemission studies of the cuprate superconductors. Rev. Mod. Phys., 75:473–541, 2003.

[5] L. D. Landau. The theory of a fermi liquid. J. Exptl. Theoret. Phys. (U.S.S.R.), 30:1058–1064, 1956.

[6] H. Kamerlingh Onnes. Further experiments with liquid helium. d. on the change of electric resistance of pure metals at very low temperatures, etc. v. the disappearance of the resistance of mercury. Commun. Phys. Lab. Univ. Leiden. Suppl., 1911.

[7] W. A. Little. Possibility of synthesizing an organic superconductor. Phys. Rev., 134:A1416–A1424, 1964.

[8] R. S. Wang, Y. Gao, Z. B. Huang, and Chen X. J. Superconductivity above 120 kelvin in a chain link molecule. preprint arXiv:1703.06641, 2017.

[9] J. Bardeen, L. N. Cooper, and J. R. Schrieffer. Theory of superconductivity. Phys. Rev., 108:1175–1204, 1957.

[10] Fa Wang and Dung-Hai Lee. The electron-pairing mechanism of iron-based superconductors. Science, 332(6026):200, 04 2011.

[11] J. R. Schrieffer. Theory of superconductivity. Perseus Books, 1999.

[12] W. L. McMillan. Transition temperature of strong-coupled superconductors. Phys. Rev., 167:331–344, 1968.

[13] N E Hussey. Phenomenology of the normal state in-plane transport properties of high- t c cuprates. Journal of Physics: Condensed Matter, 20(12):123201, 2008.

[14] Chandra Varma. High-temperature superconductivity: Mind the pseudogap. Nature, 468(7321):184–185, 11 2010.

[15] B. Keimer, S. A. Kivelson, M. R. Norman, S. Uchida, and J. Zaanen. From quantum matter to high-temperature superconductivity in copper oxides. Nature, 518(7538):179–186, 02 2015.

[16] Neven Barii, Mun K. Chan, Yuan Li, Guichuan Yu, Xudong Zhao, Martin Dressel, Ana Smontara, and Martin Greven. Universal sheet resistance and revised phase diagram of the cuprate high-temperature superconductors. Proceedings of the National Academy of Sciences, 110(30):12235–12240, 2013.

[17] Yoichiro Nambu. Quasi-particles and gauge invariance in the theory of superconductivity. Phys. Rev., 117:648–663, 1960.

[18] L. P. Gorkov. On the energy spectrum of superconductors. J. Exptl. Theoret. Phys. (U.S.S.R.), 34:735–739, 1958.

[19] G. R. Stewart. Heavy-fermion systems. Rev. Mod. Phys, 56:755, 1984.

[20] G. M. Eliashberg. Interactions between electrons and lattice vibrations in a superconductor. J. Exptl. Theoret. Phys. (U.S.S.R.), 38:966–976, 1960.

[21] P. W. Anderson. The theory of Superconductivity in the High-TC Cuprate Superconductors. Princeton University Press, 1997.

[22] T. Senthil and Matthew P. A. Fisher. Z_2. Phys. Rev. B, 62:7850–7881, 2000.

[23] Emanuel Gull, Olivier Parcollet, and Andrew J. Millis. Superconductivity and the pseudogap in the two-dimensional hubbard model. Phys. Rev. Lett., 110:216405, 2013.

[24] J. P. F. LeBlanc, Andrey E. Antipov, Federico Becca, Ireneusz W. Bulik, Garnet Kin-Lic Chan, Chia-Min Chung, Youjin Deng, Michel Ferrero, Thomas M. Henderson, Carlos A. Jiménez-Hoyos, E. Kozik, Xuan-Wen Liu, Andrew J. Millis, N. V. Prokof'ev, Mingpu Qin, Gustavo E. Scuseria, Hao Shi, B. V. Svistunov, Luca F. Tocchio, I. S. Tupitsyn, Steven R. White, Shiwei Zhang, Bo-Xiao Zheng, Zhenyue Zhu, and Emanuel Gull. Solutions of the two-dimensional hubbard model: Benchmarks and results from a wide range of numerical algorithms. Phys. Rev. X, 5:041041, 2015.

[25] Thomas Faulkner, Nabil Iqbal, Hong Liu, John McGreevy, and David Vegh. Strange metal transport realized by gauge/gravity duality. Science, 329(5995):1043–1047, 2010.

[26] Subir Sachdev. Holographic metals and the fractionalized fermi liquid. Phys. Rev. Lett., 105:151602, 2010.

[27] Aristomenis Donos and Sean A. Hartnoll. Interaction-driven localization in holography. Nat Phys, 9(10):649–655, 10 2013.

[28] Philip W. Phillips, Brandon W. Langley, and Jimmy A. Hutasoit. Un-fermi liquids: Unparticles in strongly correlated electron matter. Phys. Rev. B, 88:115129, 2013.

[29] J. E. Hirsch. Superconductivity from undressing. Phys. Rev. B, 62:14487–14497, 2000.

[30] Ar. Abanov and Andrey V. Chubukov. A relation between the resonance neutron peak and arpes data in cuprates. Phys. Rev. Lett., 83:1652–1655, 1999.

[31] M. R. Norman, M. Randeria, H. Ding, and J. C. Campuzano. Phenomenology of the low-energy spectral function in high-T_c superconductors. Phys. Rev. B, 57:R11093–R11096, 1998.

[32] Philip A. Casey and Philip W. Anderson. Hidden fermi liquid: Self-consistent theory for the normal state of high-T_c superconductors. Phys. Rev. Lett., 106:097002, 2011.

[33] T. J. Reber, X. Zhou, N.C. Plumb, S. Parham, J.A. Waugh, Y. Cao, Z. Sun, H. Li, Q. Wang, J.S. Wen, Z.J. Xu, G. Gu, Y. Yoshida, H. Eisaki, G.B. Arnold, and D. S. Dessau. Power law liquid - a unified form of low-energy nodal electronic interactions in hole doped cuprate superconductors. preprint arXiv:1509.01611, 2015.

[34] T. Valla, A. V. Fedorov, P. D. Johnson, Q. Li, G. D. Gu, and N. Koshizuka. Temperature dependent scattering rates at the fermi surface of optimally doped $bi_2sr_2cacu_2O_{8+\delta}$. Phys. Rev. Lett., 85:828–831, 2000.

[35] C. G. Olson, R. Liu, D. W. Lynch, R. S. List, A. J. Arko, B. W. Veal, Y. C. Chang, P. Z. Jiang, and A. P. Paulikas. High-resolution angle-resolved photoemission study of the fermi surface and the normal-state electronic structure of $bi_2sr_2cacu_2o_8$. Phys. Rev. B, 42:381–386, Jul 1990.

[36] C. M. Varma, P. B. Littlewood, S. Schmitt-Rink, E. Abrahams, and A. E. Ruckenstein. Phenomenology of the normal state of cu-o high-temperature superconductors. Phys. Rev. Lett., 63:1996–1999, 1989.

[37] A. Kaminski, M. Randeria, J. C. Campuzano, M. R. Norman, H. Fretwell, J. Mesot, T. Sato, T. Takahashi, and K. Kadowaki. Renormalization of spectral line shape and dispersion below T_c in $bi_2sr_2cacu_2O_{8+\delta}$. Phys. Rev. Lett., 86:1070–1073, 2001.

[38] A. Lanzara, P. V. Bogdanov, X. J. Zhou, S. A. Kellar, D. L. Feng, E. D. Lu, T. Yoshida, H. Eisaki, A. Fujimori, K. Kishio, J. I. Shimoyama, T. Noda, S. Uchida, Z. Hussain, and Z. X. Shen. Evidence for ubiquitous strong electron-phonon coupling in high-temperature superconductors. Nature, 412(6846):510–514, 08 2001.

[39] P. D. Johnson, T. Valla, A. V. Fedorov, Z. Yusof, B. O. Wells, Q. Li, A. R. Moodenbaugh, G. D. Gu, N. Koshizuka, C. Kendziora, Sha Jian, and D. G. Hinks. Doping and temperature dependence of the mass enhancement observed in the cuprate $bi_2sr_2cacu_2O_{8+\delta}$. Phys. Rev. Lett., 87:177007, 2001.

[40] H. Iwasawa, J. F. Douglas, K. Sato, T. Masui, Y. Yoshida, Z. Sun, H. Eisaki, H. Bando, A. Ino, M. Arita, K. Shimada, H. Namatame, M. Taniguchi, S. Tajima, S. Uchida, T. Saitoh, D. S. Dessau, and Y. Aiura. Isotopic fingerprint of electron-phonon coupling in high-T_c cuprates. Phys. Rev. Lett., 101:157005, 2008.

[41] T. K. Kim, A. A. Kordyuk, S. V. Borisenko, A. Koitzsch, M. Knupfer, H. Berger, and J. Fink. Doping dependence of the mass enhancement in $(Pb,Bi)_2sr_2cacu_2o_8$ at the antinodal point in the superconducting and normal states. Phys. Rev. Lett., 91:167002, 2003.

[42] A. D. Gromko, A. V. Fedorov, Y.-D. Chuang, J. D. Koralek, Y. Aiura, Y. Yamaguchi, K. Oka, Yoichi Ando, and D. S. Dessau. Mass-renormalized electronic excitations at $(\pi, 0)$ in the superconducting state of $bi_2sr_2cacu_2o_{8+\delta}$. Phys. Rev. B, 68:174520, 2003.

[43] T. Cuk, F. Baumberger, D. H. Lu, N. Ingle, X. J. Zhou, H. Eisaki, N. Kaneko, Z. Hussain, T. P. Devereaux, N. Nagaosa, and Z.-X. Shen. Coupling of the B_{1g} phonon to the antinodal electronic states of $bi_2sr_2ca_{0.92}y_{0.08}cu_2o_{8+\delta}$. Phys. Rev. Lett., 93:117003, 2004.

[44] M. R. Norman, M. Eschrig, A. Kaminski, and J. C. Campuzano. Momentum distribution curves in the superconducting state. Phys. Rev. B, 64:184508, 2001.

[45] Y.-D. Chuang, A. D. Gromko, D. S. Dessau, Y. Aiura, Y. Yamaguchi, K. Oka, A. J. Arko, J. Joyce, H. Eisaki, S. I. Uchida, K. Nakamura, and Yoichi Ando. Reexamination of the electronic structure of $Bi_2Sr_2CaCu_2O_{8+\delta}$ and $Bi_2Sr_2Cu_1O_{6+\delta}$: Electronlike portions of the fermi surface and depletion of spectral weight near $\overline{m}$. Phys. Rev. Lett., 83:3717–3720, 1999.

[46] S. V. Borisenko, M. S. Golden, S. Legner, T. Pichler, C. Dürr, M. Knupfer, J. Fink, G. Yang, S. Abell, and H. Berger. Joys and pitfalls of fermi surface mapping in $bi_2sr_2cacu_2O_{8+\delta}$ using angle resolved photoemission. Phys. Rev. Lett., 84:4453–4456, 2000.

[47] Y.-D. Chuang, A. D. Gromko, A. Fedorov, Y. Aiura, K. Oka, Yoichi Ando, H. Eisaki, S. I. Uchida, and D. S. Dessau. Doubling of the bands in overdoped $Bi_2Sr_2CaCu_2O_{8+\delta}$: Evidence for c-axis bilayer coupling. Phys. Rev. Lett., 87:117002, 2001.

[48] D. L. Feng, N. P. Armitage, D. H. Lu, A. Damascelli, J. P. Hu, P. Bogdanov, A. Lanzara, F. Ronning, K. M. Shen, H. Eisaki, C. Kim, Z.-X. Shen, J.-i. Shimoyama, and K. Kishio. Bilayer splitting in the electronic structure of heavily overdoped $bi_2sr_2cacu_2O_{8+\delta}$. Phys. Rev. Lett., 86:5550–5553, 2001.

[49] T. J. Reber, N. C. Plumb, J. A. Waugh, and D. S. Dessau. Effects, determination, and correction of count rate nonlinearity in multi-channel analog electron detectors. Review of Scientific Instruments, 85(4):043907, 2014.

[50] T. Dahm, V. Hinkov, S. V. Borisenko, A. A. Kordyuk, V. B. Zabolotnyy, J. Fink, B. Buchner, D. J. Scalapino, W. Hanke, and B. Keimer. Strength of the spin-fluctuation-mediated pairing interaction in a high-temperature superconductor. Nat Phys, 5(3):217–221, 03 2009.

[51] D. S. Inosov, S. V. Borisenko, I. Eremin, A. A. Kordyuk, V. B. Zabolotnyy, J. Geck, A. Koitzsch, J. Fink, M. Knupfer, B. Büchner, H. Berger, and R. Follath. Relation between the one-particle spectral function and dynamic spin susceptibility of superconducting $bi_2sr_2Cacu_2o_{8-\delta}$. Phys. Rev. B, 75:172505, May 2007.

[52] J. W. Alldredge, Jinho Lee, K. McElroy, M. Wang, K. Fujita, Y. Kohsaka, C. Taylor, H. Eisaki, S. Uchida, P. J. Hirschfeld, and J. C. Davis. Evolution of the electronic excitation spectrum with strongly diminishing hole density in superconducting bi2sr2cacu2o8+[delta]. Nat Phys, 4(4):319–326, 04 2008.

[53] A. A. Kordyuk, S. V. Borisenko, A. Koitzsch, J. Fink, M. Knupfer, and H. Berger. Bare electron dispersion from experiment: Self-consistent self-energy analysis of photoemission data. Phys. Rev. B, 71:214513, 2005.

[54] Jin Mo Bok, Jong Ju Bae, Han-Yong Choi, Chandra M. Varma, Wentao Zhang, Junfeng He, Yuxiao Zhang, Li Yu, and X. J. Zhou. Quantitative determination of pairing interactions for high-temperature superconductivity in cuprates. Science Advances, 2(3), 2016.

[55] Jin Mo Bok, Jae Hyun Yun, Han-Yong Choi, Wentao Zhang, X. J. Zhou, and Chandra M. Varma. Momentum dependence of the single-particle self-energy and fluctuation spectrum of slightly underdoped $bi_2sr_2cacu_2o_{8+\delta}$ from high-resolution laser angle-resolved photoemission. Phys. Rev. B, 81:174516, 2010.

[56] D. L. Feng, D. H. Lu, K. M. Shen, C. Kim, H. Eisaki, A. Damascelli, R. Yoshizaki, J.-i. Shimoyama, K. Kishio, G. D. Gu, S. Oh, A. Andrus, J. O'Donnell, J. N. Eckstein, and Z.-X. Shen. Signature of superfluid density in the single-particle excitation spectrum of bi2sr2cacu2o8+. Science, 289(5477):277–281, 2000.

[57] Kiyohisa Tanaka, W. S. Lee, D. H. Lu, A. Fujimori, T. Fujii, Risdiana, I. Terasaki, D. J. Scalapino, T. P. Devereaux, Z. Hussain, and Z.-X. Shen. Distinct fermi-momentum-dependent energy gaps in deeply underdoped bi2212. Science, 314(5807):1910–1913, 2006.

[58] Takeshi Kondo, Yoichiro Hamaya, Ari D. Palczewski, Tsunehiro Takeuchi, J. S. Wen, Z. J. Xu, Genda Gu, Jorg Schmalian, and Adam Kaminski. Disentangling cooper-pair formation above the transition temperature from the pseudogap state in the cuprates. Nat Phys, 7(1):21–25, 01 2011.

[59] T. J. Reber, N. C. Plumb, Y. Cao, Z. Sun, Q. Wang, K. McElroy, H. Iwasawa, M. Arita, J. S. Wen, Z. J. Xu, G. Gu, Y. Yoshida, H. Eisaki, Y. Aiura, and D. S. Dessau. Prepairing and the "filling" gap in the cuprates from the tomographic density of states. Phys. Rev. B, 87:060506, 2013.

[60] Yayu Wang, Z. A. Xu, T. Kakeshita, S. Uchida, S. Ono, Yoichi Ando, and N. P. Ong. Onset of the vortexlike nernst signal above T_c in $la_{2-x}sr_xcuo_4$ and $bi_2sr_{2-y}la_ycuo_6$. Phys. Rev. B, 64:224519, 2001.

[61] T. Cuk, D. H. Lu, X. J. Zhou, Z.-X. Shen, T. P. Devereaux, and N. Nagaosa. A review of electronphonon coupling seen in the high-tc superconductors by angle-resolved photoemission studies (arpes). physica status solidi (b), 242(1):11–29, 2005.

[62] A. A. Kordyuk, S. V. Borisenko, V. B. Zabolotnyy, J. Geck, M. Knupfer, J. Fink, B. Büchner, C. T. Lin, B. Keimer, H. Berger, A. V. Pan, Seiki Komiya, and Yoichi Ando. Constituents of the quasiparticle spectrum along the nodal direction of high-T_c cuprates. Phys. Rev. Lett., 97:017002, 2006.

[63] R. S. Wang, Y. Gao, Z. B. Huang, and X. J. Chen. Superconductivity in p-terphenyl. preprint arXiv:1703.05803, 2017.

[64] R. S. Wang, Y. Gao, Z. B. Huang, and X. J. Chen. Superconductivity at 43 k in a single c-c bond linked terpheny. preprint arXiv:1703.05804, 2017.

[65] Andrew P. Rice, Fook S. Tham, and Eric L. Chronister. A temperature dependent x-ray study of the order–disorder enantiotropic phase transition of p-terphenyl. Journal of Chemical Crystallography, 43(1):14–25, 2013.

[66] N. I Nijegorodov, W. S Downey, and M. B Danailov. Systematic investigation of absorption, fluorescence and laser properties of some p- and m-oligophenylenes. Spectrochimica Acta Part A: Molecular and Biomolecular Spectroscopy, 56(4):783–795, 2000.

[67] Benjamin Mahns, Friedrich Roth, and Martin Knupfer. Absence of photoemission from the fermi level in potassium intercalated picene and coronene films: Structure, polaron, or correlation physics? The Journal of Chemical Physics, 136(13):134503, 2017/09/15 2012.

[68] Andreas Ruff, Michael Sing, Ralph Claessen, Hunpyo Lee, Milan Tomić, Harald O. Jeschke, and Roser Valentí. Absence of metallicity in k-doped picene: Importance of electronic correlations. Phys. Rev. Lett., 110:216403, 2013.

[69] W. L. Yang, V. Brouet, X. J. Zhou, Hyoung J. Choi, Steven G. Louie, Marvin L. Cohen, S. A. Kellar, P. V. Bogdanov, A. Lanzara, A. Goldoni, F. Parmigiani, Z. Hussain, and Z. X. Shen. Band structure and fermi surface of electron-doped c₆₀ monolayers. Science, 300(5617):303, 2003.

[70] T. J. Reber, N. C. Plumb, Z. Sun, Y. Cao, Q. Wang, K. McElroy, H. Iwasawa, M. Arita, J. S. Wen, Z. J. Xu, G. Gu, Y. Yoshida, H. Eisaki, Y. Aiura, and D. S. Dessau. The origin and non-quasiparticle nature of fermi arcs in bi2sr2cacu2o8+[delta]. Nat Phys, 8(8):606–610, 08 2012.

[71] Takeshi Kondo, W. Malaeb, Y. Ishida, T. Sasagawa, H. Sakamoto, Tsunehiro Takeuchi, T. Tohyama, and S. Shin. Point nodes persisting far beyond tc in bi2212. 6:7699 EP –, 07 2015.

[72] R. C. Dynes, V. Narayanamurti, and J. P. Garno. Direct measurement of quasiparticle-lifetime broadening in a strong-coupled superconductor. Phys. Rev. Lett., 41:1509–1512, 1978.

[73] Makoto Hashimoto, Rui-Hua He, Kiyohisa Tanaka, Jean-Pierre Testaud, Worawat Meevasana, Rob G. Moore, Donghui Lu, Hong Yao, Yoshiyuki Yoshida, Hiroshi Eisaki, Thomas P. Devereaux, Zahid Hussain, and Zhi-Xun Shen. Particle-hole symmetry breaking in the pseudogap state of bi2201. Nat Phys, 6(6):414–418, 06 2010.

[74] M. Q. Ren, W. Chen, Q. Liu, Y. J.and Chen Y. J. Chen, C.and Qiao, G. Zhou, Y. J. Zhang, T.and Yan, and D. L. Feng. Observation of novel gapped phases in potassium doped single layer p-terphenyl on au (111). preprint arXiv:1705.09901, 2017.

[75] M. Yi, Y. Zhang, Z. K. Liu, X. Ding, J. H. Chu, A. F. Kemper, N. Plonka, B. Moritz, M. Hashimoto, S. K. Mo, Z. Hussain, T. P. Devereaux, I. R. Fisher, H. H. Wen, Z. X. Shen, and D. H. Lu. Dynamic competition between spin-density wave order and superconductivity in underdoped ba1xkxfe2as2. 5:3711 EP –, 04 2014.

[76] John H. Davies and Judy R. Franz. Coulomb gap in sodium tungsten bronzes. Phys. Rev. Lett., 57:475–478, Jul 1986.

[77] Z.-H. Pan, P. Richard, Y.-M. Xu, M. Neupane, P. Bishay, A. V. Fedorov, H. Luo, L. Fang, H.-H. Wen, Z. Wang, and H. Ding. Evolution of fermi surface and normal-state gap in the chemically substituted cuprates $bi_2sr_{2-x}bi_xcuo_{6+\delta}$. Phys. Rev. B, 79:092507, 2009.

[78] H. Ding, T. Yokoya, J. C. Campuzano, T. Takahashi, M. Randeria, M. R. Norman, T. Mochiku, K. Kadowaki, and J. Giapintzakis. Spectroscopic evidence for a pseudogap in the normal state of underdoped high-tc superconductors. Nature, 382(6586):51–54, 07 1996.

[79] A. Ino, T. Mizokawa, K. Kobayashi, A. Fujimori, T. Sasagawa, T. Kimura, K. Kishio, K. Tamasaku, H. Eisaki, and S. Uchida. Doping dependent density of states and pseudogap behavior in $la_{2-x}sr_xcuo_4$. Phys. Rev. Lett., 81:2124–2127, 1998.

[80] Kyle M. Shen, F. Ronning, D. H. Lu, F. Baumberger, N. J. C. Ingle, W. S. Lee, W. Meevasana, Y. Kohsaka, M. Azuma, M. Takano, H. Takagi, and Z. X. Shen. Nodal quasiparticles and antinodal charge ordering in ca_{2-x}na_xcuo₂cl₂. Science, 307(5711):901, 02 2005.

[81] Y. D. Chuang, A. D. Gromko, D. S. Dessau, T. Kimura, and Y. Tokura. Fermi surface nesting and nanoscale fluctuating charge/orbital ordering in colossal magnetoresistive oxides. Science, 292(5521):1509, 05 2001.

[82] Yue Cao, Qiang Wang, Justin A. Waugh, Theodore J. Reber, Haoxiang Li, Xiaoqing Zhou, Stephen Parham, S. R. Park, Nicholas C. Plumb, Eli Rotenberg, Aaron Bostwick, Jonathan D. Denlinger, Tongfei Qi, Michael A. Hermele, Gang Cao, and Daniel S. Dessau. Hallmarks of the mott-metal crossover in the hole-doped pseudospin-1/2 mott insulator sr2iro4. 7:11367 EP –, 04 2016.

[83] N. F. Mott. The basis of the electron theory of metals, with special reference to the transition metals. Proceedings of the Physical Society. Section A, 62(7):416, 1949.

[84] A. S. Alexandrov and N. F. Mott. Do pairs exist above t c ? Superconductor Science and Technology, 6(4):215, 1993.

[85] S. H. Pan, J. P. O'Neal, R. L. Badzey, C. Chamon, H. Ding, J. R. Engelbrecht, Z. Wang, H. Eisaki, S. Uchida, A. K. Gupta, K. W. Ng, E. W. Hudson, K. M. Lang, and J. C. Davis. Microscopic electronic inhomogeneity in the high-tc superconductor bi2sr2cacu2o8+x. Nature, 413(6853):282–285, 09 2001.

[86] Makoto Hashimoto, Inna M. Vishik, Rui-Hua He, Thomas P. Devereaux, and Zhi-Xun Shen. Energy gaps in high-transition-temperature cuprate superconductors. Nat Phys, 10(7):483–495, 07 2014.

[87] Y. K. Kim, O. Krupin, J. D. Denlinger, A. Bostwick, E. Rotenberg, Q. Zhao, J. F. Mitchell, J. W. Allen, and B. J. Kim. Fermi arcs in a doped pseudospin-1/2 heisenberg antiferromagnet. Science, 345(6193):187, 07 2014.

[88] J. Chang, E. Blackburn, A. T. Holmes, N. B. Christensen, J. Larsen, J. Mesot, Ruixing Liang, D. A. Bonn, W. N. Hardy, A. Watenphul, M. v. Zimmermann, E. M. Forgan, and S. M. Hayden. Direct observation of competition between superconductivity and charge density wave order in yba2cu3o6.67. Nat Phys, 8(12):871–876, 12 2012.

[89] G. H. Zhong, X. H. Wang, R. S. Wang, J. X. Han, C. Zhang, X. J. Chen, and H. Q. Lin. Structural and bonding character of potassium-doped p-terphenyl superconductors. preprint arXiv:1706.03965, 2017.

[90] Shin ichi Uchida, Hidenori Takagi, Koichi Kitazawa, and Shoji Tanaka. High t c superconductivity of la-ba-co oxides. Japanese Journal of Applied Physics, 26(1A):L1, 1987.

[91] Yayu Wang, Lu Li, and N. P. Ong. Nernst effect in high-T_c superconductors. Phys. Rev. B, 73:024510, 2006.

[92] Wu Xiao-Lin Cheng Jia Deng Tian-Guo Yan Xun-Wang Huang Zhong-Bing Gao Yun, Wang Ren-Shu. Searching superconductivity in potassium-doped p-terphenyl. Acta Physica Sinica, 65(7):77402, 2016.

[93] B. J. Powell and Ross H. McKenzie. Half-filled layered organic superconductors and the resonating-valence-bond theory of the hubbard-heisenberg model. Phys. Rev. Lett., 94:047004, 2005.

[94] L. D. Kispert, J. Joseph, G. G. Miller, and R. H. Baughman. Epr study of polarons in a conducting polymer with nondegenerate ground states: Alkali metal complexes of poly (pphenylene) and phenylene oligomers. The Journal of Chemical Physics, 81(4):2119–2125, 2017/09/15 1984.

[95] J. Zaanen, G. A. Sawatzky, and J. W. Allen. Band gaps and electronic structure of transition-metal compounds. Phys. Rev. Lett., 55:418–421, 1985.

[96] Viktor V. Poltavets, Konstantin A. Lokshin, Andriy H. Nevidomskyy, Mark Croft, Trevor A. Tyson, Joke Hadermann, Gustaaf Van Tendeloo, Takeshi Egami, Gabriel Kotliar, Nicholas ApRoberts-Warren, Adam P. Dioguardi, Nicholas J. Curro, and Martha Greenblatt. Bulk magnetic order in a two-dimensional ni^{1+}/ni^{2+} (d^9/d^8) nickelate, isoelectronic with superconducting cuprates. Phys. Rev. Lett., 104:206403, 2010.

[97] M. Uchida, K. Ishizaka, P. Hansmann, Y. Kaneko, Y. Ishida, X. Yang, R. Kumai, A. Toschi, Y. Onose, R. Arita, K. Held, O. K. Andersen, S. Shin, and Y. Tokura. Pseudogap of metallic layered nickelate $R_{2-x}sr_xnio_4$ ($r = \mathrm{Nd}, \mathrm{Eu}$) crystals measured using angle-resolved photoemission spectroscopy. Phys. Rev. Lett., 106:027001, 2011.

[98] M. Uchida, Y. Yamasaki, Y. Kaneko, K. Ishizaka, J. Okamoto, H. Nakao, Y. Murakami, and Y. Tokura. Pseudogap-related charge dynamics in the layered nickelate $R_{2-x}sr_xnio_4$ ($x \sim 1$). Phys. Rev. B, 86:165126, 2012.

[99] S. Anissimova, D. Parshall, G. D. Gu, K. Marty, M. D. Lumsden, Songxue Chi, J. A. Fernandez-Baca, D. L. Abernathy, D. Lamago, J. M. Tranquada, and D. Reznik. Direct observation of dynamic charge stripes in la2–xsrxnio4. 5:3467 EP –, 03 2014.

[100] Ji ří Chaloupka and Giniyat Khaliullin. Orbital order and possible superconductivity in $lanio_3/lamo_3$ superlattices. Phys. Rev. Lett., 100:016404, 2008.

[101] H. Y. Hwang, Y. Iwasa, M. Kawasaki, B. Keimer, N. Nagaosa, and Y. Tokura. Emergent phenomena at oxide interfaces. Nat Mater, 11(2):103–113, 02 2012.

[102] Anand Bhattacharya and Steven J. May. Magnetic oxide heterostructures. Annual Review of Materials Research, 44(1):65–90, 2014.

[103] Junjie Zhang, Yu-Sheng Chen, D. Phelan, Hong Zheng, M. R. Norman, and J. F. Mitchell. Stacked charge stripes in the quasi-2d trilayer nickelate la4ni3o8. Proceedings of the National Academy of Sciences, 113(32):8945–8950, 2016.

[104] Junjie Zhang, A. S. Botana, J. W. Freeland, D. Phelan, Hong Zheng, V. Pardo, M. R. Norman, and J. F. Mitchell. Large orbital polarization in a metallic square-planar nickelate. Nat Phys, 13(9):864–869, 09 2017.

[105] Antia S. Botana, Victor Pardo, Warren E. Pickett, and Michael R. Norman. Charge ordering in ni^{1+}/ni^{2+} nickelates: $la_4ni_3o_8$ and $la_3ni_2o_6$. Phys. Rev. B, 94:081105, Aug 2016.

[106] M. D. Carvalho, M. M. Cruz, A. Wattiaux, J. M. Bassat, F. M. A. Costa, and M. Godinho. Influence of oxygen stoichiometry on the electronic properties of la4ni3o10. Journal of Applied Physics, 88(1):544–549, 2000.

[107] D. K. Seo, W. Liang, M. H. Whangbo, Z. Zhang, and M. Greenblatt. Electronic band structure and madelung potential study of the nickelates la2nio4, la3ni2o7, and la4ni3o10. Inorganic Chemistry, 35(22):6396–6400, 01 1996.

[108] K. Nakayama, T. Sato, T. Dobashi, K. Terashima, S. Souma, H. Matsui, T. Takahashi, J. C. Campuzano, K. Kudo, T. Sasaki, N. Kobayashi, T. Kondo, T. Takeuchi, K. Kadowaki, M. Kofu, and K. Hirota. Shadow bands in single-layered $bi_2sr_2Cuo_{6+\delta}$ studied by angle-resolved photoemission spectroscopy. Phys. Rev. B, 74:054505, 2006.

[109] R-H He, X J Zhou, M Hashimoto, T Yoshida, K Tanaka, S-K Mo, T Sasagawa, N Mannella, W Meevasana, H Yao, M Fujita, T Adachi, S Komiya, S Uchida, Y Ando, F Zhou, Z X Zhao, A Fujimori, Y Koike, K Yamada, Z Hussain, and Z-X Shen. Doping dependence of the (,) shadow band in la-based cuprates studied by angle-resolved photoemission spectroscopy. New Journal of Physics, 13(1):013031, 2011.

[110] A. Mans, I. Santoso, Y. Huang, W. K. Siu, S. Tavaddod, V. Arpiainen, M. Lindroos, H. Berger, V. N. Strocov, M. Shi, L. Patthey, and M. S. Golden. Experimental proof of a structural origin for the shadow fermi surface of $bi_2sr_2cacu_2o_{8+\delta}$. Phys. Rev. Lett., 96:107007, 2006.

[111] A. Koitzsch, S. V. Borisenko, A. A. Kordyuk, T. K. Kim, M. Knupfer, J. Fink, M. S. Golden, W. Koops, H. Berger, B. Keimer, C. T. Lin, S. Ono, Y. Ando, and R. Follath. Origin of the shadow fermi surface in Bi-based cuprates. Phys. Rev. B, 69:220505, 2004.

[112] Wei Ku, Tom Berlijn, and Chi-Cheng Lee. Unfolding first-principles band structures. Phys. Rev. Lett., 104:216401, 2010.

[113] Chia-Hui Lin, Tom Berlijn, Limin Wang, Chi-Cheng Lee, Wei-Guo Yin, and Wei Ku. One-fe versus two-fe brillouin zone of fe-based superconductors: Creation of the electron pockets by translational symmetry breaking. Phys. Rev. Lett., 107:257001, 2011.

[114] V. Brouet, M. Fuglsang Jensen, Ping-Hui Lin, A. Taleb-Ibrahimi, P. Le Fèvre, F. Bertran, Chia-Hui Lin, Wei Ku, A. Forget, and D. Colson. Impact of the two fe unit cell on the electronic structure measured by arpes in iron pnictides. Phys. Rev. B, 86:075123, 2012.

[115] Karlheinz Schwarz and Peter Blaha. Solid state calculations using wien2k. Computational Materials Science, 28(2):259–273, 2003.

[116] E Sjstedt, L Nordstrm, and D.J Singh. An alternative way of linearizing the augmented plane-wave method. Solid State Communications, 114(1):15 – 20, 2000.

[117] John P. Perdew, Kieron Burke, and Matthias Ernzerhof. Generalized gradient approximation made simple. Phys. Rev. Lett., 77:3865–3868, 1996.

[118] Yue Cao, J. A. Waugh, X-W. Zhang, J-W. Luo, Q. Wang, T. J. Reber, S. K. Mo, Z. Xu, A. Yang, J. Schneeloch, G. D. Gu, M. Brahlek, N. Bansal, S. Oh, A. Zunger, and D. S. Dessau. Mapping the orbital wavefunction of the surface states in three-dimensional topological insulators. Nat Phys, 9(8):499–504, 08 2013.

[119] Masato Emori, Akiko Sakino, Kenichi Ozawa, and Hiroshi Sakama. Polarization-dependent arpes measurement for valence band of anatase tio2. Solid State Communications, 188(Supplement C):15–18, 2014.

[120] R. Müller, M. Schneider, C. Janowitz, R. St. Unger, T. Stemmler, A. Krapf, H. Dwelk, R. Manzke, K. Roßnagel, L. Kipp, and M. Skibowski. Fermi surface map of the single-layer bi-cuprate bi2sr2 xlaxcuo6 + at optimal doping. Journal of Superconductivity, 14(6):659–668, 2001.

[121] Y. Zhang, C. He, Z. R. Ye, J. Jiang, F. Chen, M. Xu, Q. Q. Ge, B. P. Xie, J. Wei, M. Aeschlimann, X. Y. Cui, M. Shi, J. P. Hu, and D. L. Feng. Symmetry breaking via orbital-dependent reconstruction of electronic structure in detwinned nafeas. Phys. Rev. B, 85:085121, 2012.

[122] A. G. Loeser, Z.-X. Shen, D. S. Dessau, D. S. Marshall, C. H. Park, P. Fournier, and A. Kapitulnik. Excitation gap in the normal state of underdoped bi2sr2cacu2o8+. Science, 273(5273):325–329, 1996.

[123] Q. Wang, Y. Cao, J. A. Waugh, S. R. Park, T. F. Qi, O. B. Korneta, G. Cao, and D. S. Dessau. Dimensionality-controlled mott transition and correlation effects in single-layer and bilayer perovskite iridates. Phys. Rev. B, 87:245109, 2013.

[124] J. S. Lee, S. J. Moon, B. J. Yang, Jaejun Yu, U. Schade, Y. Yoshida, S.-I. Ikeda, and T. W. Noh. Pseudogap dependence of the optical conductivity spectra of $ca_3ru_2o_7$: A possible contribution of the orbital flip excitation. Phys. Rev. Lett., 98:097403, 2007.

[125] S. Ideta, K. Takashima, M. Hashimoto, T. Yoshida, A. Fujimori, H. Anzai, T. Fujita, Y. Nakashima, A. Ino, M. Arita, H. Namatame, M. Taniguchi, K. Ono, M. Kubota, D. H. Lu, Z.-X. Shen, K. M. Kojima, and S. Uchida. Enhanced superconducting gaps in the trilayer high-temperature $bi_2sr_2ca_2cu_3o_{10+\delta}$ cuprate superconductor. Phys. Rev. Lett., 104:227001, 2010.

[126] L. Moreschini, S. Moser, A. Ebrahimi, B. Dalla Piazza, K. S. Kim, S. Boseggia, D. F. McMorrow, H. M. Rønnow, J. Chang, D. Prabhakaran, A. T. Boothroyd, E. Rotenberg, A. Bostwick, and M. Grioni. Bilayer splitting and wave functions symmetry in $sr_3ir_2o_7$. Phys. Rev. B, 89:201114, 2014.

[127] Z. Sun, Y.-D. Chuang, A. V. Fedorov, J. F. Douglas, D. Reznik, F. Weber, N. Aliouane, D. N. Argyriou, H. Zheng, J. F. Mitchell, T. Kimura, Y. Tokura, A. Revcolevschi, and D. S. Dessau. Quasiparticlelike peaks, kinks, and electron-phonon coupling at the $(\pi, 0)$ regions in the cmr oxide $la_{2-2x}sr_{1+2x}mn_2o_7$. Phys. Rev. Lett., 97:056401, 2006.

[128] H. Ding, A. F. Bellman, J. C. Campuzano, M. Randeria, M. R. Norman, T. Yokoya, T. Takahashi, H. Katayama-Yoshida, T. Mochiku, K. Kadowaki, G. Jennings, and G. P. Brivio.

Electronic excitations in $bi_2sr_2Cacu_2O_8$: Fermi surface, dispersion, and absence of bilayer splitting. Phys. Rev. Lett., 76:1533–1536, 1996.

[129] D. L. Feng, A. Damascelli, K. M. Shen, N. Motoyama, D. H. Lu, H. Eisaki, K. Shimizu, J.-i. Shimoyama, K. Kishio, N. Kaneko, M. Greven, G. D. Gu, X. J. Zhou, C. Kim, F. Ronning, N. P. Armitage, and Z.-X Shen. Electronic structure of the trilayer cuprate superconductor $bi_2sr_2ca_2cu_3O_{10+\delta}$. Phys. Rev. Lett., 88:107001, 2002.

[130] N. Mannella, W. L. Yang, X. J. Zhou, H. Zheng, J. F. Mitchell, J. Zaanen, T. P. Devereaux, N. Nagaosa, Z. Hussain, and Z. X. Shen. Nodal quasiparticle in pseudogapped colossal magnetoresistive manganites. Nature, 438(7067):474–478, 11 2005.

[131] I. Pletikosić, G. D. Gu, and T. Valla. Inducing a lifshitz transition by extrinsic doping of surface bands in the topological crystalline insulator $pb_{1-x}sn_xSe$. Phys. Rev. Lett., 112:146403, 2014.

[132] Z. Hiroi, J. Yamaura, T. Hirose, I. Nagashima, and Y. Okamoto. Lifshitz metalinsulator transition induced by the all-in/all-out magnetic order in the pyrochlore oxide cd2os2o7. APL Materials, 3(4):041501, 2015.

[133] Chang Liu, Takeshi Kondo, Rafael M. Fernandes, Ari D. Palczewski, Eun Deok Mun, Ni Ni, Alexander N. Thaler, Aaron Bostwick, Eli Rotenberg, Jorg Schmalian, Sergey L. Bud/'ko, Paul C. Canfield, and Adam Kaminski. Evidence for a lifshitz transition in electron-doped iron arsenic superconductors at the onset of superconductivity. Nat Phys, 6(6):419–423, 06 2010.

[134] Antonio Bianconi. Quantum materials: Shape resonances in superstripes. Nat Phys, 9(9):536–537, 09 2013.

[135] R. S. Dhaka, S. E. Hahn, E. Razzoli, Rui Jiang, M. Shi, B. N. Harmon, A. Thaler, S. L. Bud'ko, P. C. Canfield, and Adam Kaminski. Unusual temperature dependence of band dispersion in $Ba(fe_{1-x}ru_x)_2as_2$ and its consequences for antiferromagnetic ordering. Phys. Rev. Lett., 110:067002, 2013.

[136] A. B. Migdal. Interaction between electrons and lattice vibrations in a normal metal. J. Exptl. Theoret. Phys. (U.S.S.R.), 34:1438–1446, 1958.

[137] A. A. Kordyuk. Iron-based superconductors: Magnetism, superconductivity, and electronic structure (review article). Low Temperature Physics, 38(9):888–899, 2012.

[138] M. R. Norman, H. Ding, M. Randeria, J. C. Campuzano, T. Yokoya, T. Takeuchi, T. Takahashi, T. Mochiku, K. Kadowaki, P. Guptasarma, and D. G. Hinks. Destruction of the fermi surface in underdoped high-tc superconductors. Nature, 392(6672):157–160, 03 1998.

[139] M. V. Feigelman and L. B. Ioffe. Theory of diamagnetism in granular superconductors. Phys. Rev. Lett., 74:3447–3450, 1995.

[140] M. Randeria and A. Taylor. Bcs-bec crossover and the unitary fermi gas. Annual Review of Condensed Matter Physics,, 5:209–232, 2014.

[141] Wenhao Liu, Hai Lin, Ruizhe Kang, Yue Zhang, Xiyu Zhu, and Hai-Hu Wen. Magnetization of potassium doped p-terphenyl and p-quaterphenyl by high pressure synthesis. preprint arXiv:1706.06018, 2017.